Biomaterials for protection and repair of the central nervous system

by

Christopher D. Pritchard
M.Eng. Engineering Science – University of Oxford, 2007
M.S.CEP. Chemical Engineering Practice – M.I.T. 2009

Submitted to the Department of Chemical Engineering in partial fulfillment of the requirements
for the degree of

Doctorate in Chemical Engineering Practice
At the
Massachusetts Institute of Technology

June 2012

Signature of Author……………………………………………………………..………………..
Department of Chemical Engineering

Certified by………………………………………………………………………………………
Robert Langer
David H. Koch Institute Professor
Thesis Supervisor

Accepted by……………………………………………………………………..…………………..
William M. Deen
Professor of Chemical Engineering
Chairman, Committee for Graduate Students

Biomaterials for protection and repair of the central nervous system

By

Christopher D. Pritchard

Submitted to the Department of Chemical Engineering on May 1, 2012 in partial fulfillment of the requirements for the degree of Doctorate in Chemical Engineering Practice

ABSTRACT

An injectable hydrogel for controlled release of methylprednisolone was designed based on the inflammatory response during acute spinal cord injury. The gel is injectable through a small gauge needle, cross-links under physiological conditions, and releases methylprednisolone over a time period on the order of weeks. Swelling properties were characterized to address potential safety concerns for potential clinical use. Two studies are presented towards the development of a model Brown-Séquard syndrome and accompanying behavioral and pathological outcome measures for evaluation of biomaterials *in vivo*. A modified poly(glycerol-co-sebacic acid) membrane was developed using electrospun poly(ε-caprolactone) nanofibers. Retinal adhesion and histology was evaluated *in vitro*. Membranes were evaluated *in vivo* for their ability to selectively remove photoreceptors *in situ* and promote survival and integration of retinal transplants. Viscoelastic poly(ethylene glycol) sols were evaluated as potential vitreous substitutes. Finally, a business plan outlines the strategy towards clinical trials for a hydrogel vitreous substitute.

Thesis Supervisor: Robert Langer
Title: David H. Koch Institute Professor

ACKNOWLEDGMENTS

I möchte hiermit meine Eltern, meine Schwester, meine Grosseltern und Sonia bedanken, dass sie mich pausenlos in allen möglichen Wegen unterstützen und herausfordern.

Durch ihre Beispiele habe ich gelernt dass man im Leben versuchen muss das was man geschenkt bekommt an andere weiterzugeben. Somit ist dieser kleine Versuch, das Leben anderer Menschen ein wenig zu verbessern, meiner Familie gewidmet.

Albert Einstein is quoted: "Phantasie ist wichtiger als Wissen. Wissen ist begrenzt. Phantasie aber umfasst die ganze Welt." MIT is the factory of dreams, and in late 2007 there seemed to be no place bristling more with ideas than the third floor of E25. Bob Langer's conviction, that anything that *can't* be done *should* be done, is visionary. I am forever grateful for his insistence on tackling the most important problems first, and for his persistence to instill his sense of purpose in others.

I would like to explicitly thank some people who made a tremendous impact on my work at MIT: Frank Reynolds for inviting me to participate in his mission, Dr. Eric Woodard for his outstanding advice and friendship, and Dr. Fredrik Ghosh for his creativity, generosity and patience.

Finally, thank you to the many great friends I have made over the years, without whom there would be no stories to tell.

Table of Contents

I.

A novel injectable thiol-acrylate poly(ethylene glycol) hydrogel for sustained release of methylprednisolone sodium succinate

Christopher D. Pritchard (1), Timothy M. O'Shea (2), Daniel J. Siegwart (1), Eliezer Calo (3), Daniel G. Anderson (1), Francis M. Reynolds (4), John A. Thomas (5), Jonathan R. Slotkin (5), Eric J. Woodard (6), Robert Langer (1, 2)

(1) Department of Chemical Engineering
Massachusetts Institute of Technology, Cambridge, MA 02139, USA

(2) Harvard-MIT Division of Health Sciences and Technology
Massachusetts Institute of Technology, Cambridge, MA 02139, USA

(3) Koch Institute for Integrative Cancer Research
Massachusetts Institute of Technology, Cambridge, MA 02139, USA

(4) InVivo Therapeutics Corporation
Cambridge, MA 02141, USA

(5) Department of Neurosurgery
The Washington Brain and Spine Institute, Washington, DC 20010, USA

(6) Department of Neurosurgery
New England Baptist Hospital, Cambridge, MA 02120, USA

Reprinted with permission from Elsevier: Biomaterials. 2011 Jan;32(2):587-97.

Abstract

Clinically available injectable hydrogels face technical challenges associated with swelling after injection and toxicity from unreacted constituents that impede their performance as surgical biomaterials. To overcome these challenges, we developed a system where chemical gelation was controlled by a conjugate Michael addition between thiol and acrylate in aqueous media, with 97 % monomer conversion and 6 wt.% sol fraction. The hydrogel exhibited syneresis on equilibration, reducing to 59.7 % of its initial volume. It had mechanical properties similar to soft human tissue with an elastic modulus of 189.8 kPa. Furthermore, a mesh size of 6.9 nm resulted in sustained release of methylprednisolone sodium succinate with a loading efficiency of 2 mg/mL. Functionalization with 50 μg/mL of an oligolysine peptide resulted in attachment of freshly isolated murine mesenchymal stem cells. The rational design of the physical, chemical and biological properties of the hydrogel make it a potentially promising candidate for injectable applications.

Introduction

Synthetic polymeric hydrogels represent a promising technology platform for therapeutic intervention in a wide range of diseases and traumatic injuries. Comprising a three dimensional insoluble polymer network formed through the covalent or physical crosslinking of hydrophilic macromer precursors, hydrogels thermodynamically interact with aqueous media in a similar way to the native extracellular matrix (ECM). Owing to their easily tunable physical and chemical properties, hydrogels have been explored in a variety of diverse biomedical applications across the domains of controlled drug delivery, *in vitro* disease modeling and regenerative medicine [1-3]. Poly(ethylene glycol) (PEG) based hydrogels are particularly attractive for rapid clinical translation because devices and delivery systems based on PEG already have FDA approval due to the characteristic properties of PEG that limit non-specific protein adhesion and cellular interactions [4]. To date, a wide variety of novel PEG based hydrogels have been fabricated using numerous covalent gelation mechanisms. These include the free radical chain growth homopolymerization of activated -enes (most notably acrylates) [5]; free radical step growth photopolymerization of thiols and -enes [6-8], click chemistry of alkynes and azides [9], and conjugate Michael addition of multifunctional thiol and activated -ene precursors [10, 11]. Incorporation of various biological, chemical and/or mechanical cues have allowed these biomaterials to be applied to the study of cellular matrix interactions as well as disease states *in vitro* by recreating intricate cellular microenvironments [12]. However, the suitability of some of these systems for *in situ* gelation is limited by incomplete conversion of reactive functional groups and high sol fraction [2]. In addition, the use of metal catalysts, or photoinitiators and ultra-violet (UV) light, to initiate and propagate gelation creates biocompatibility concerns [9, 13]. Additional structural constraints, caused by substantial network defects and problematic large equilibrium volume swelling, have also hampered *in vivo* material performance in the past. Duraseal, a hydrogel composed of a mixture of polyethylene glycol (PEG) ester and trilysine amine solutions**,** caused spinal cord compression due to undue swelling and as a result induced or worsened quadriparesis requiring intervening decompression surgery [14, 15]. Hydrogels of co-poly(methylacrylate-hydroxyethyl acrylate) used in scleral buckling procedures to treat retinal detachment displayed compromised long-term performance attributed to undesirable swelling and also degradation [16, 17]. These cases demonstrate that unfavorable physical properties of injectable hydrogels can create severe post surgical complications. Such limitations have been overcome by post-gelation processing prior to implantation, but this precludes their surgical application via a minimally invasive injection [18]. Hydrogels that display temperature dependent de-swelling properties have been developed previously through the covalent crosslinking of thermoreversible physical gels composed of triblock poly(ethylene oxide) (PEO) and poly(propylene oxide) (PPO) macromers. However a capacity to achieve sustained release of low molecular weight molecules using this system was not demonstrated and photopolymerization was still required for irreversible network formation [19].

We were interested in developing a more robust hydrogel technology platform that could overcome the above constraints and bypass additional processing requirements through a capacity to safely transition from a sol precursor mixture to a gel state *in situ*. Utilizing a rational engineering design approach, we defined performance parameters applicable to a wide spectrum of diseased and injured tissues prior to the selection of material constituents and a gelation mechanism. These requirements included no volume increase during equilibration, resilient mechanical properties that match human tissues of interest, a mesh size adequate for diffusion-controlled release of hydrophilic small molecule drugs, tunable gelation kinetics and the ability to functionalize the material with biological motifs to guide cellular interactions. An injectable biomaterial displaying such properties would provide a substrate for diverse therapeutic interventions that could permit minimally invasive surgical application, minimal compressive tissue damage, reduced inflammation and risk of infection, as well as faster recovery for patients following surgery [20]. Given the desire to achieve rapid gelation under ambient conditions without use of reaction initiators or UV light, conjugate thiol-ene Michael addition was selected as a suitable chemical cross-linking mechanism for the injectable hydrogel system. This reaction involves the direct addition of a dissociated thiolate nucleophile and an unsaturated carbon double bond, activated by a neighboring electron withdrawing group such as an ester or amide [10, 11, 21, 22]. Advantageously, this mechanism has been shown to be applicable to a wide range of commercially available precursors, forms polymer networks with minimal structural deficiencies and can react completely within a surgically relevant timeframe, while avoiding the production of free radicals [23]. This paper describes the rational design and characterization of a novel PEG based hydrogel and an investigation of its applicability for drug release and cell adhesion *in vitro*.

Materials and methods

Materials

Poly(ethylene glycol) diacrylate (PEG-400-DA, Polyscience, Warrington, PA) and ethoxylated trimethylolpropane tri-3-mercaptopropionate (ETTMP, Thiocure 1300, Bruno Bock, Marschacht, Germany) were passed through a short column of activated basic aluminum oxide (Cole-Parmer Instrument Company, Vernon Hills, IL) to remove the radical inhibitor, hydroquinone monomethyl ether (MEHQ, 400ppm) prior to use. Physiologically isotonic phosphate-buffered saline (PBS, pH 7.4, 1.06 mM potassium phosphate monobasic, 155.17 mM sodium chloride, 2.97 mM sodium phosphate dibasic, Invitrogen, Carlsbad, PA), Dulbecco's Modified Eagle Medium (DMEM, 1X, 4.5g/L Glucose, 4mM L-glutamine, Invitrogen, Carlsbad, PA), methylprednisolone sodium succinate (MPSS, CAS 2375-03-3, Sigma-Aldrich Corp., St. Louis MO), oligolysine peptide (14 lysine amino acid units with a cysteine at both the N and C termini, Applied Biosystems 430A, Biopolymers & Proteomics Core Facility, Koch Institute at MIT, Cambridge MA), sodium hydroxide (NaOH, Mallinckrodt), and poly(ethylene glycol) (400 g/mol, Fluka), acetonitrile (Chromasolv Plus, Sigma-Aldrich Corp., St. Louis MO), ddH$_2$0 (NANOpure, Thermo Fisher Scientific, Waltham MA), and formic acid (Sigma-Aldrich Corp., St. Louis MO) were used as received.

Instrumentation

UV-vis was measured on a Spectramax Plus spectrophotometer (Molecular Devices). pH was measured using a digital pH probe (Russell RL060P, Thermo Scientific). Fourier transform infrared (FT-IR) spectroscopy was taken using an Alpha FT-IR with Eco ATR sampling module (Bruker Optics, Billerica MA). Dynamic rheology was performed using an AR G-2 with a 40 mm diameter 2° cone and plate set-up (TA Instruments, New Castle, DE). Specific gravity was measured using a kit (Mineralab, Prescott AZ). Tensile testing was performed on a Model 5542 (Instron, Norwood, MA). High performance liquid chromatography (HPLC) was performed on an Agilent 1100 (Agilent Technologies Inc., Santa Clara CA) based on an existing procedure [24]. A C18 column (dC18 Atlantis 5μm, 4.6 mm x 250 mm, Waters, Ireland) was used at a flow rate of 1 mL/min. The mobile phase was 60:40 acetonitrile and ddH_20 with 0.1% formic acid. Mathematica (Mathematica, Wolfram Research, Champaign IL) was employed. Microscopy was performed on using a Carl Zeiss microscope (MicroImaging Inc., Thornwood NY).

Poly(ethylene glycol) hydrogel fabrication

Poly(ethylene glycol) based hydrogels were formed using precursors containing multiple thiol and acrylate functional groups capable of reacting in an aqueous solvent to form a network structure (Fig. 1 and Scheme. 1). Aqueous stock solutions of the two precursors, PEG-400-DA, and ETTMP, were prepared by dissolving the polymers in PBS at 4 °C for 24 hours. To fabricate the hydrogels, appropriate volumes of the two stock solutions resulting in an equimolar stoichiometric ratio of thiol and acrylate functional groups were combined, yielding a final total polymer concentration of 25 wt.% in a Falcon tube at 4 °C. Following a five minute incubation period at 4 °C to increase dissolution of the precursors in the mixture, molds of a desired size were filled with the solution and transferred to an incubator at 37 °C to complete gelation. Gelation occurred within 5 minutes of incubation. However, samples produced for structural characterization and mechanical testing were maintained in the 37 °C environment for 20 minutes to promote complete conversion of functional groups. The gelation protocol described above was applied to all hydrogels prepared in PBS. For cell culture studies, DMEM was incorporated as the solvent phase in the hydrogel by incubating the cured hydrogel in the media for a 24 hour period, prior to cell seeding. For MPSS encapsulation and release studies, weighed samples of the steroid were incorporated into the PEG-400-DA solution for a final concentration of 0.5, 1 or 2 mg/mL in the hydrogels. Functionalization of the hydrogel with an oligolysine peptide was performed by dissolving the peptide in the PEG-400-DA in solution, prior to mixing with the ETTMP stock solution. The oligolysine was reacted into the hydrogel via its thiol-containing cysteine end residues. Solutions were sterilized by syringe filtration through a 0.2 μm nylon filter. The concentrations of oligopeptide used were 5, 50 and 500 μg/mL.

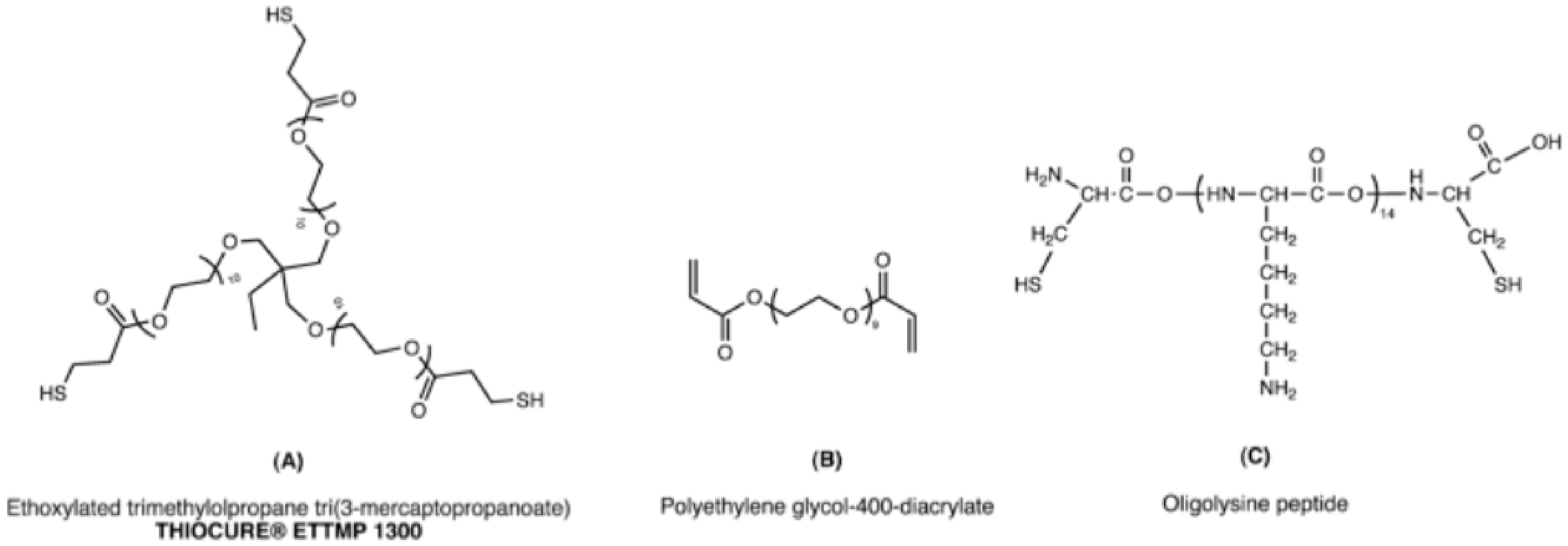

(A)

Ethoxylated trimethylolpropane tri(3-mercaptopropanoate)
THIOCURE® ETTMP 1300

(B)

Polyethylene glycol-400-diacrylate

(C)

Oligolysine peptide

Figure 1. Hydrogel polymer components. **A**: Ethoxylated trimethylolpropane tri(3-mercaptopropanoate) (ETTMP). **B**: Poly(ethylene glycol) diacrylate (PEG-400-DA). **C**: Oligolysine peptide with cysteine residues at N and C termini (Cys-Lys$_{14}$-Cys).

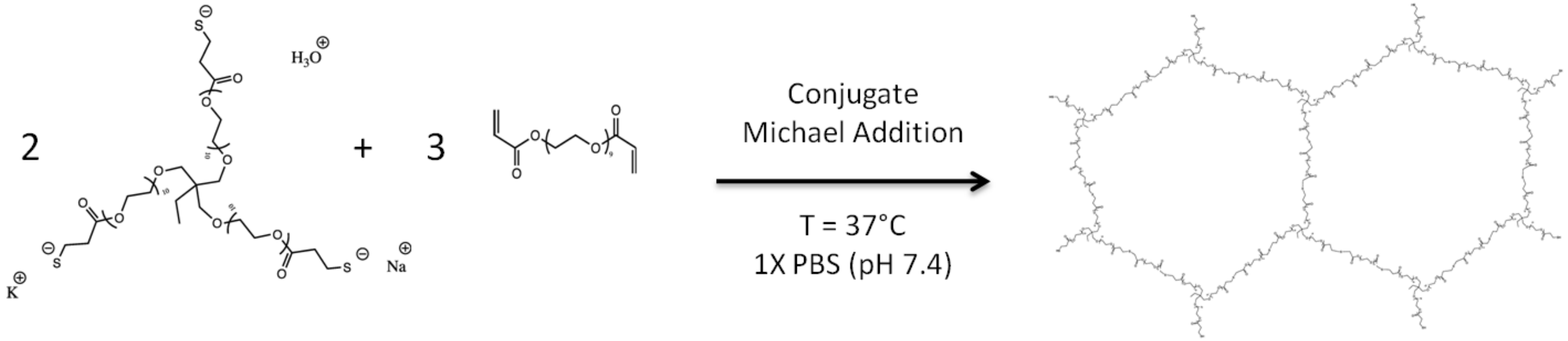

Scheme 1. Formation of cross-linked network under physiological conditions. In aqueous medium a thiol functional group of ETTMP is in equilibrium with thiolate, its conjugate base. A 2:3 ratio of ETTMP and PEG-400-DA results in stoichiometric equivalents of thiol and acrylate functional groups. Due to the multi-functionality (n=3) of ETTMP, a cross-linked network is formed. The thiolate anion in ETTMP attacks from the unsaturated β-carbon of the acrylate in PEG-400-DA,which is activated towards nucleophiles, in a nucleophilic conjugate addition reaction. In a buffer, a metal cation may act as a counterion to thiolate and as a Lewis acid, coordinating with the ester carbonyl in PEG-400-DA to further activate it, and promote nucleophilic attack of thiolate from the unsaturated β-carbon.

Hydrogel precursors analysis

Solubility of hydrogel precursors

To investigate the parameters affecting solubility of ETTMP in PBS, nine standard solutions, with concentrations from 5 wt.% to 45 wt.%, at 5 wt.% increments, were prepared and stored at 4 °C for 24 hours. Following vortexing, 4 x 200 μL of each standard was aliquotted into a transparent 96-well plate and equilibrated at 4 °C for 30 minutes. The absorbance of the standards was then assessed spectrophotometrically at 37 °C for 20 minutes ($\lambda = 450$ nm). The initial absorbance and the time at which a rapid increase in absorbance occurred (represented by a characteristic inflection in the absorbance curve) were used as measures of solubility at 4 °C and stability (precipitation/phase separation) at 37 °C respectively. The solubility of the PEG-400-DA was assessed but not reported in this paper, as this polymer was soluble over the concentration and temperature ranges of interest.

Measuring the pKa of ETTMP

A 50 mL 0.1 M (0.3 N) solution of ETTMP in ddH$_2$0 was prepared in a 250 mL beaker with a magnetic stir bar and a digital pH probe. A 0.1 M solution of NaOH in ddH$_2$0 was titrated in increments of 500 to 1200 μL into the ETTMP solution with concomitant pH measurements until the pH increased beyond the upper equivalence point (approximately 150 mL). The pKa was determined as the pH halfway between the equivalence points.

Gelation kinetics and mechanism

The gelation kinetics involving sol-gel transition and chemical conversion were assessed using dynamic rheology and FT-IR spectroscopy respectively. The Michael addition mechanism was assessed by evaluating the gelation response as a function of buffer pH and counterion content using these two tests. To study the presence of radical reactions (thiyl-acrylate addition or acrylate homopolymerization), gelation was also performed in the presence of radical inhibitor, MEHQ, by not filtering PEG-400-DA prior to use.

FT-IR analysis

500 μL hydrogel discs were cast using a 24-well tissue culture plate as a mold following the fabrication protocol outlined above. Hydrogel samples were extracted from their molds after curing and either lyophilized for a period of 36 hours, or equilibrated by incubation at 37 °C in a 12-well plate (4 mL per well of PBS) for 48 hours followed by lyophilization. FT-IR spectra were obtained on the dry gels by measuring attenuated total reflection. The differences in the amount of unreacted acrylate and thiol constituents remaining in the two hydrogel sample groups (characterized by C=C stretch at 1675-1600 cm^{-1} and S-H stretch at 2550-2600 cm^{-1}) were assessed through a quantification analysis using the OPUS software package. Standard curves for the quantification analysis were constructed by diluting the precursors to known concentrations using poly(ethylene glycol) (400 g/mol) polymer. Linear regression curves were constructed from this data and used to assess residual acrylate ($R^2 = 0.998$) and thiol ($R^2 = 1.000$) in the hydrogels.

Dynamic rheology

The sol-gel transition was studied *in situ* using dynamic rheology. 600 μL aliquots of precursor/PBS solution were prepared and incubated at 4 °C for 5 minutes. The solutions were then transferred to the rheometer. First measurements were recorded 40 seconds after removal from the 4 °C environment. The dynamic evolution of the mechanical properties (storage (G') and loss (G”) moduli) was assessed at 5% strain and a frequency of 10 rad s^{-1} for 10 minutes. Separately, a frequency sweep was performed at 5% strain to verify that testing conditions were within the linear viscoelastic range. The gel point was characterized as the time when tan(δ) =G’’/G’= 1 was observed, which was deemed a valid approximation given that the prepared hydrogel was stoichiometrically balanced and sufficiently far away from its glass transition temperature [25, 26]. The proposed mechanism of hydrogel formation via a base catalyzed Michael type addition reaction between thiolate anion and acrylate was studied further by assessing functional group conversion and gelation kinetics under varying buffer conditions. Potassium and sodium phosphate buffer 0.1M solutions with pH values of 6, 6.6, 7, 7.4 and 8 were prepared by mixing and diluting appropriate quantities of 1M solutions containing their respective monobasic dihydrogen and dibasic monohydrogen phosphate salts. Additional FT-IR and dynamic rheology experiments were performed on hydrogels using these buffer solutions as the solvent phase. The extent of chemical conversion of the acrylate and thiol functional groups and the gel point time were characterized for each buffer solution. For dynamic rheology testing of these hydrogels, the 5 minute incubation procedure at 4 °C was not necessary.

Structural and mechanical properties of the hydrogel

Hydrogel equilibration and sol fraction

The hydrogel equilibration behavior and sol fraction were evaluated using 500 μL hydrogel discs prepared in a 24-well plate mold. The wet masses of hydrogels cured and swollen for 6, 12, 24, 48 and 72 hours were recorded before then being lyophilized to determine the mass of dry polymer. To calculate the relaxed (immediately after curing) and equilibrium polymer volume fractions ($\nu_{2,r}$ and $\nu_{2,s}$ respectively, per equations 1 and 2), the specific gravity of the hydrogel (cured and equilibrated for the same above incremental time points) as well as the dry polymer network were measured, using a specific gravity kit and applying Archimedes' buoyancy law before then being converted to volume measurements.

Equilibrium polymer volume fraction $$v_{2,s} = \frac{V_p}{V_{hgel,s}} \quad (1)$$

Polymer volume fraction in the relaxed state $$v_{2,r} = \frac{V_p}{V_{hgel,r}} \quad (2)$$

The sol mass fraction was computed by comparing the differences in dry polymer weight between the cured and equilibrated samples.

Hydrogel degradation

Individual 500 μL hydrogel discs were incubated in 4 mL PBS in 12-well plates for a period of 12 weeks to assess hydrolytic degradation. Masses of wet and lyophilized gels were measured in triplicate at 1, 2, 4, 6, and 9 weeks. Before lyophilization, the hydrogels were washed in distilled water to remove any residual salt that may have built up on the surface. The total dry polymer mass loss of each sample was determined through comparisons with the dry weight of cured (non-equilibrated) samples.

Mechanical testing of equilibrated and cured hydrogels

To assess the mechanical properties of the hydrogel, tensile testing was performed on cured and equilibrated samples. Planar sheets of hydrogel with 3 mm uniform thickness were fabricated in a flat rectangular mold, with equilibrated samples incubated in PBS for 48 hours before use. Immediately prior to testing, ASTM 412-D type specimens were cut from the planar sheet using a stainless steel die and a mallet. The final dimensions of the specimen were measured using Vernier calipers before being loaded into the testing jig. Tests were performed using a 50 N static load cell under a strain rate of 5 mm min^{-1}. The shear and elastic modulus was computed assuming incompressible neo-Hookean mechanics (Poisson's Ratio, ν~ 0.5) and assessing engineering stress as a function of both extension ratio and deformation factor [27, 28]. Using a statistical mechanics approach and applying the experimentally observed modulus value (G) (as calculated by fitting a linear regression for engineering stress versus deformation factor), the number of elastically effective chains per unit volume (ν_e / V_o) for equilibrated hydrogels was determined (Equation 3).

$$\begin{gathered}\tau = \left[RT \left(\frac{\nu_e}{V_o} \right) \left(\frac{\nu_{2,s}}{\nu_{2,r}} \right)^{1/3} \right] \left(\lambda - \frac{1}{\lambda^2} \right) \Rightarrow \nu_e = \nu \left(1 - \frac{2N}{\nu} \right) \\ G_{aff} = RT \left(\frac{\nu_e}{V_o} \right) \left(\frac{\nu_{2,s}}{\nu_{2,r}} \right)^{1/3} = \frac{1}{3} E \end{gathered} \tag{3}$$

Additional modeling of the gel structure through the application of the Miller-Macosko branching theory for end-linked networks was used to characterize the extent of reaction, as well as the ideal mechanical properties based upon the measured sol fraction [29, 30]. An approximate mesh size for the hydrogel in both cured and equilibrium states was also determined by calculating the distance between active crosslinks, μ_e (= $2\nu_e/f$).

In vitro analysis

Drug release and stability study

The release kinetics of MPSS from hydrogels was studied as follows. Hydrogels containing 0.5, 1 and 2 mg/mL MPSS (dissolved in precursor solutions prior to gelation) were fabricated in 1.7 mL Eppendorf tubes (21 x 250 μL for each concentration of MPSS). Following complete gelation (20 minutes at 37 °C), 1 mL PBS was added to each tube and incubated at 37 °C.

Degradation of MPSS in PBS was measured by incubating stock solutions of MPSS in PBS at 37 °C (500, 250 and 125 μg/mL, 21 x 1 mL for each concentration). After 6, 12, 24, 48, 96, 192 or 384 hours the solution above the hydrogels or from stock aliquots were extracted and stored in Eppendorf tubes at - 80 °C (n=3 for each concentration at each time point). MPSS concentrations were analyzed using high HPLC based on an existing procedure [24]. Ultraviolet light absorbance was measured at 238nm. The MPSS peak elutes at 4.864 minutes. A standard curve was calculated using HPLC peak areas from six points in a series dilution from a stock solution (85 μg/mL MPSS in PBS, diluted geometrically. A response factor of 8.7446 mAUs mL μg^{-1} was calculated with R^2 of 0.9997 (linear regression with zero intercept). Mass transfer coefficients for MPSS release from the hydrogel were calculated by solving a system of differential equations for drug release kinetics and the degradation of MPSS in PBS and fitting a regression of appropriate form to the data using Mathematica.

Cell adhesion assay

Hydrogels were prepared in PBS, with final concentrations of oligolysine peptide of 0, 5, 50 and 500 μg/mL (4 x 250 μL each), in a sterile 24-well polystyrene tissue culture plate, before being incubated in DMEM for 24 hours to facilitate solvent exchange. On the same plate, 4 wells were incubated with 200 μL for 3 hours at room temperature, with 0.25 mg/mL oligolysine peptide in DMEM, followed by aspiration of the media. The remaining 4 wells were left uncoated as positive controls. The tissue culture plate was further sterilized in a laminar flow hood by ultraviolet irradiation for 15-30 minutes with the addition of excess media to the gels to maintain hydration. Freshly isolated bone marrow derived murine mesenchymal stem cells (mMSC) were then seeded using sterile technique at a density of 10^5 cells per well and incubated (2mL DMEM per well, 37 ºC, 5% CO_2). After 24 hours, digital images of the cells were obtained from all wells (40x Phase 2 contrast bright field, light microscope).

Statistics

Throughout this paper all statistics are represented as mean ± standard deviation. Hypothesis tests of comparison were performed using the student's t-test, assuming that variances were unknown and not equal, with p-values of less than 0.05 taken as significant.

Results

Hydrogel precursor analysis

Solubility of ETTMP

PEG-DA-400 was soluble in PBS over the temperature (4 to 37 ºC) and concentration (5 to 45 wt.%) ranges of interest. In contrast, the solubility of ETTMP in PBS changed as a function of concentration. Therefore, experiments were performed to characterize the solubility of ETTMP in PBS at 4 ºC (Fig. 2) and stability during heating from 4 to 37 ºC (Fig. 3). ETTMP solubility in PBS at 4 ºC decreased nonlinearly from 5 to 25 wt.%, determined by the increasing absorbance of visible light ($\lambda = 450$ nm). The solubility of the polymer then increased again from 25 to 45 wt.%, exhibiting the highest solubility from 40 to 45 wt.% (Fig. 2). The results were confirmed by visual inspection, where mixtures from 20 to 35 wt.% were above their cloud point at 4 ºC in PBS. The stability of ETTMP in PBS when heated from 4 to 37 ºC was measured by dissolving ETTMP at different concentrations at 4ºC, followed by heating at 37 ºC for 20 minutes. These experimental conditions were chosen to replicate the physiological environment under which gelation would take place *in situ*. Regression of error functions (in the form $A \operatorname{erf}[b(t - t_{inf})] + d$) were applied to the temporal absorbance profiles and used to determine the time where the inflection in absorbance of visible light ($\lambda = 450$ nm) occurred (t_{inf}), marking the maxima in rate of precipitation (Fig. 3). The precipitation time decreased from approximately 794 to 485 seconds between 5 and 10 wt.%. Precipitation time increased again markedly from 483 to 1044 seconds to between 20 and 45 wt.%. Based on these results, gelation experiments were performed with varying concentrations of ETTMP in the stock solution. The concentration of the PEG-400-DA stock solution was modified accordingly to maintain a total polymer concentration of 25 wt.% in the hydrogels, with no precipitation of PEG-400-DA observed in the stock solution over the resulting concentration range. Higher sol fractions of the resulting hydrogels were observed using ETTMP stock solutions between 25 and 35 wt.% compared to 40 wt.%, associated with reduced ETTMP stability in solution. Gelation did not readily occur using a 45 wt.% ETTMP stock solution. When the concentration was increased above 50 wt.%, the mixing was greatly reduced due to increased viscosity, which hindered the polymerization. The 40 wt.% concentration was therefore used for further experiments.

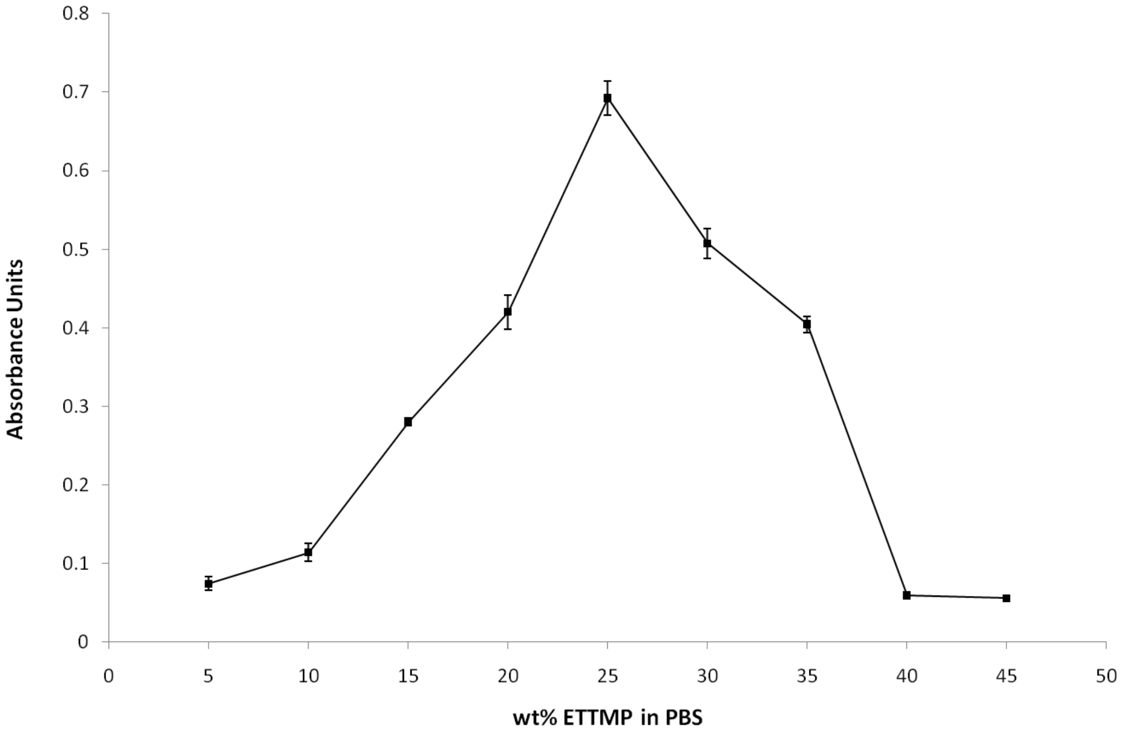

Figure 2. Solubility of ETTMP in PBS at 4ºC. The absorbances of 200 μL standards of ETTMP at different concentrations in PBS were measured at a wavelength of 450 nm. The dependence of solubility on concentration between 5 and 45 wt.% is not monotonic, with the solubility minimum observed at 25 wt.%. Error bars are standard deviation, n=4.

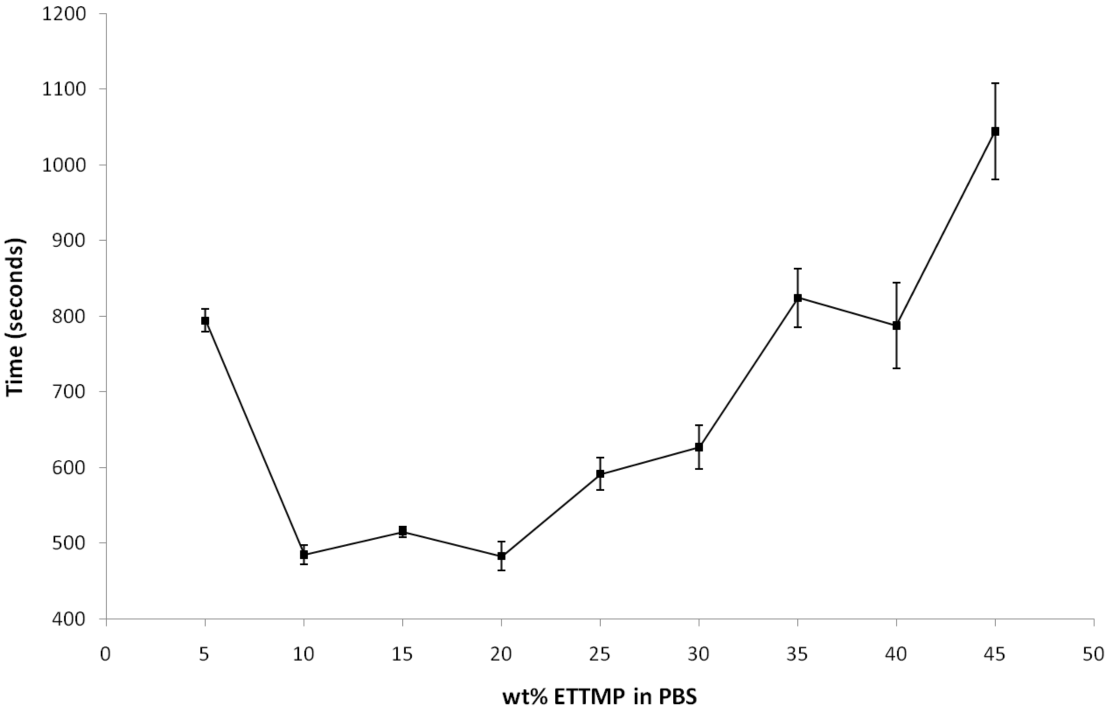

Figure 3. Stability of ETTMP in PBS from 4ºC to 37ºC. The absorbances of 200 μL standards of ETTMP at different concentration, prepared at 4ºC, were measured at a wavelength of 450 nm at 37ºC for 20 minutes. The graph shows the time taken for the standards to reach an inflection point in absorbance increase. The precipitation time is not a monotonic function of concentration between 5 and 45 wt.%, and is a maximum at 45 wt.%. Error bars are standard deviation, n=4.

Measuring the pK_a of ETTMP

The pK_a of ETTMP was measured in order to predict the extent of thiol deprotonation as a function of pH in aqueous media. A titration of 0.1M ETTMP at 24 ºC with 0.1M NaOH resulted in a pK_a for ETTMP of 9.87 (Fig. 4).

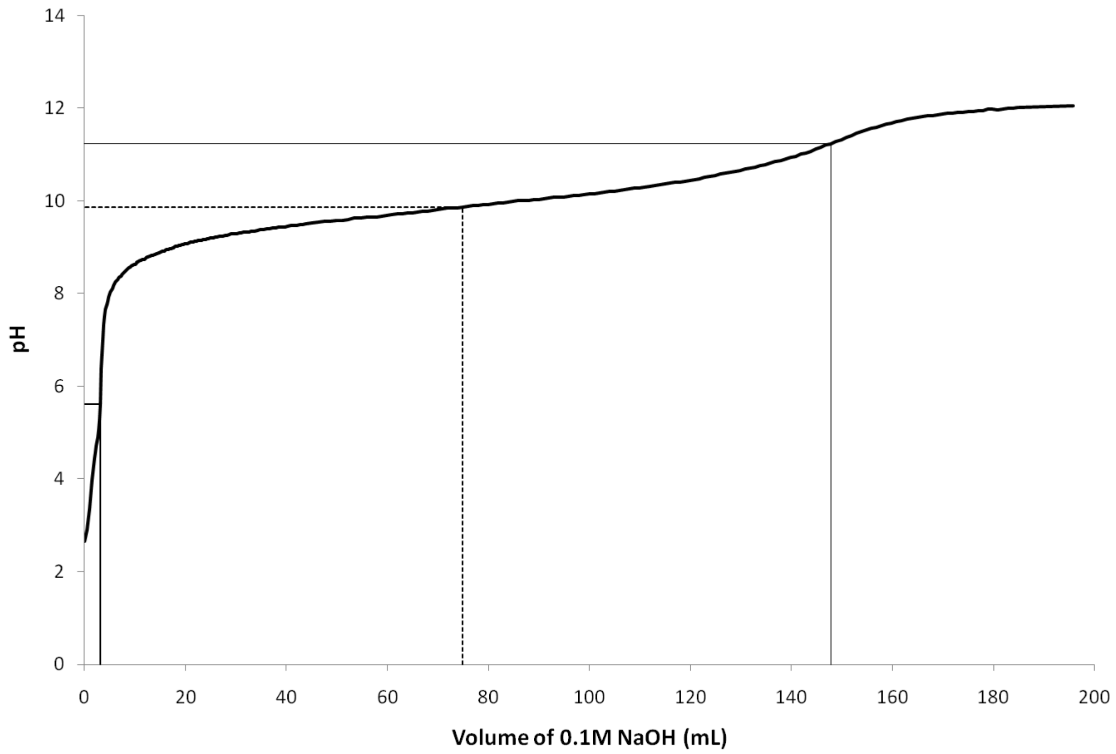

Figure 4. pK_a of ETTMP at 24 ºC. 0.1M ETTMP (0.3N, 50 mL) at 24 ºC was titrated with 0.1M sodium hydroxide (NaOH) (0.1N, 200 mL). The pK_a (dashed line) of 9.87 (74.8 mL 0.1M NaOH) was determined as halfway between equivalence points (solid lines) at pH 5.62 (3.2 mL 0.1M NaOH) and pH 11.23 (147.8 mL 0.1M NaOH).

Gelation kinetics

Fourier transform infra-red spectroscopy

Attenuated total reflection FT-IR was used to measure PEG-400-DA acrylate C=C stretch (1675-1600 cm^{-1}) and ETTMP S-H stretch (2550-2600 cm^{-1}) (Fig. 5). Following the reaction in PBS, 15.0 vol.% thiol and 6.7 vol.% acrylate were detected in cured gels, after lyophilization. 8.0 vol.% thiol and -2.7 vol.% acrylate were detected in equilibrated gels, after lyophilization. These parameters were determined using the FT-IR quantification software. The apparatus used appeared to have a detection limitation for low macromer concentrations, where peaks expected based on the values obtained could not clearly be distinguished from noise (Fig. 5C, D).

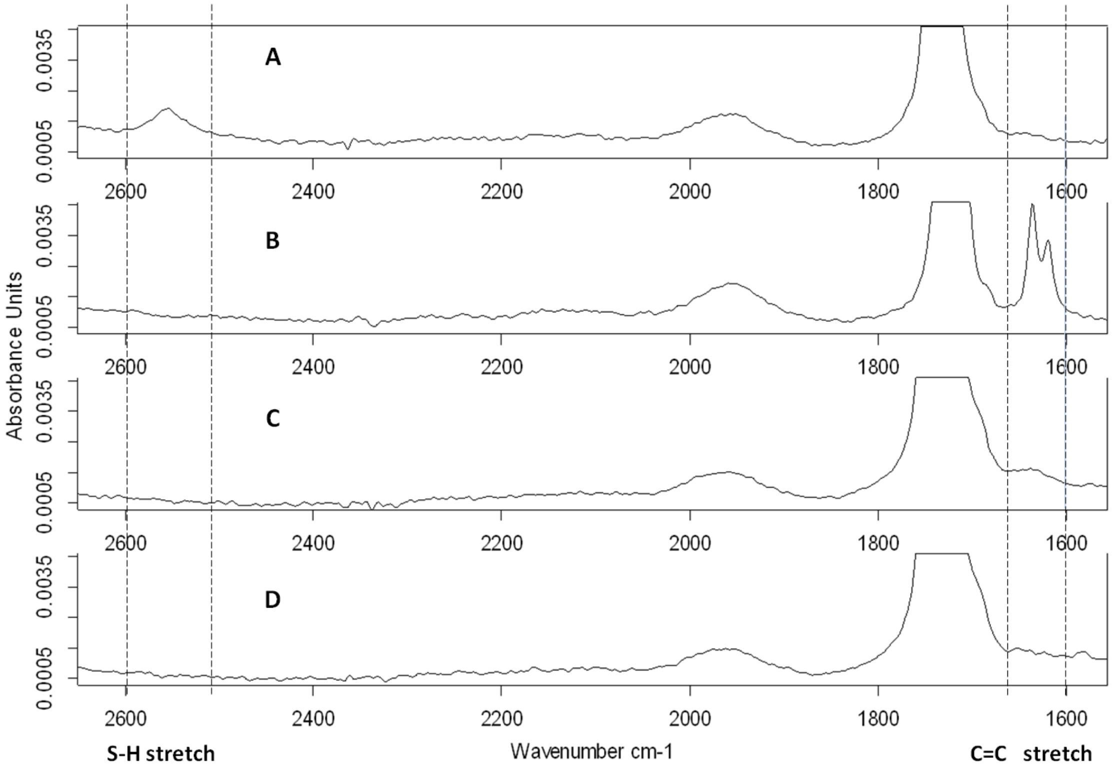

Figure 5. Fourier transform infrared spectroscopy (FT-IR) spectra, measured by attenuated total reflection through a Zinc Selenide (ZnSe) crystal, normalized by maximum and minimum absorbance. C=C stretch was measured at 1675-1600 cm^{-1} and S-H stretch at 2550-2600 cm^{-1}. **A**: ETTMP. There is an S-H stretch but no C=C stretch. **B**: PEG-400-DA. No S-H stretch is present but two peaks in the C=C stretch region are visible. **C**: Hydrogel, cured and lyophilized. Following reaction of ETTMP and PEG-400-DA in PBS, both S-H stretch and C=C stretch have disappeared from the lyophilized network. **D**: Hydrogel, equilibrated for 48 hours and lyophilized. Spectrum displays same characteristics as the as cured samples.

Dynamic rheology

Dynamic rheology was performed to quantify the critical gelation time, defined where the magnitudes of the elastic (G') and loss (G") moduli are equivalent (Fig. 6). Gelation times were measured in phosphate buffer solutions of varying pH and either Na or K cations. The gelation time decreased exponentially with increasing pH, for 0.1 M phosphate buffer solution containing either Na or K cations (Fig. 7). The gelation time was also weakly dependent on the cation in the buffer, decreasing as the ionization energy of the cation decreased from Na to K. The gelation time in PBS increased with the inclusion of MEHQ, from 459.7 to 475.3 seconds ($p < 0.05$).

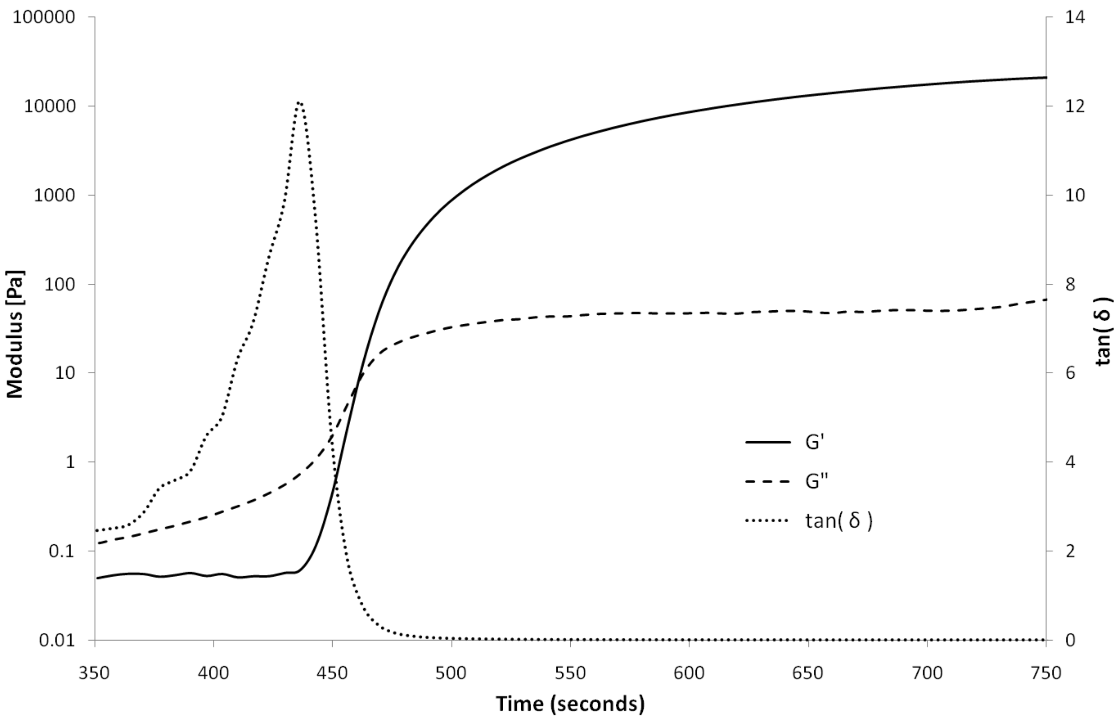

Figure 6. Dynamic rheology of characteristic gel point between ETTMP and PEG-400-DA in PBS. Gel point can be observed by dynamic rheology as the point where the magnitude of the elastic modulus (G’) equals the loss modulus (G”). Shortly before this point, G” rises as the molecular weight of co-polymer chains increases significantly prior to network formation, resulting in increased viscosity. This is reflected in a maximum in tan(delta). At the gel point G’ increases sharply as an infinite molecular weight network forms in solution. G’ and G” reach asymptotes following complete conversion indicating a viscoelastic product.

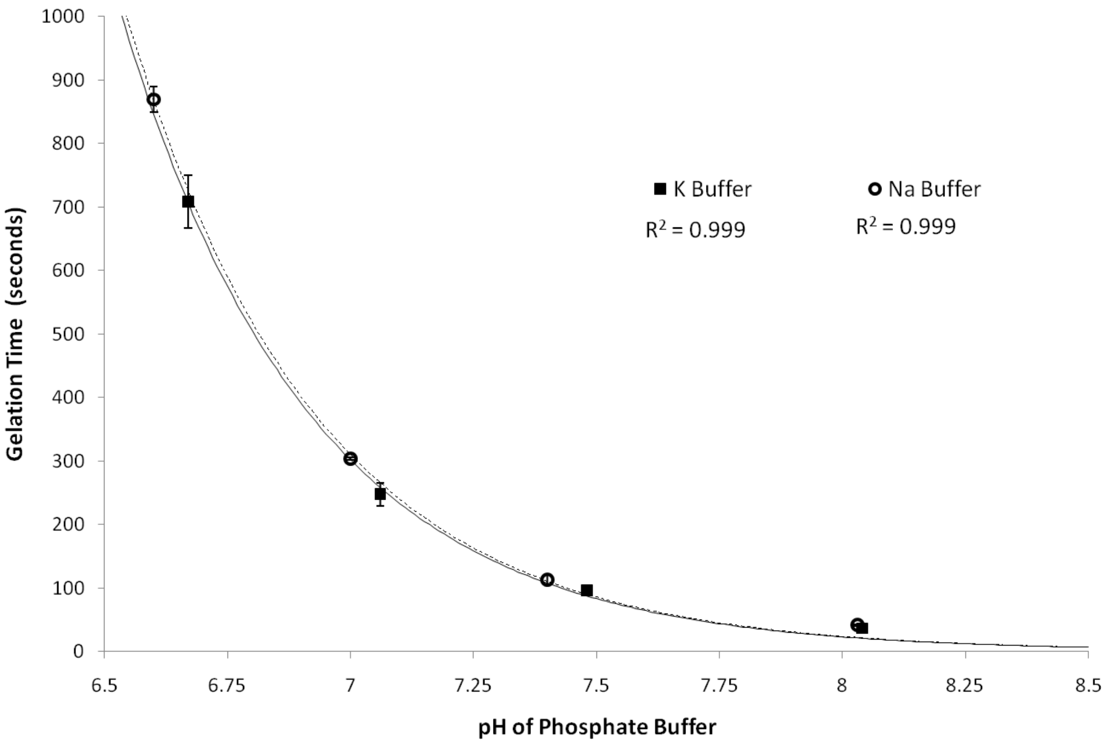

Figure 7. Gelation kinetics as a function of pH and alkali metal cation in 0.1 M phosphate buffer at 25 ºC. Gel point was determined by dynamic rheology where the magnitudes of elastic (G’) and loss (G”) moduli are equal. The reaction rate between ETTMP and PEG-400-DA follows an exponential dependence on buffer pH, and is therefore linearly proportional to thiolate concentration. The reaction rate is weakly dependent on the alkali metal cation in the buffer.

Structural and mechanical properties of the hydrogel

Hydrogel equilibration and sol fraction

Equilibrium polymer volume, mass and sol fractions were measured for hydrogels cured at 37 ºC in different solvents. The hydrogel exhibited syneresis during equilibration. The polymer volume and mass fractions in the relaxed state were 22.1 vol.% and 26.1 wt.% immediately post gelation and increased to 36.7 vol.% and 39.4 wt.% after 12 hours of incubation in PBS. This equilibrium value was maintained relatively constant through 48 hours (Fig. 8). The polymer mass fraction followed the volume fraction profile over the 72 hour period analyzed but was offset by 2 to 3 % at each time point. By comparing dry mass initially and following equilibration, it was determined that 93.7 ± 1.0 wt.% and 95.4 ± 1.4 wt.% of the polymer precursors were incorporated into the hydrogel network in PBS with or without MEHQ respectively (no statistical significance). MEHQ did not affect the equilibrium volume or mass fractions. Hydrogels prepared in ddH_20 without MEHQ incorporated 64.2 ± 5.8 wt.% of precursors into the gel network and had an equilibrium polymer mass fraction of 26.9 ± 1.6 wt.%. Hydrogels did not form in ddH_2O with MEHQ and the polymer precipitated prior to gelation.

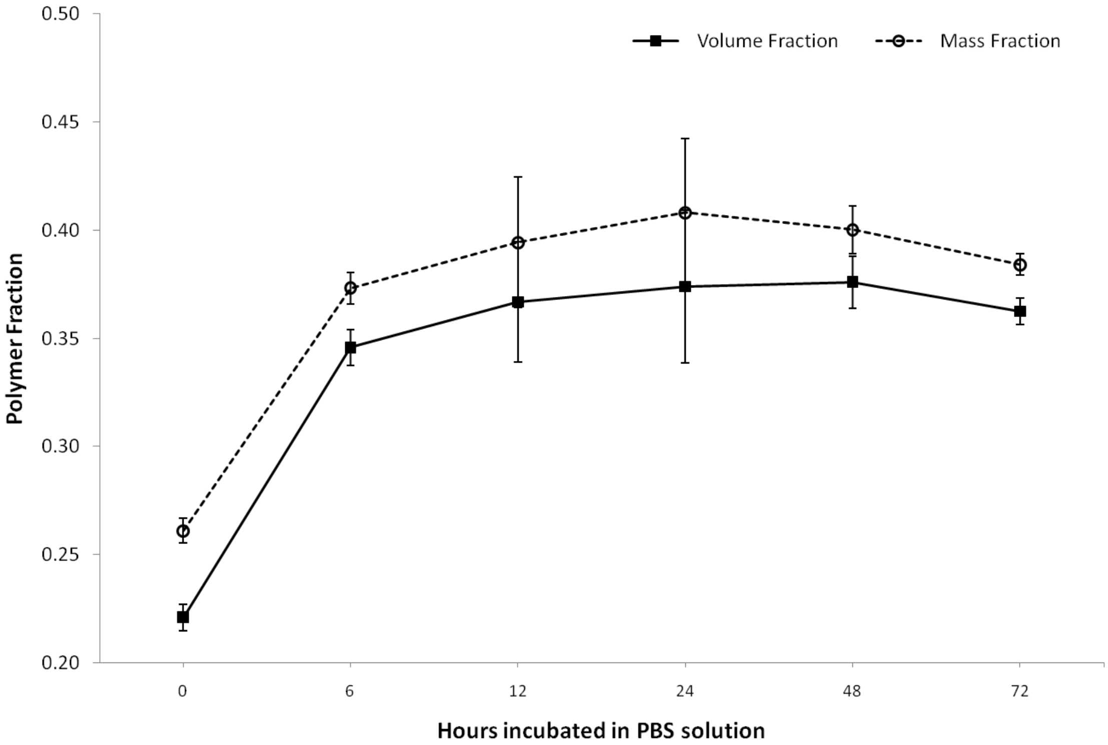

Figure 8. Equilibrium volume and mass fractions of hydrogels in PBS (pH 7.4) at 37 ºC over a 72 hour period. A rapid increase from the relaxed volume fraction is observed over the first 12 hours before a stable equilibrium volume fraction is obtained and sustained at a near constant value over 48 hours. The mass fraction profile traces the volume fraction response but is offset by 2-3 % for each time point.

Degradation

The degradation profile of hydrogels was studied by measuring mass loss of lyophilized samples in PBS at 37 ºC over a period of 9 weeks (Fig. 9A). Gels reached equilibrium within 48 hours of incubation displaying a characteristic sol fraction of approximately 6 wt.%, similar to the value observed in equilibration studies. The hydrogel degraded linearly *in vitro* at a rate of 2 wt.% a week over the 9 weeks. Furthermore, the hydrogel displayed approximately constant polymer mass and volume fractions over the initial 4 week period with an increased solvent uptake apparent from 6 weeks (Fig 9B). After 4 weeks the hydrogel exhibited a noticeable reduction in mechanical rigidity and could be easily compressed upon handling.

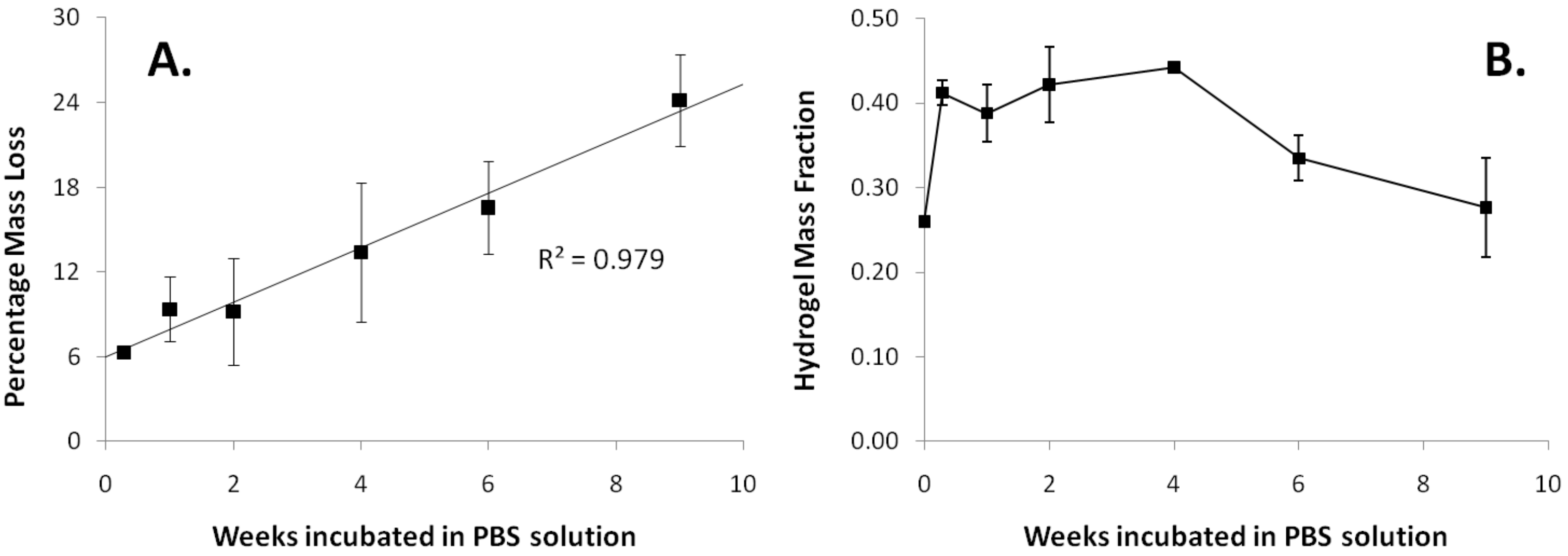

Figure 9. Degradation of hydrogels in PBS (pH 7.4) at 37 ºC. The chosen buffer and temperature simulate physiological conditions where hydrolysis of ester bonds in the network result in gel mass loss. **A.** Gels reach equilibrium within 48 hours of incubation with no appreciable mass loss and degrade linearly over 9 weeks *in vitro*. **B.** The polymer mass fraction remained approximately constant following equilibration for the first 4 weeks of incubation and exhibited increased solvent uptake from 6 weeks. Error is standard deviation, n=3 for each time point.

Mechanical testing

Tensile testing was performed on hydrogels cured at 37 ºC in their initial and equilibrium-swollen states (Fig. 10). From the data obtained, ultimate tensile strengths and terminal extensions were recorded (Table 1). Elastomer rubber elasticity theory was applied to quantify the elastic modulus of the hydrogels by using the characteristic linear relationship between tensile stress and deformation factor over the extension ratio range of relevance [27]. For the equilibrated hydrogels a shear modulus of 63.26 ± 2.13 kPa was determined, which was significantly greater than the modulus recorded for the cured hydrogels, calculated to be 50.98 ± 1.42 kPa ($p \ll 0.001$). By assuming an isotropic material that behaves as a neo-Hookean incompressible solid, the elastic modulus, E was approximated to be 189.8 and 152.9 kPa for the equilibrated and cured gels respectively. Through the application of equation 3 and knowledge of the volume fraction parameters ($\nu_{2,r} = 0.221$, $\nu_{2,s} = 0.376$) the percentage of elastically effective chains was calculated to be approximately 11 % of the total number of initial chains ($\nu_e \sim 0.021$ mol L^{-1}) and was consistent in both the cured and equilibrium states. The extent of reaction was calculated to be approximately 96.98 % based on the theory of Miller-Macosko, but the number of elastically effective chains was overestimated to be 0.15 mol L^{-1} using this model. By taking the root mean squared value of the distance between crosslinks, the mesh size of the system was approximated at 7 nm and 6.9 nm in the cured and equilibrium states respectively.

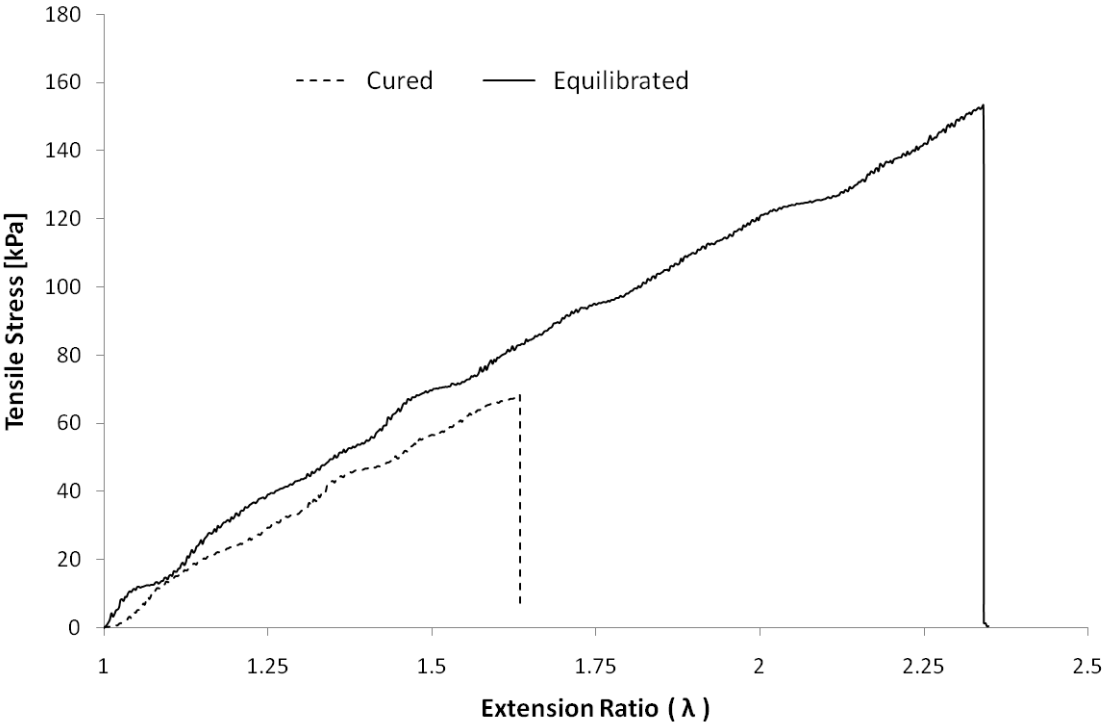

Figure 10. Tensile testing of hydrogels. Graph shows tensile stress versus extension ratio for cured and equilibrated hydrogels. Sample curves are shown for specimens that displayed median terminal elongation for each type.

Table 1. Mechanical properties of hydrogels. Collated data from tensile tests on cured and equilibrated hydrogels is compared with calculated ideal values for Affine and Phantom network models derived from Miller-Macosko theory using the experimentally determined sol fraction. Error is standard deviation, n=4 for cured gels, n=6 for swollen gels.

Hydrogel Type	Shear Modulus (G) [kPa]	Elastic Modulus (E) [kPa]	Ideal Shear Moduli (Affine and Phantom Models) [kPa]	Ultimate Tensile Strength [kPa]	Terminal Extension Factor (λ)
Cured (n=4)	50.98 ± 1.42	152.9 ± 2.5	382.1 and 127.4	66.8 ± 6.9	1.637 ± 0.067
Equilibrated (n=6)	63.26 ± 2.13	189.8 ± 3.7	456.2 and 152.1	141.7 ± 21.2	2.232 ± 0.220

Evaluation of drug delivery and tissue engineering applications in vitro

Release of Methylprednisolone sodium succinate from the hydrogels

The degradation constant for MPSS in PBS was determined as $5.98 \pm 0.50 \times 10^{-3}$ hour^{-1} by exponential regression ($R^2 = 0.997$, Fig. 11A). By solution of ordinary differential equations for mass transfer and degradation, the degradation constants in the gel and mass transfer coefficients were calculated by regression (Fig. 11B). The determined mass transfer coefficient was $1.54 \pm 0.29 \times 10^{-4}$ hour^{-1} while the degradation constant for MPSS in the gels was $3.12 \pm 0.10 \times 10^{-3}$ hour^{-1}. Using these two coefficients, the drug release was predicted for infinite sink conditions (Fig. 11C).

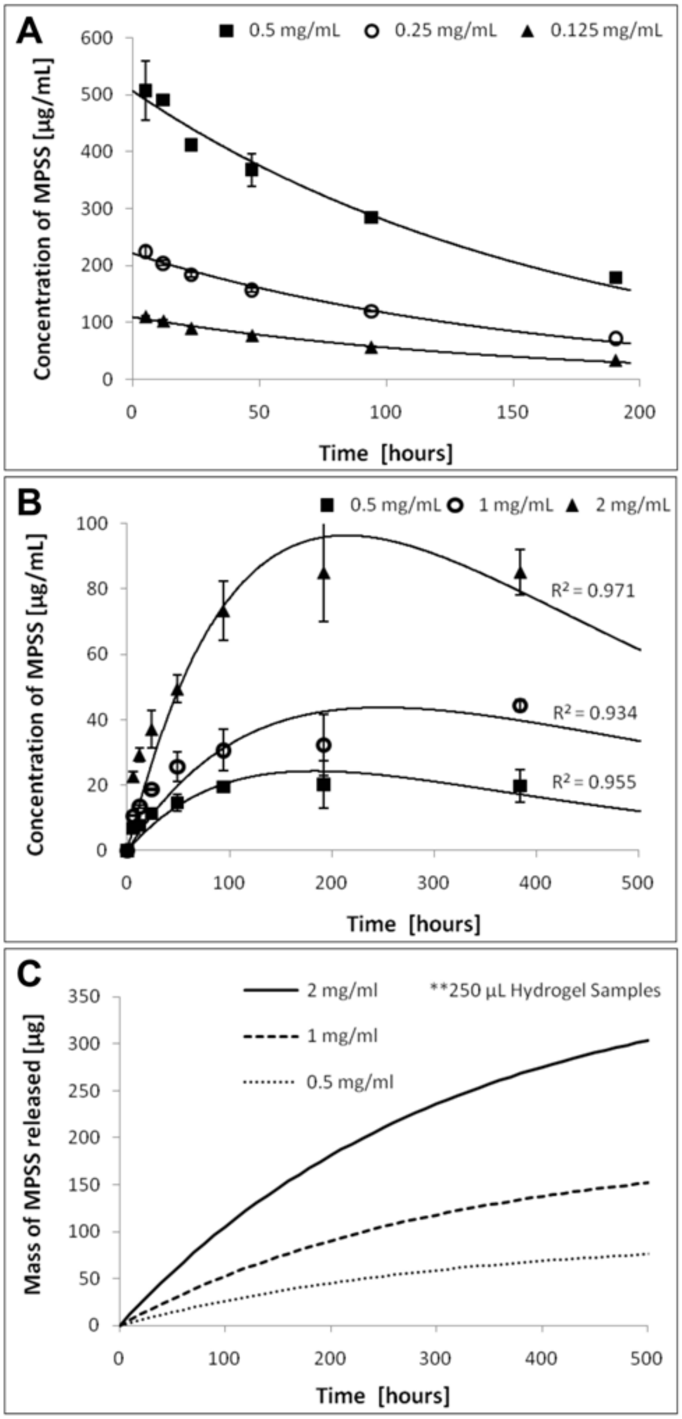

Figure 11. Controlled release of Methylprednisolone Sodium Succinnate (MPSS) from hydrogels in PBS (pH 7.4) at 37 ºC. **A.** Degradation of MPSS in PBS for three concentrations (0.125, 0.25 and 0.5 mg/ml). **B.** Release profile of MPSS from hydrogels for three concentrations (0.5, 1, 2 mg/ml). Graph displays experimental data for the release into PBS, including degradation of MPSS. n=3 for each time point and concentration. **C.** Predicted drug release from the hydrogels into an infinite sink, corrected for degradation of MPSS in PBS.

Cell adhesion mediated by peptide functionalization

Functionalization of hydrogels by incorporation of an oligolysine peptide (Cys-(Lys)$_{14}$-Cys) was performed to promote cell adhesion on the hydrogels (Fig. 12). No cell attachment was observed for hydrogels with zero or 5 μg/mL Cys-(Lys)$_{14}$-Cys. Attachment and process extension of cultured murine mesenchymal stem cells was observed for hydrogels containing 50 μg/mL, with a similar conformation to cells in uncoated wells. A concentration of 500 μg/mL caused the cells to adhere to the gel but form spherical conformations without process extension.

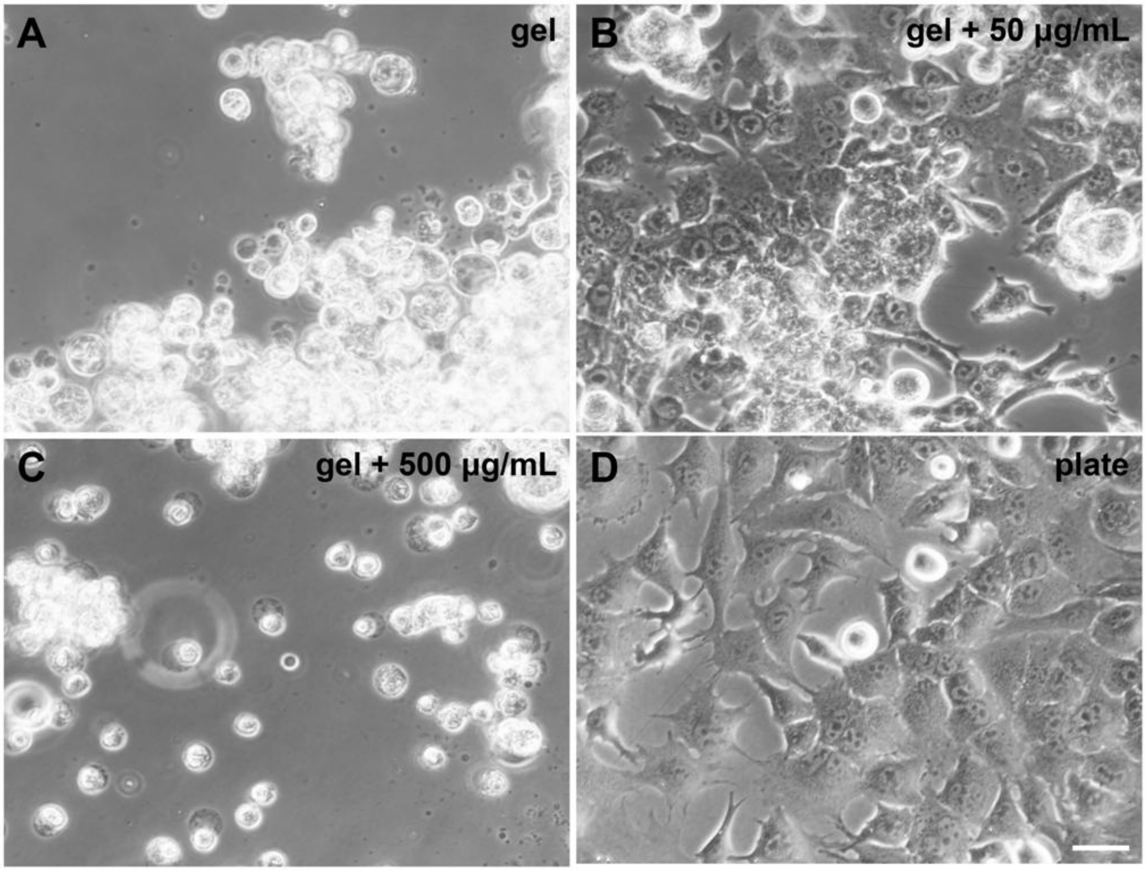

Figure 12. Functionalization of hydrogels to promote cell adhesion. 24 well polystyrene tissue culture plate was coated with 200 µL 25 wt.% thiol-acrylate hydrogels cured in 1XPBS (solvent exchanged to 1x DMEM medium just prior to testing) containing Cys-(Lys)$_{14}$-Cys at different concentrations (A, B, C) or wells left untreated (D). Murine mesenchymal stem cells (mMSC) were seeded 10^5 cells per well. 40x Phase 2 contrast light microscope images, 24 hours post-seeding. Hydrogels containing 50 µg/mL promotes mMSC adhesion and process extension. n=4 for each group.

Discussion

Thermodynamic considerations of ETTMP in PBS

Successful preparation of the hydrogels was found to be dependent on the solubility of the ETTMP in the solvent, which was shown to have a non-linear dependence on concentration in PBS at 4 ºC (Fig. 2). In unsuccessful attempts, precipitation of the polymer at 37°C occurred during chemical reaction, resulting in incomplete conversion and a high sol fraction. Assessing the stability of ETTMP in PBS when heated from 4 to 37 ºC provided a practically relevant indication of solubility throughout the gelation period at physiological temperature. It is well understood that polymers containing ethylene glycol units exhibit a concentration dependent lower critical solution temperature (LCST) [31]. Visible light absorbance data of ETTMP in PBS during heating was fitted to an error function, where the inflection point signifies 50 percent precipitation. Therefore, a characteristic error function was observed as the cumulative function when a lower critical solution temperature was reached and phase separation occurs [32]. The solubility of ETTMP in PBS appeared to be improved upon mixing with PEG-400-DA solution and was maintained throughout the complete gelation process as long as the mixture was maintained at 4 °C for the initial five minutes.

Physical chemistry of gelation mechanism

Understanding the timeline of hydrogel formation was of critical importance for determining its practical use as an injectable biomedical material. Dynamic rheological measurements was a convenient means of assessing the gelation kinetics of the hydrogel system and provided insight into the mechanism of gelation through the control of various gelation parameters such as pH, temperature and macromer stoichiometry [25, 33]. The characteristic hydrogel formation response of the current system, as depicted in Figure 6, can be described by standard branch gelation theory developed by Flory and Stockmayer [27, 34].

The data presented in Figure 7 provides support for a conjugate Michael addition reaction mechanism between a thiolate and the activated unsaturated carbon double-bond of the acrylate. The gelation time, or reaction rate, was linearly dependent on the concentration of protons and corresponding thiolate anions in solution. While a pK_a of 9.87 indicates that a small proportion of thiol groups in ETTMP are dissociated in pH 7.4 PBS, thiolate anions will continue to be produced under rapid equilibration with their rate of consumption according to Le Châtelier's principle. The small variation in gelation time and physical properties with the inclusion of a radical inhibitor MEHQ in PBS indicated that a radical thiyl-acrylate reaction mechanism was not kinetically competitive with the addition mechanism. This is advantageous in the minimization of transient free radical production *in situ*, compared to approaches using photoinitiators and UV light.

Mechanical properties

The PEG-400-DA/ETTMP hydrogel exhibited a de-swelling property during equilibration at 37 ºC. This can be attributed to the LCST of the PEG based precursors. In addition, a relief of tension was observed, as the hydrogels were separated from the walls of their molds during removal, indicating residual tensile stress after curing. This characteristic makes it a candidate material for applications where pressure exerted by hydrogel swelling may cause severe nerve damage [14-17].

Biomaterials often require a resorbable capacity *in vivo* following the completion of their desired function so as to minimize the extent of the induced foreign body response. Poly(α-hydroxy esters) have been incorporated into the PEG based system to increase the rate of hydrolytic degradation [35]. The PEG-DA-400/ETTMP system contains ester bonds, allowing the material to resorb within an estimated 12-months *in vitro*. However, the *in vitro* experiment does not account for many factors *in vivo* such as enzymatic and phagocytic activity as well as mechanical loading, which may increase the degradation rate. Due to the hydrophilic nature of PEG, bulk degradation is the predominate mechanism [36]. The linear profile of the macroscopic degradation curve for the hydrogel as depicted in Figure 9, may be attributed to the net result of two competing processes, namely first order hydrolysis and crosslink density reduction, which is stochastic in nature [37].

The mechanical properties of biomaterials can influence the phenotype and activity of local and systemic cells, dictating foreign body and wound healing responses. The developed hydrogel displays a modulus of elasticity of 189.8 kPa that is comparable, in magnitude, to a range of soft human tissues. It is important to note that the material failed to obtain mechanical properties close to the affine or phantom values predicted by the Miller-Macosko model (Table 1). This was attributed to a significant difference in the number of elastically active chains actually incorporated (11% of the initial chains, $\nu_e = 0.021$ mol L^{-1}) compared to that the model prediction (82%, $\nu_a = 0.15$ mol L^{-1}). However, this is to be expected due to a number of factors such as low volume fraction of polymer during curing, the use of low molecular weight macromers and the possibility of intramolecular reactions, which may all contribute to non-ideal network formation.

Sustained drug release

MPSS is a glucocorticoid prodrug, with anti-inflammatory and immunosuppressant properties, that is currently a clinical treatment option for acute traumatic spinal cord injury [38]. However, high-dose intravenous administration immediately post-injury is being widely abandoned by neurosurgeons due to complications associated with systemic immunosuppression, including increased risk of pneumonia and sepsis [39]. MPSS has a half-life of 109 hours in PBS at 37ºC. In aqueous media, the ester bond between the methylprednisolone and succinate hydrolyses, yielding free methylprednisolone (MP) which has limited solubility in PBS due to its hydrophobic nature. MP was likely not detected by HPLC for this reason in drug release experiments. In future experiments, it may be possible to measure MP by extraction with organic solvents. The drug release experiment was modeled using a system of ordinary differential equations to include rates of mass transfer, proportional to the MPSS concentration difference between the hydrogel and the PBS, and drug degradation in both the hydrogel and PBS. Experimental data were fitted to the solutions to determine the mass transfer coefficient and degradation constants. The degradation rates of MPSS in the PBS and hydrogel were modeled separately in the differential equations to assess whether encapsulation had a stabilizing effect on the active life of the drug. Regression analysis using the solution to the system of equations identified a lower degradation constant for MPSS in the hydrogel, suggesting that the material may create a protective environment that transiently impedes drug degradation. To predict the actual release profile of methylprednisolone *in vivo*, the equations were modified for an infinite sink and resolved using the determined constants. In reality, the sink conditions *in vivo* will deviate from this infinite sink approximation. A more accurate mathematical description would need to consider further the spatial dimensions of the system, account for interstitial diffusion and convection, as well as make concession for receptor binding and other biological processes. The hydrolysis of MPSS to MP once it has been released from the hydrogel is of little concern for local release systems as MP is the active form of the steroid and the limited aqueous solubility will not hinder activity. A key feature of the MPSS release profile from the current system is that the release time period is independent of the initial concentration in the hydrogel. For biomedical applications, this means that the drug dosage could be tailored to individual patients without increasing the volume of the drug depot required to administer it locally over a precise period of time.

Functionalization and cell adhesion

Whilst PEG is generally favored in biomedical applications because of limited protein adsorption, this can result in limited interaction with cells. To improve cell interactions, the hydrogel can be functionalized with peptides. One advantage of the PEG-DA-400/ETTMP hydrogel is that it involves thiol chemistry, which can be exploited to attach almost any compound with a thiol group, including any peptide containing cysteine to promote a specific cell response. Incorporation of an oligolysine peptide into the hydrogel promoted surface attachment of mMSCs in a concentration dependent manner *in vitro*. Polylysine was chosen as an initial proof of concept as it generally promotes cell adhesion, and in fact is used to promote neural stem cell attachment to culture plates [40, 41]. Others have shown that cell attachment on PEG based hydrogels can also be achieved using short peptide sequences from extracellular matrix proteins [42, 43]. The current nanoscale mesh size of the hydrogel (~6.9 nm) was too small for cellular ingrowth into the material. However, the small mesh size is advantageous for the characteristic de-swelling and drug release properties. Furthermore, a small mesh size may be useful to isolate encapsulated cells from a host immune system to prevent rejection. Recently, others have demonstrated incorporation of macroscopic pores or channels into similar hydrogels for cell ingrowth using sacrificial substrates of fibrin or poly(α-hydroxy esters) [44, 45]. However, utilizing these approaches would not preserve injectability. Future work towards use of this hydrogel in regenerative medicine will therefore focus on the development of procedures to create macroporous structures with controlled architecture *in situ* following injection and gelation.

Conclusion

This paper presents the rational design of a hydrogel, seeking to address the engineering challenges associated with clinical translation of injectable *in situ* gelling biomaterials. This poly(ethylene glycol) based hydrogel cross-linked in aqueous media via conjugate Michael addition reaction of thiol and acrylate groups, resulting in nearly complete conversion and minimal sol fraction. By selecting low molecular weights macromer precursors with favorable solvent interactions the hydrogel exhibited syneresis under simulated physiological conditions *in vitro*. The suitability of the material for sustained release of a hydrophilic small molecule drug, methylprednisolone sodium succinate, was demonstrated with high encapsulation efficiency and programmable dosage which facilitated release over a concentration independent timeline. Furthermore, incorporation of an oligolysine peptide promoted concentration dependent adhesion of murine mesenchymal stem cells *in vitro*.

Acknowledgements

We thank Dr. Arthur J. Coury (Boston, MA) for reviewing the manuscript and engaging in discussions. C.D.P. was supported by the MIT/CIMIT Medical Engineering Fellowship. T.M.O was supported by the General Sir John Monash Award. This research was sponsored by a gift to MIT by InVivo Therapeutics Corporation. This research was sponsored by the Armed Forces Institute of Regenerative Medicine award number W81XWH-08-2-0034. The U.S. Army Medical Research Acquisition Activity, 820 Chandler Street, Fort Detrick MD 21702-5014 is the awarding and administering acquisition office. The content of the manuscript does not necessarily reflect the position or the policy of the Government, and no official endorsement should be inferred.

Role of the funding source

InVivo Therapeutics Corporation provided assistance determining the general design of this study to develop a novel injectable hydrogel.

References

1. Drury JL, Mooney DJ. Hydrogels for tissue engineering: scaffold design variables and applications. Biomaterials 2003;24(24):4337-4351.
2. Lin C-C, Anseth K. PEG Hydrogels for the Controlled Release of Biomolecules in Regenerative Medicine. Pharm Res 2009;26(3):631-643.
3. Slaughter BV, Khurshid SS, Omar ZF, Khademhosseini A, Peppas NA. Hydrogels in Regenerative Medicine. Adv Mater 2009;21(32-33):3307-3329.
4. Chapman RG, Ostuni E, Liang MN, Meluleni G, Kim E, Yan L, et al. Polymeric Thin Films That Resist the Adsorption of Proteins and the Adhesion of Bacteria. Langmuir 2001;17(4):1225-1233.
5. Pathak CP, Sawhney AS, Hubbell JA. Rapid photopolymerization of immunoprotective gels in contact with cells and tissue. J Am Chem Soc 1992;114(21):8311-8312.
6. Salinas CN, Anseth KS. Mixed Mode Thiol,àíAcrylate Photopolymerizations for the Synthesis of PEG,àíPeptide Hydrogels. Macromolecules 2008;41(16):6019-6026.
7. Rydholm AE, Bowman CN, Anseth KS. Degradable thiol-acrylate photopolymers: polymerization and degradation behavior of an in situ forming biomaterial. Biomaterials 2005;26(22):4495-4506.
8. Lee TY, Roper TM, Jonsson ESn, Guymon CA, Hoyle CE. Thiol-Ene Photopolymerization Kinetics of Vinyl Acrylate/Multifunctional Thiol Mixtures. Macromolecules 2004;37(10):3606-3613.
9. DeForest CA, Polizzotti BD, Anseth KS. Sequential click reactions for synthesizing and patterning three-dimensional cell microenvironments. Nat Mater 2009;8:659 - 664.
10. Lutolf MP, Hubbell JA. Synthesis and Physicochemical Characterization of End-Linked Poly(ethylene glycol)-co-peptide Hydrogels Formed by Michael-Type Addition. Biomacromolecules 2003;4(3):713-722.
11. Elbert DL, Pratt AB, Lutolf MP, Halstenberg S, Hubbell JA. Protein delivery from materials formed by self-selective conjugate addition reactions. J Control Release 2001;76(1-2):11-25.
12. Cushing MC, Anseth KS. MATERIALS SCIENCE: Hydrogel Cell Cultures. Science 2007;316(5828):1133-1134.
13. Sawhney AS, Pathak CP, Hubbell JA. Bioerodible hydrogels based on photopolymerized poly(ethylene glycol)-co-poly(.alpha.-hydroxy acid) diacrylate macromers. Macromolecules 1993;26(4):581-587.
14. Thavarajah DM, De Lacy PM, Hussain RM, Redfern RMF. Postoperative Cervical Cord Compression Induced by Hydrogel (DuraSeal): A Possible Complication. Spine;35(1):E25-E26.
15. Blackburn Sl, Smyth MD. Hydrogel-induced cervicomedullary compression after posterior fossa decompression for Chiari malformation. J Neurosurg Pediatr 2007;106(4):302-304.

16. Roldan-Pallares M, del Castillo Sanz JL, Awad-El Susi S, Refojo MF. Long-term Complications of Silicone and Hydrogel Explants in Retinal Reattachment Surgery. Arch Ophthalmol 1999;117(2):197-201.
17. Hwang KI, Lim JI. Hydrogel Exoplant Fragmentation 10 Years After Scleral Buckling Surgery. Arch Ophthalmol 1997;115(9):1205-1206.
18. Bakshi A, Fisher O, Dagci T, Himes BT, Fischer I, Lowman A. Mechanically engineered hydrogel scaffolds for axonal growth and angiogenesis after transplantation in spinal cord injury. J Neurosurg Spine 2009;1(3):322-329.
19. Pathak CP, Barman SP, Philbrook MC, Sawhney AS, Coury AJ, Avila LZ, et al. Multiblock biodegradable hydrogels for drug delivery and tissue treatment. US Patent No. 0072961, 2001.
20. Klimo P, Jr., Khalil A, Slotkin JR, Smith ER, Scott RM, Goumnerova LC. Wound Complications Associated With the Use of Bovine Serum Albumin-Glutaraldehyde Surgical Adhesive in Pediatric Patients. Neurosurgery 2007;60(4):305-309.
21. Metters A, Hubbell J. Network Formation and Degradation Behavior of Hydrogels Formed by Michael-Type Addition Reactions. Biomacromolecules 2004;6(1):290-301.
22. Lowe AB. Thiol-ene "click" reactions and recent applications in polymer and materials synthesis. Polym Chem 2010;1:17-36.
23. Mather BD, Viswanathan K, Miller KM, Long TE. Michael addition reactions in macromolecular design for emerging technologies. Prog Polym Sci 2006;31(5):487-531.
24. Smith MD. High-performance liquid chromatographic determination of hydrocortisone and methylprednisolone and their hemisuccinate esters in human serum. J Chromatogr B 1979;164(2):129-137.
25. Chambon F, Winter HH. Linear Viscoelasticity at the Gel Point of a Crosslinking PDMS with Imbalanced Stoichiometry. J Rheol 1987;31(8):683-697.
26. Winter HH. Can the gel point of a cross-linking polymer be detected by the G' - G" crossover? Polym Eng Sci 1987;27(22):1698-1702.
27. Flory PJ. Principles of polymer chemistry. Ithaca, N.Y.: Cornell University Press, 1953.
28. Treloar LRG. The physics of rubber elasticity. 2d ed. Oxford,: Clarendon Press, 1958.
29. Gnanou Y, Hild G, Rempp P. Molecular structure and elastic behavior of poly(ethylene oxide) networks swollen to equilibrium. Macromolecules 1987;20(7):1662-1671.
30. Miller DR, Macosko CW. A New Derivation of Post Gel Properties of Network Polymers. Macromolecules 1976;9(2):206-211.
31. Kjellander R, Florin E. Water structure and changes in thermal stability of the system poly(ethylene oxide)–water. J Chem Soc Farad T 1 1981;77(9).
32. Barnes MD, Ng KC, Fukui K, Sumpter BG, Noid DW. Probing Phase-Separation Behavior in Polymer-Blend Microparticles: Effects of Particle Size and Polymer Mobility. Macromolecules 1999;32(21):7183-7189.

33. Chiou B-S, English RJ, Khan SA. Rheology and Photo-Cross-Linking of Thiol-ene Polymers. Macromolecules 1996;29(16):5368-5374.

34. Stockmayer WH. Theory of Molecular Size Distribution and Gel Formation in Branched-Chain Polymers. J Chem Phys 1943;11(2):45-55.

35. West JL, Hubbell JA. Photopolymerized hydrogel materials for drug delivery applications. React Polym 1995;25(2-3):139-147.

36. Sawhney AS, Pathak CP, Hubbell JA. Bioerodible hydrogels based on photopolymerized poly(ethylene glycol)-co-poly(α-hydroxy acid) diacrylate macromers. Macromolecules 1993;26(4):581-587.

37. Metters AT, Anseth KS, Bowman CN. Fundamental studies of a novel, biodegradable PEG-b-PLA hydrogel. Polymer 2000;41(11):3993-4004.

38. Bracken MB, Shepard MJ, Collins WF, Holford TR, Young W, Baskin DS, et al. A randomized, controlled trial of methylprednisolone or naloxone in the treatment of acute spinal-cord injury. Results of the Second National Acute Spinal Cord Injury Study. N Engl J Med 1990;322(20):1405-1411.

39. Hugenholtz H. Methylprednisolone for acute spinal cord injury: not a standard of care. C Med Assoc J 2003;168(9):1145-1146.

40. Yavin E, Yavin Z. Attachment and culture of dissociated cells from rat embryo cerebral hemispheres on polylysine-coated surface. J Cell Biol 1974;62(2):540-546.

41. Banker GA, Cowan WM. Rat hippocampal neurons in dispersed cell culture. Brain Res 1977;126(3):397-425.

42. Burdick JA, Anseth KS. Photoencapsulation of osteoblasts in injectable RGD-modified PEG hydrogels for bone tissue engineering. Biomaterials 2002;23(22):4315-4323.

43. Lutolf MP, Lauer-Fields JL, Schmoekel HG, Metters AT, Weber FE, Fields GB, et al. Synthetic matrix metalloproteinase-sensitive hydrogels for the conduction of tissue regeneration: Engineering cell-invasion characteristics. P Natl Acad Sci USA 2003;100(9):5413-5418.

44. Ford MC, Bertram JP, Hynes SR, Michaud M, Li Q, Young M, et al. A macroporous hydrogel for the coculture of neural progenitor and endothelial cells to form functional vascular networks invivo. P Natl Acad Sci USA 2006;103(8):2512-2517.

45. Namba RM, Cole AA, Bjugstad KB, Mahoney MJ. Development of porous PEG hydrogels that enable efficient, uniform cell-seeding and permit early neural process extension. Acta Biomater 2009;5(6):1884-1897.

II.

Establishing a model spinal cord injury in the African green monkey for the preclinical evaluation of biodegradable polymer scaffolds seeded with human neural stem cells

Christopher D Pritchard (1), Jonathan R Slotkin (2), Dou Yu (3), Haining Dai (4), Matthew S Lawrence (5), Roderick T Bronson (6), Francis M Reynolds (7), Yang D Teng (3), Eric J Woodard (8), Robert S Langer (1)

(1) Department of Chemical Engineering
Massachusetts Institute of Technology, Cambridge, MA 02139

(2) Department of Neurosurgery
The Washington Brain and Spine Institute, Washington, DC 20010

(3) Department of Neurosurgery
Brigham and Women's Hospital, Boston, MA

(4) Department of Neuroscience
Georgetown University Medical Center, Washington, DC

(5) RxGen, Inc., Hamden, CT

(6) 6 Department of Pathology
Harvard Medical School, Boston, MA

(7) InVivo Therapeutics Corporation
Cambridge, MA 02141

(8) Department of Neurosurgery
New England Baptist Hospital, Cambridge, MA 02120

Reprinted with permissions from Elsevier: J Neurosci Methods. 2010 May 15;188(2):258-69.

Abstract

Given the involvement of post-mitotic neurons, long axonal tracts and incompletely elucidated injury and repair pathways, spinal cord injury (SCI) presents a particular challenge for the creation of preclinical models to robustly evaluate longitudinal changes in neuromotor function in the setting in the presence and absence of intervention. Whilst rodent models exhibit high degrees of spontaneous recovery from SCI injury, animal care concerns preclude complete cord transsections in nonhuman primates and other larger vertebrate models. To overcome such limitations a segmental thoracic (T9-T10) spinal cord hemisection was created and characterized in the African green monkey. Physiological tolerance of the model permitted behavioral analyses for a prolonged period post-injury, extending to predefined study termination points at which histological and immunohistochemical analyses were performed. Four monkeys were evaluated (one receiving no implant at the lesion site, one receiving a poly(lactide-co-glycolide) (PLGA) scaffold, and two receiving PLGA scaffolds seeded with human neural stem cells (hNSC)). All subjects exhibited Brown-Séquard syndrome two days post-injury consisting of ipsilateral hindlimb paralysis and contralateral hindlimb hypesthesia with preservation of bowel and bladder function. A 20-point observational behavioral scoring system allowed quantitative characterization of the levels of functional recovery. Histological endpoints including silver degenerative staining and Iba1 immunohistochemistry, for microglial and macrophage activation, were determined to reliably define lesion extent and correlate with neurobehavioral data, and justify invasive telemetered electromyographic and kinematic studies to more definitively address efficacy and mechanism.

Introduction

Spinal cord injury (SCI) results from penetrating or compressive traumatic injury to the spine or from compressive lesions associated with neoplastic growth or vertebral dislocation. Neuronal injury and recovery is critically guided and impacted by the surrounding cells and extracellular environment within the spinal cord and adjacent tissues, reducing the utility of *in vitro* assays, and necessitating the study of injury mechanisms and spinal cord physiology in *in vivo* vertebrate models (Feringa et al., 1975; Hall and Springer, 2004; Jones et al., 2005; Liverman et al., 2005; Thuret et al, 2006; Baptiste and Fehlings, 2007; Rossignol et al. 2007). A recent review of data derived from the extensive literature related to the modeling of SCI to better understand mechanisms of injury and repair has highlighted the greater relevance and utility of nonhuman primate models relative to rodents and other vertebrate species in the preclinical investigation of therapeutic interventions (Courtine et al., 2007). Rodents may over-predict the efficacy of interventions given high rates of spontaneous recovery from induced spinal cord injury, even following profound lesions. The spinal cord anatomy and physiology of old world monkeys are more similar to humans, particularly with respect to the position and function of corticospinal tracts (Courtine et al., 2007). This permits a more critical evaluation of results from preclinical studies, facilitating translation to humans. Here we report the development of a surgical model of acute SCI in the African green monkey (*chlorocebus sabaeus*) for the evaluation of biomaterial implants as a translational interval between rodent and clinical investigations. Poly(lactide-co-glycolide) (PLGA) biocompatible and biodegradable porous scaffolds seeded with neural stem cells (NSC) have demonstrated potential as a strategy for the treatment of central nervous system lesions (Flax et al., 1998; Park et al., 2002). A PLGA scaffold seeded with murine NSC (mNSC) promoted long-term functional improvements in an adult rat hemisection model of SCI as compared to controls (Teng et al., 2002). 70 days post-injury, treated animals exhibited coordinated, weight-bearing hindlimb stepping. Histological and immunocytochemical analysis suggested the recovery may have been associated with a reduction in tissue loss, possibly resulting from modulation of secondary injury mechanisms and reduced astrogliosis.

To establish an SCI model in which this possibility might be critically evaluated, a lateral hemisection at level T9-10 in the thoracic spine was created in the monkey, with removal of the ipsilateral T9-T10 segment. This approach bears some similarity to previously published models, where ipsilateral tracts were transected without removal of a full segment or only particular tracts (lateral corticospinal efferents, dorsal funiculus afferents) were targeted (Crowe et al., 1997; Babu et al., 2000; Edgerton et al., 2004). The lesion was designed to result in Brown-Séquard syndrome, characterized in humans at comparable cord levels by paralysis of the ispilateral leg, loss of ipsilateral muscle tone in the lower abdomen (innervated by T9-L1), loss of vibration and position sensation in the ipsilateral hindlimb, loss of thermal and mechanical pain sensation in the contralateral leg, lumbar and sacral dermatomes and ipsilateral lower thoracic dermatomes, and spastic paresis in the ipsilateral leg resulting in increased knee and ankle jerk reflexes with retention of monosynaptic reflexes involving the lower motor neurons (Brown-Séquard, 1851). Importantly, a unilateral restriction of the lesion was implemented with the additional aim of sparing bladder function and anal muscle tone by allowing compensatory innervation by retained contralateral corticospinal efferents. Evaluation of loss and recovery of these multiple lower extremity functions may permit objective measures of the efficacy of the therapeutic intervention with minimal post-operative complications.

In addition to establishing methodologies for the generation of a discrete unilateral cord lesion designed to minimize special animal care requirements, behavioral and histological endpoints were evaluated for their utility in differentiating treatment outcomes. Neuromotor and histopathological endpoints were assessed across multiple time points following introduction of a PLGA scaffold, PLGA scaffold seeded with hNSC, or no implant.

Materials and methods

Hemisection model

Four juvenile male African Green monkeys ranging in weight from 2.3 to 2.7 kg were employed in the study. Subjects were between 1.8 to 2.0 years old. Baseline clinical and neurological exams confirmed good health and suitability for study enrollment. Treatment allocation was performed arbitrarily with respect to weight. All experimental and surgical procedures were carried out in accordance with the Guide for the Care and Use of Laboratory Animals (National Academy Press, revised 1996) and the Institutional Animal Care and Use Committee (IACUC) of the St. Kitts Biomedical Research Foundation, where the study was conducted.

To perform the hemisection lesion, monkeys were sedated with ketamine/xylazine i.m., and kept on a 0.9% saline drip. Isoflourane anesthesia was applied with depth of anesthesia monitored throughout the study. Deep-dermal or subcutaneous bleeding was controlled using electrocautery following skin incision. The laminectomy was performed by an en-bloc, lateral lamina cut method. Following bone removal, the dural opening was performed with a #15 surgical blade. Dural edges were tacked to the surrounding ligaments or musculature with 4.0 non-absorbable sutures. The midline of the spinal cord was carefully assessed with the visualization of anatomic landmarks. At all times, spinal cord veins and surface vessels were spared unless it was absolutely necessary that they be controlled. The segmental hemisection lesion was microscopically performed with the use of microneurosurgical dissection instruments and micro-suction aspiration. A transverse incision extending to the midline was made at the caudal point of the intersection of the T9 dorsal root with the cord and at the rostral point of the intersection of the T10 dorsal root with the cord, followed by a midline incision extending between those levels.

Hemi-cord parenchyma resection to these defined boundaries ensured complete transection to the anatomic midline in a lesion extending 10mm in length, without damage to the contralateral hemi-cord. At this point in the procedure, if designated, a scaffold was implanted (Figure 1). The scaffold was sized to fill the hemisection cavity, without exerting pressure on the surrounding host tissue during or following insertion. When this process was complete, the dural tack-up sutures were removed, and the dura was closed with a 4.0 non-absorbable single running suture. Fibrin tissue sealant was applied to the dural suture line. The fascia was then closed with interrupted 3.0 absorbable sutures. After this layer was closed, the subcutaneous layers were re-approximated with 3.0 absorbable sutures. Then, the deep dermal layer was brought together with interrupted 3.0 absorbable sutures. After successful extubation and recovery from anesthesia, a neurologic examination was performed. Vital signs were monitored in a manner consistent with standard human post-anesthesia care. Following recovery from anesthesia the monkeys were returned to their cage with a mattress placed on the floor to minimize pressure sore risk. Monkeys were observed twice daily to assess skin integrity and exclude the possibility of autophagy, which can be observed in the setting of limb denervation. All monkeys additionally received a pre and postoperative course of immunosuppressants, consisting of cyclosporine (0.6 mg/kg), prednisolone (0.3 mg/kg) and azathioprine (0.5 mg/kg) i.m. BID starting 3 days before implantation and continuing until sacrifice to prevent hNSC rejection. Though this immunosuppressant regimen had been previously established to be well tolerated, additional attention and vigilance was maintained to prevent opportunistic infections.

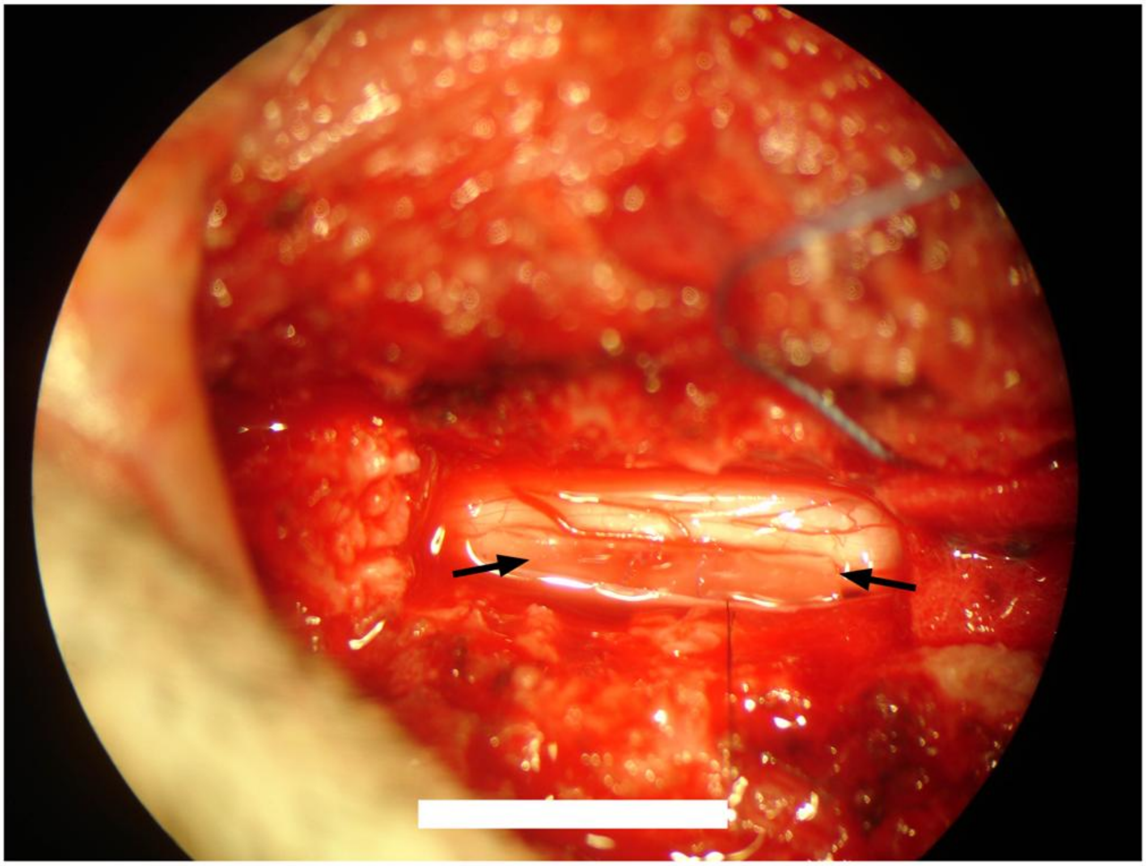

Figure 1. Photograph through surgical microscope of scaffold implanted into T9-T10 hemisection lesion. Arrow indicated scaffold position. Scale bar = 10 mm.

Neuromotor video recordings

Video recordings of quadrupedal locomotion were generated for qualitative and quantitative assessment of gait and posture deficiencies associated with motor impairment of the ipsilateral hindlimb. To document locomotion, the monkeys were placed in an 8 by 2.5 by 2 foot ambulation chamber. One long side of the chamber was made of Plexiglas^{TM} to allow visualization of the monkey as it navigated the enclosure. Movements were recorded by video continuously for a four-minute period with the entire width of the enclosure captured in the camera's field of view under optimized illumination. At the end of the four-minute video segment a food reward was introduced to the chamber through an aperture in the ceiling to promote and document upright standing, after which another 4 minutes of close-up video of the monkey was obtained. Video sessions were conducted prior to surgery, postoperative days 2, 3, 4, 6 and 10 and then weekly for 6 weeks and prior to sacrifice.

Video data were reviewed and rated by a blinded reviewer, not involved in the *in vivo* execution of the study. Ratings for each video session were based on review of the combined four-minute video segments collected during the wide field and close-up recordings. Ratings generated an overall observational neuromotor score for the ipsilateral and contralateral hindlimbs (Table 1). The rating scale incorporates the components derived from the spectrum of behaviors and motions observed in healthy African green monkeys and was based on previously established methods for observational scoring (Basso et al., 1996; Babu et al., 2000).

Table 1. Ambulation chamber video observational neuromotor score.

Scale	Description
0	no voluntary function
1	slight one or two joints movement
2	active one or two joints, slight movement others
3	active movement of all three joints, no weight bearing
4	slight weight bearing, consistent dorsal stepping (no plantar stepping)
5	slight weight bearing, occasional plantar stepping
6	frequent plantar stepping, occasional weight bearing, hops with partial weight support
7	frequent plantar stepping and weight bearing, occasional FL-HL coordination,
8	consistent plantar stepping and partial weight supported steps, occasional FL-HL coordination
9	frequent partial weight supported steps, occasional FL-HL coordination
10	occasional partial weight supported steps, frequent foot drop and/or drag, run with partial weight support
11	occasional partial weight supported steps, frequent FL-HL coordination
12	slight partial weight supported steps, frequent FL-HL coordination,stands up HL with partial weight support
13	slight partial weight supported steps, consistent FL-HL coordination, frequent foot drop and/or drag
14	full weight supported steps and consistent FL-HL coordination, occasional foot drop and/or drag
15	occasional foot drop and/or drag, stand up HL with full weight support
16	slight foot drop and/or drag, no toe clearance
17	no foot drop and/or drag, no toe clearance
18	occasional toe clearance
19	frequent toe clearance
20	normal

Histology & immunohistochemistry

On the study day indicated in Table 2, the monkeys were euthanized with intravenous sodium pentobarbital followed by whole body perfusion fixation with 4% paraformaldehyde. Animals were examined carefully for external abnormalities including hair loss or decubitus ulcers at bony prominences, palpable masses, and abnormalities in the abdominal, thoracic, and cranial cavities. The sciatic nerves, spinal cord and brain were dissected en masse and fixed overnight in 4% paraformaldehyde, following which specimens were transferred to phosphate buffered saline.

The fixed tissue was treated overnight with 20 % glycerol and 2 % dimethylsulfoxide and embedded in a gelatin matrix using MultiBrain^{TM} (NeuroScience Associates, Knoxville, TN). After curing in weak formaldehyde solution, the block was rapidly frozen by immersion in 2-methyl butane chilled to -70 °C with crushed dry ice and mounted on an A860 sliding microtome. The block was sectioned to generate alternating 40 µm sagittal and coronal sections spanning the lesion site as well as cervical, thoracic and lumbar regions rostral and caudal to the lesion. For each stain, every 24th section at 720 µm intervals was mounted and processed, yielding approximately 20 individual sections mounted on 10 slides. For ionized calcium-binding adapter molecule (Iba1) staining, sections were stained free-floating. Sections were treated with hydrogen peroxide and blocking serum, and immunostained with a 1:15,000 dilution of primary polyclonal rabbit anti-Iba1 antibody (#01973, WAKO, wakousa.com), a goat anti-rabbit secondary antibody, and an avidin-biotin-HRP complex (Vectastain ABC kit, Vector, Burlingame, CA). Incubation times were 24 hours (4 °C) for the primary antibody, 30 minutes (room temperature) for the secondary antibody, and 1 hour (room temperature) for the avidin-biotin-HRP complex. Sections were subsequently treated with diaminobenzidine tetrahydrochloride (DAB) and mounted on gelatinized (subbed) glass slides. Amino cupric silver staining was performed as described previously (de Olmos et al., 1994).

Table 2. Study animal summary.

Monkey	**Weight (kg)**	**Sex**	**Treatment group**	**Surgery date**	**Sacrifice date**	**Sacrifice day**
Y464	2.80	M	Scaffold alone	4/19/08	7/11/08	83
X992	2.74	M	Scaffold+hNSC	4/19/08	5/29/08	40
Y156	2.34	M	Control	4/20/08	8/8/08	111
Y430	2.79	M	Scaffold+hNSC	4/20/08	7/11/08	82

Adobe Photoshop Creative Suite 4 Extended was used for cord image compilation and analysis. For each cord, the original 8-10 microscopic images of the sections containing the lesions were consolidated using *Photomerge* in the *reposition* layout, shown in Figure 9. Guidelines for cord lengths and widths were formulated using the straight *line tool*, and their pixel measurements were taken using *Ruler tool*. For lesion areas, original cord border was approximated with the outline of the spared portion as a reference with the help of the *magnetic lasso* under 10% contrast settings and the *brush*. Area measurements with square pixel units were taken using the *magnetic lasso* and *record measurements* with *area data points*.

Due to the curvature of both X992 and Y156, the cord images were straightened out to obtain more realistic data for quantification of lesion dimensions. While keeping cord width constant between the original and modified images, *warp* was used to straighten out the image and prepare it for measurements.

All data was converted from pixel units to metric units using measurements recorded from the original cord samples. Cord widths were then normalized to 6 mm for all samples, to enable comparison and remove histological artifact. Linear and area dimensions were adjusted accordingly and summarized in Table 3.

Poly(lactide-co-glycolide) implants

Poly(lactide-co-glycolide) (PLGA) polymer porous scaffolds were prepared in a similar manner to previously published protocols (Mikos et al., 1992; Lavik et al., 2002; Teng et al., 2002). The implant was sized to precisely fit the spinal cord cavity, created by the segmental hemisection surgical resection. The size of the lesion was determined prior to live surgery by measurement of the spinal cord of a cadaver African Green monkey, of similar weight to the enrolled subjects. The ratio of lactic to glycolic acids units in the PLGA was chosen in order for the scaffold to degrade over a period of four to eight weeks *in vivo* (Sung et al., 2004). PLGA with a lactide/glycolide ratio of 50:50 and intrinsic viscosity 0.55-0.75 dL/g was obtained from Lactel (Durect, Pelham, AL). Thin polymer foams were fabricated by solvent casting/particulate leaching. PLGA was dissolved in chloroform (Sigma, St. Louis, MO) to obtain a 5 % wt./vol. stock solution. The stock solution was mixed with sodium chloride (particle size 180-450 µm by sieving; Sigma) in a 1:1.67 ratio (3 mL / 5 g) and poured into a 5.5 cm diameter Teflon^{TM} mold. After chloroform was evaporated in a fume hood for 48 hours, the salt particles were leached out by immersion in distilled water for 48 hours at room temperature. The water was changed every 4-8 hours during the leaching period. Subsequently, PLGA foam disks were dried on blotting paper and lyophilized overnight to remove residual water. The process yielded highly porous foam with a thickness of 1 mm. The foams were cut into segments (5 cm by 2 cm) with a surgical razor blade (VWR, West Chester, PA) and stored in 50 mL polypropylene Falcon test tubes (BD Biosciences, San Jose, CA) in a secondary container over anhydrous calcium sulfate (Drierite, Xenia, OH) at -20 °C until use.

Cell seeding on poly(lactide-co-glyolide) scaffolds

Scaffolds were trimmed to 5 mm by 12 mm by 1 mm, prior to seeding. As PLGA is hydrophobic, the scaffolds were immersed in 70% ethanol for 30 minutes on an orbital shaker at room temperature (Daigger, Vernon Hills, IL), for the purpose of removing air inside the pores, sterilizing the accessible surface for cell attachment, and pre-wetting the scaffolds prior to immersion in aqueous media (Mikos et al., 1992). The excess ethanol was then removed and the scaffolds were washed 3 times for 10 minutes in sterile phosphate buffered saline (PBS, pH 7.4, Invitrogen, Carlsbad, CA) solutions and transferred individually to sterile 2 mL Eppendorf™ centrifuge tubes (Daigger) containing 1.5 mL sterile PBS solutions with extracellular matrix

(ECM) adhesion molecules (10 μg/mL): poly-D-lysine (Sigma, St Louis, MO), laminin (BD Biosciences, San Jose, CA), and fibronectin (Sigma, St Louis, MO). Scaffolds were left overnight on a sterilized orbital shaker platform to ensure sufficient adsorption of the adhesion proteins on the accessible scaffold surface, as well as full hydration inside the scaffold pores. The following day, supernatant was removed, and the scaffolds were transferred to a 6 well culture plate (Falcon™, BD Biosciences, San Jose, CA), followed by two 5 minute rinses in fresh Neurobasal™ medium (with B27-A supplement, Invitrogen, Carlsbad, CA) on an orbital shaker (45 rpm).

Human neural stem cells (hNSC, clone HFB2050) were maintained in Falcon™ culture flasks in modified Neurobasal™ cell culture medium (with B27 supplements, antibiotics, heparin, and L-glutamine) in a humid incubator (37 °C, 5% CO_2) (Flax et al., 1998). Prior to seeding, cells were lifted from the flasks using Accutase™ (Innovative Cell Technologies, San Diego, CA), and concentrated to $5x10^5$ per mL to $1x10^6$ per mL via a series of centrifugation, cell counting, and re-suspension in fresh medium. The first time the scaffolds were seeded with hNSC is considered an acclimation seeding. For the acclimation seeding, 2 mL of $5x10^5$ per mL hNSC were used in each well in a 6 well plate. The plates were gently rotated in a sterilized humid chamber on an orbital shaker at 37 °C for 30 minutes (40 rpm). For subsequent cell seedings, 2 mL of $1x10^6$ per mL hNSC were used. Following the rotations, 3 mL of fresh modified Neurobasal™ medium were added to each well, and growth factors (20 ng/mL, basic fibroblast growth factor, bFGF, Calbiochem, San Diego, CA; 10 ng/mL, leukemia inhibitory factor, LIF, Chemicon, Temecula, CA; 20 ng/mL, epidermal growth factor, EGF, Invitrogen, Carlsbad, CA), and the plates were maintained in the incubator. The plates were observed under sterilized light microscope twice daily, and 2.5 mL of the 5 mL total culture medium in each well was replaced with fresh medium and new growth factors every 3 days. The seedings were repeated at total of 4 times (including the acclimation seeding) with an average interval of 1 week in between each seeding. Films of PLGA approximately 200 microns thick were sterilized in 70% ethanol and maintained in serum containing medium for one week.

At the end of the scaffold seeding period, light-field microscopy was carried out on scaffolds in the culture plates, and images of attached hNSC inside the scaffold pores were captured using an AxioCam™ MRc on an AxioVert™ S100 inverted microscope (Carl Zeiss Microimaging, Thornwood, NY). Representative scaffolds were then fixed in 4% paraformaldehyde at 4 °C overnight (on the same day as the surgeries were carried out using scaffolds from the same seeding wells), cryoprotected in 30% sucrose solution, embedded in OCT™ compound (Sakura Finetek, Torrance, CA), and cut into 20 µm thick serial sections for immunocytochemical (ICC) analysis. The scaffolds were oriented in the embedding compound in such a way that the sections are across the width (5 mm side) of the scaffold.

Microslides with scaffold sections were coverslipped with Fluorescent Mounting Medium with DAPI (Vector Labs, Burlingame, CA), and fluorescent images were captured via an AxioCam™ MRm on an AxioVert™ S100 inverted microscope (Carl Zeiss Microimaging) with a DAPI-specific color filter. Montage images of the entire cross section were created from multiple shots at 10 x magnification, which show clear identification of the nucleus of each attached hNSC. Occasionally, higher magnification images were captured in areas where too many cells cluster. The images were then printed inverted with high resolution so that each nucleus appears as a black dot. The total numbers of nuclei stained in each cross section were counted, and sections from the ends and the center of the scaffolds were used for this practice. The average cell numbers (n) in each cross section (20µm) were used to estimate the total number (N) of hNSC seeded in each scaffold (N = n x scaffold length / 20µm). The cell nucleus counting follows the principle of conservative counting, by which only the clearly distinguishable nuclei were counted. Given the fact that some cells are washed off during the staining process, and some nuclei were not visible if they were behind others, the total N estimates derived from this counting method represent a somewhat deflated version of the true cell numbers.

Results

Implants

The implant was designed as a porous PLGA scaffold to support seeded hNSC and permit in-growth of endogenous cells *in vivo,* as well as facilitating nutrient and waste transport. The pores were approximately 300 microns in diameter (Figure 2). To facilitate cell seeding, cells were seeded on scaffold layers, 1 millimeter in thickness, which were subsequently sutured together with an outer layer to yield a three-dimensional hemi-cylindrical structure (Figure 3). The outer layer of the implant was designed to emulate the spinal cord dura, to inhibit infiltration of meningeal cells into the scaffold in case the dura was not completely resealed post-surgery. The outer layer consisted of a solid PLGA sheet, approximately 200 microns in thickness.

The seeding protocol lead to scaffolds with hNSC attached to the outer surface, as well as the inner walls of the pores inside the scaffolds (Figure 4). Based on 6 sections from 2 scaffolds, the average number of hNSC attached in each 20 µm scaffold section n=4922, which translates to approximately 2.5 million hNSC in a 10 mm x 5 mm x 1mm scaffold. Therefore, there were an estimated 5 million hNSC on assembled scaffolds.

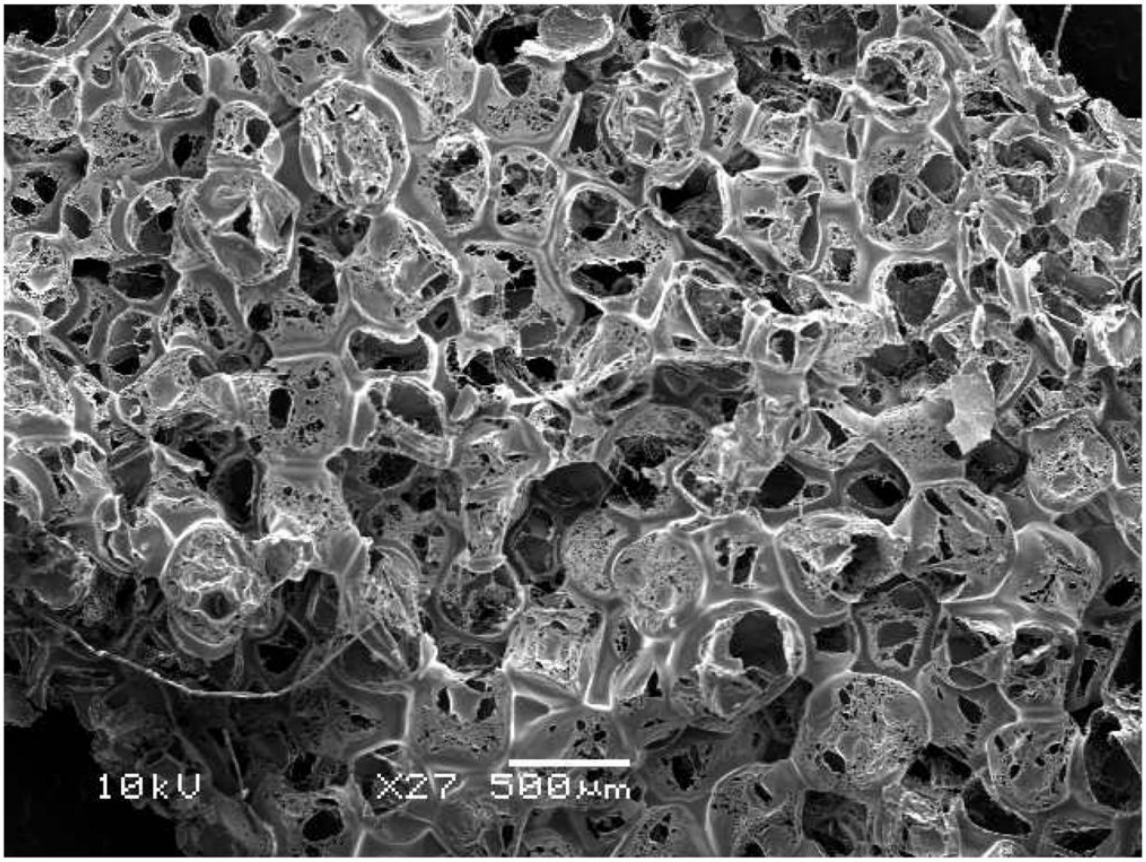

Figure 2. Scanning electron microscope image of scaffold architecture.

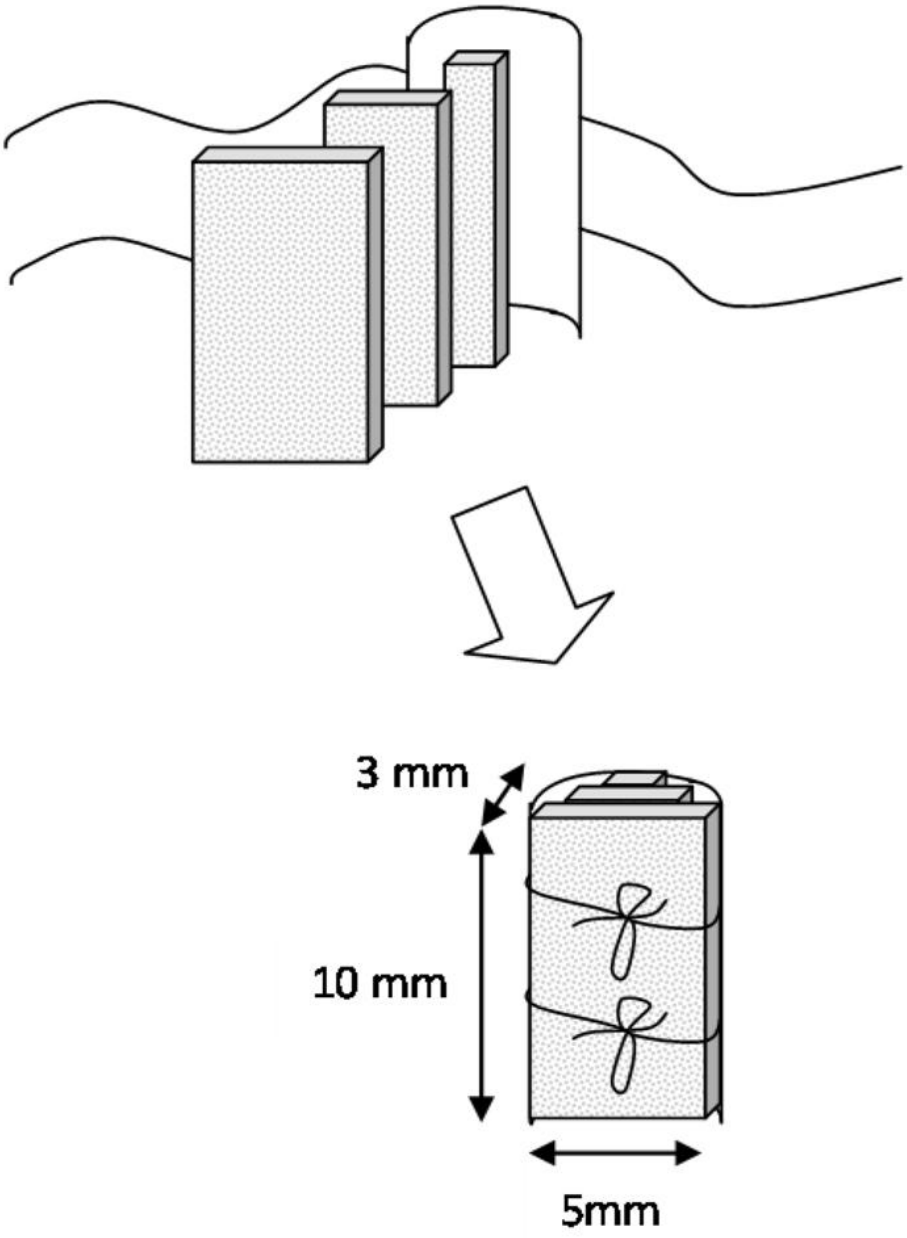

Figure 3. Composite scaffold design.

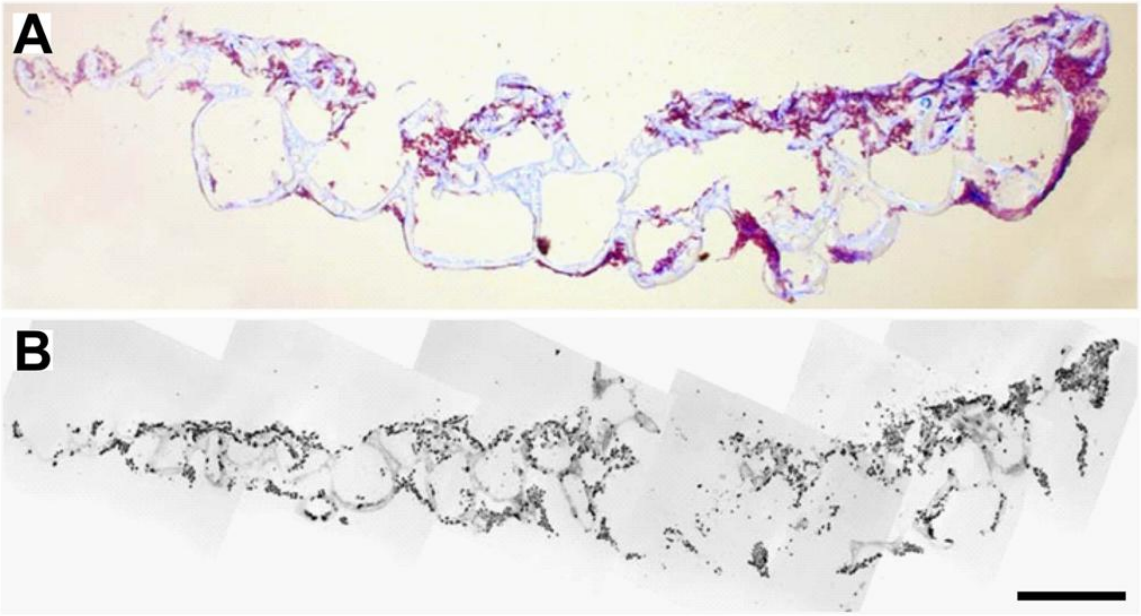

Figure 4. Seeding of hNSC on PLGA scaffolds. **A:** Microscope image of Toluidine Blue staining of a cross section of a PLGA scaffold seeded with hNSCs (purple dots). **B:** Montage of multiple microscope images of the different areas of the same scaffold cross section; inverted greyscale image of DAPI fluorescence (black dots are hNSC nuclei stained for DAPI). Scale bar = 500 microns.

Neuromotor outcomes

Monkeys were enrolled in the study according to the treatment schedule indicated in Table 2. The spinal cord hemisection procedure and placement of the scaffold or scaffold seeded with hNSC (scaffold+hNSC) was well tolerated in all subjects. Throughout the duration of the study the monkeys remained in good health. The T9-T10 hemisection resulted in Brown-Séquard syndrome with paralysis of the ispilateral leg, slight reduction in ipsilateral muscle tone in the lower abdomen, loss of pain sensation in the contralateral leg, and spastic paresis in the ipsilateral leg with increased knee and ankle jerk reflexes. There was a preservation of bladder and bowel tone, including in the acute setting, and no evidence of joint contractures in the paretic limb. Induced neuromotor deficits were observed in the immediate post-operative setting. One monkey (Y430) developed a sore on the dorsal surface of the ipsilateral (left) foot two weeks post-injury, as a result of loss of dorsiflexion. The wound improved with routine wound care. Video recordings of quadrupedal locomotion and object retrieval in the ambulation chamber permitted an assessment of gait and posture deficits and improvements over time. Application by a trained observer of the specified video scoring procedure (Table 1) to recorded video segments provided a reproducible measure of leg, foot and toe positioning and movements, postural changes and overall neuromotor changes. Changes in the video based neuromotor score were defined for the in the ipsilateral (left) and contralateral (right) side of each monkey (Figure 5).

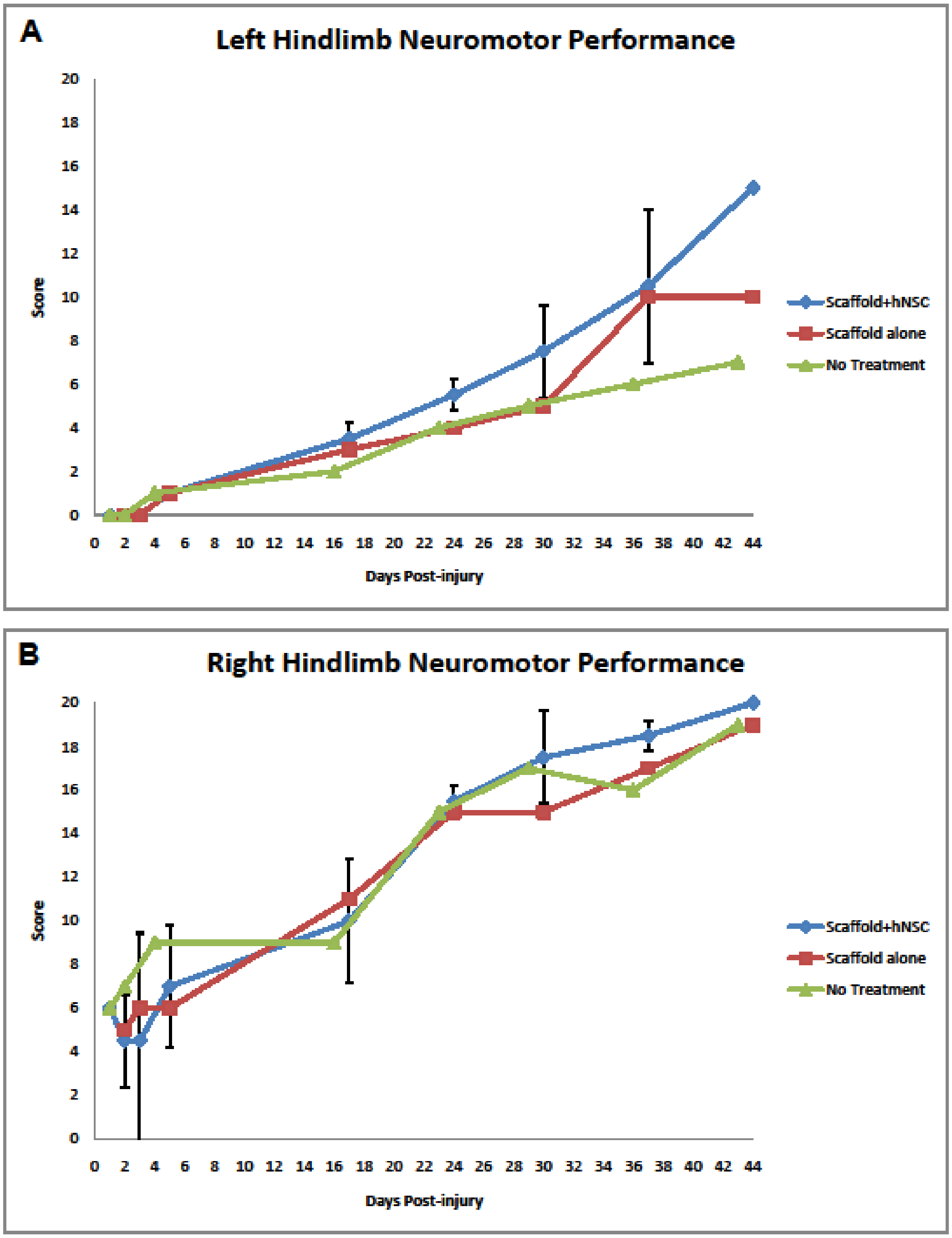

Figure 5. Temporal profile of functional recovery post-injury. **A:** Video neuromotor scores in ipsilateral (left) hindlimb. **B:**. Video neuromotor scores in contralateral (right) hindlimb. Designations are as follows: Scaffold+hNSC: mean and standard deviation for Y430 and X992; n=2 except for day 1 and day 44 where n=1 due to sacrifice of X992 at 40 days post-injury. Scaffold alone: Y464. Control (no treatment): Y156.

Histopathology and Immunohistochemistry

Hematoxylin and eosin (H&E) stained cross-sections in the thoracic region rostral and caudal to the injury center were examined, showing clear anatomic evidence for the observed Brown-Séquard syndrome in all subjects. In rostral sections, there was severe degeneration of ipsilateral dorsal funiculus afferent tracts, as confirmed by the presence of swollen axons, necrosis and lymphocyte and macrophage invasion. Severe ipsilateral degeneration of lateral and ventral corticospinal tract efferents was also observed. In caudal sections, there was bilateral preservation of dorsal funiculi afferents. The degree of lymphocyte recruitment to afferent and efferent tracts, rostral and caudal to the injury site respectively, varied between subjects.

H&E staining revealed small amounts persisting polymer debris in the scaffold+hNSC subject sacrificed at 40 days post-injury (Figure 6 A, B). There was minimal evidence of persisting polymer in the scaffold+hNSC sacrificed at 82 days post-injury, suggesting complete degradation and clearance of the scaffold within this time frame *in vivo* (Figure 6 C, D).

H&E staining revealed evidence of fibrous matter around the lesion in two subjects, namely the scaffold treated subject sacrificed at 83 days post-injury (Y464) and the scaffold+hNSC treated subject sacrificed at 82 days post-injury (Y430). This was observed as birefringence using a polarizing filter under an optical microscope, often an indication of collagen deposition. It is possible that, in these subjects, the resealed dura did not remain completely intact following surgery, permitting infiltration of fibroblasts into the injury site. As the influx of meningeal cells could play a significant role in the pathological profile of the lesion, the consistency of dural integrity is important across subjects in the development of a central nervous system injury model.

H&E staining also revealed lines of hemocynanin deposition, demarking severed blood vessels within the spinal cord. Blood flowing under pressure from severed blood vessels, in particular arterial vessels, is a possible source of mechanical insult to nervous system tissue surrounding the lesion. In addition, damaged blood vessels result in local ischemia. The presence of multinucleated giant cells around the lesion site was observed in all subjects, and it is unclear to what extent, if at all, these were specifically present in response to foreign polymer materials and allogeneic hNSC.

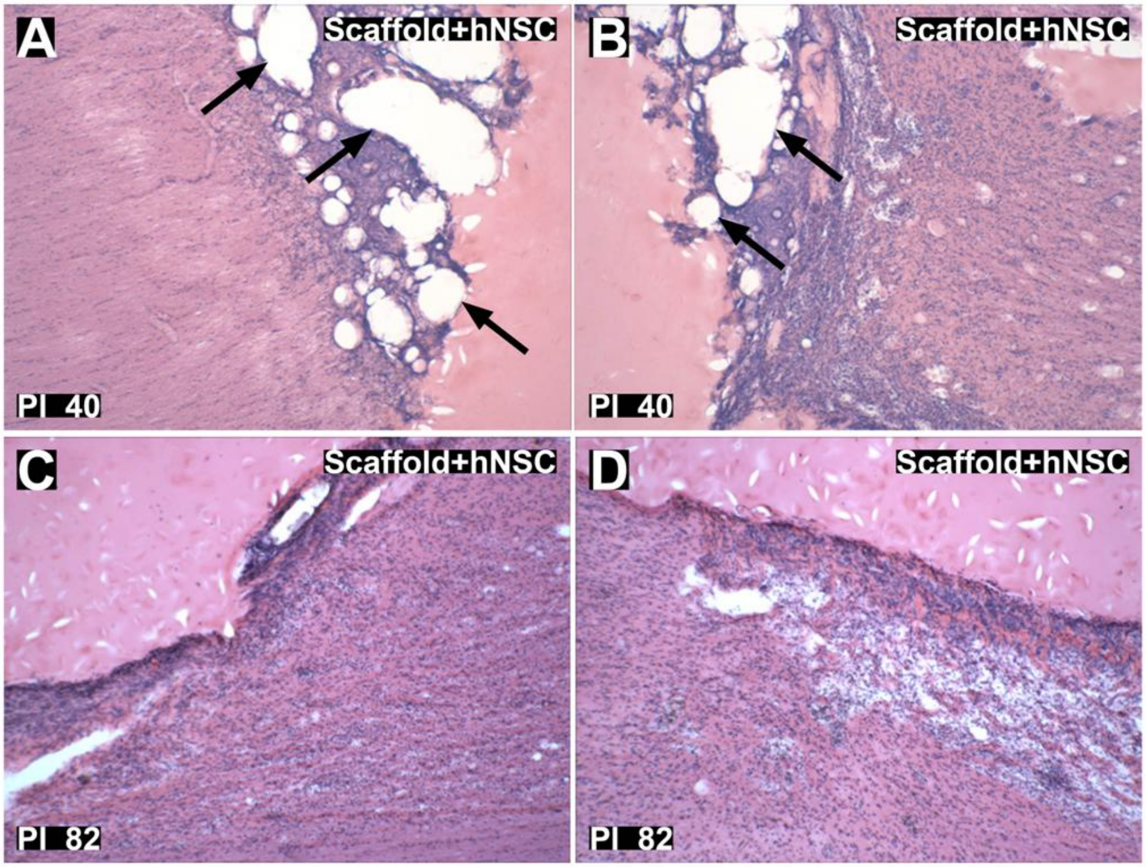

Figure 6. Hematoxylin and eosin staining of lesion margins. **A-B:** Rostral (**A**) and caudal (**B**) lesion margins of scaffold+hNSC treated animal 40 days post-injury (X992). Arrows indicate preserved polymer matrix. **C-D:** Rostral (**C**) and caudal (**D**) lesion margins of scaffold+hNSC treated animal 82 days post-injury (Y430). There was no appreciated polymer matrix, indicating substantial degradation and clearance of the scaffold within 82 days *in vivo*. Glial cell proliferation and mononuclear cell infiltration adjacent to the lesion margin is visible in both subjects (**A-D**). Magnification = 40x.

Silver degenerative staining of cross-sections rostral and caudal to the lesion provided an indication of the extent of axonal disruption. The lesions remained unilateral in the lateral regions, with severe degeneration of ipsilateral lateral corticospinal tract (CST) efferents (Figure 7). Some degree of variability between subjects exists at the midline in dorsal funiculus afferents (Figure 8 A, C, E, G). In all animals, longitudinal sections through the lesion site showed clear evidence that, at the time of analysis, the lesion had crossed the cord midline, resulting in loss of grey matter on the contralateral side (Figure 9), further studied by quantification of lesion dimensions (Table 3). Axonal damage was observed both ipsilaterally and contralaterally in ventral-medial tracts (Figure 10). The small sample size, however, was not intended to distinguish the degree to which these differences were due to variations in the surgical lesion and individual responses to trauma compared to secondary injury and wound healing processes that may hypothetically be influenced by implantation of scaffolds and hNSC (Teng et al., 2002).

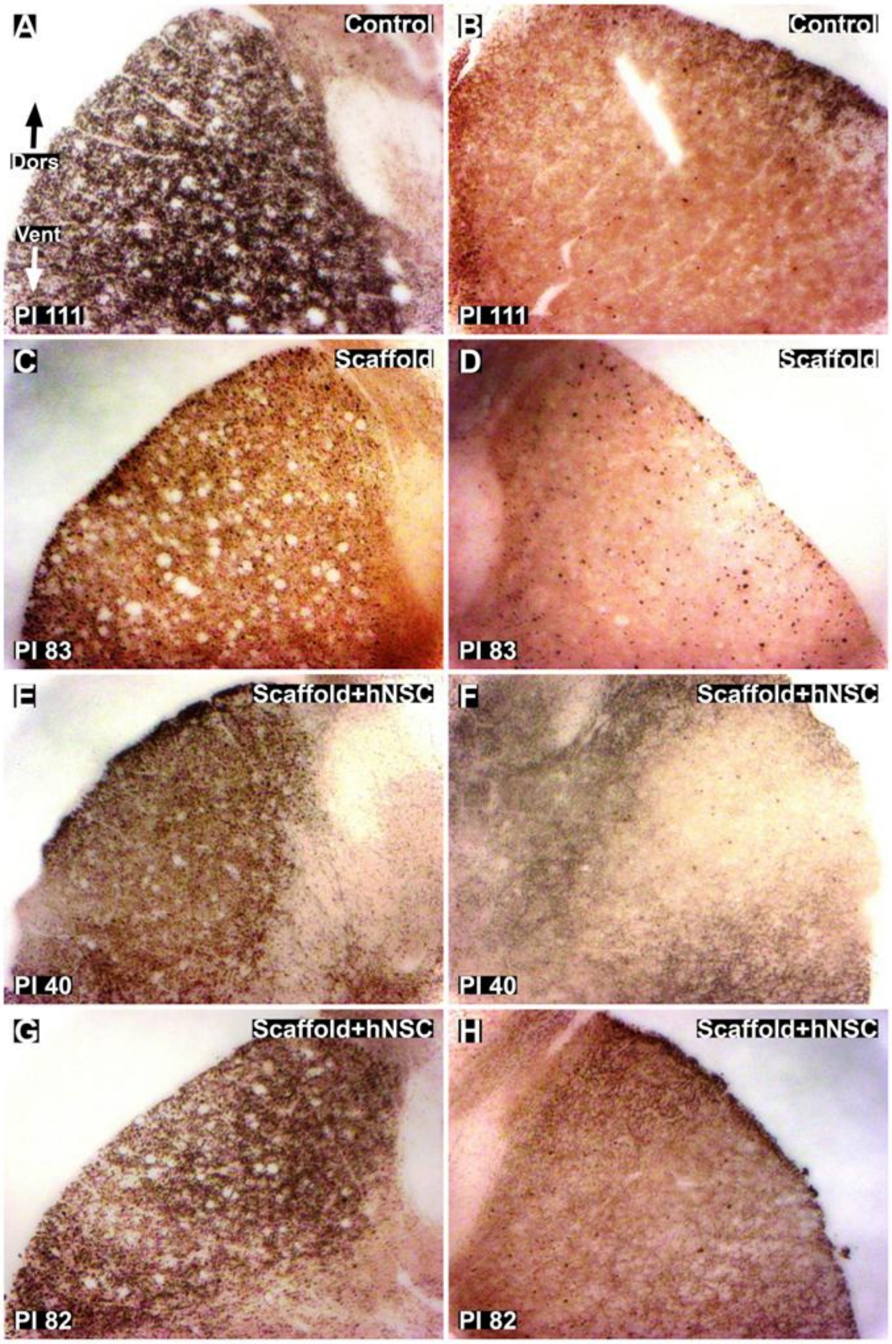

Figure 7. Silver staining for axonal degeneration of lateral corticospinal tracts (CST) in thoracic cross-sections caudal to the injury site. **A-B:** Ipsilateral (**A**) and contralateral (**B**) images of control subject 111 days post-injury. **C-D:** Ipsilateral (**C**) and contralateral (**D**) images of scaffold treated subject 83 days post-injury. **E-H:** Ipsilateral (**E, G**) and contralateral (**F, H**) images of scaffold+hNSC treated subjects 40 (**E, F**) and 82 (**G, H**) days post-injury. The lesion is unilateral with respect to degeneration of axons in the CST. Dors = dorsal. Vent = ventral. Magnification = 10x.

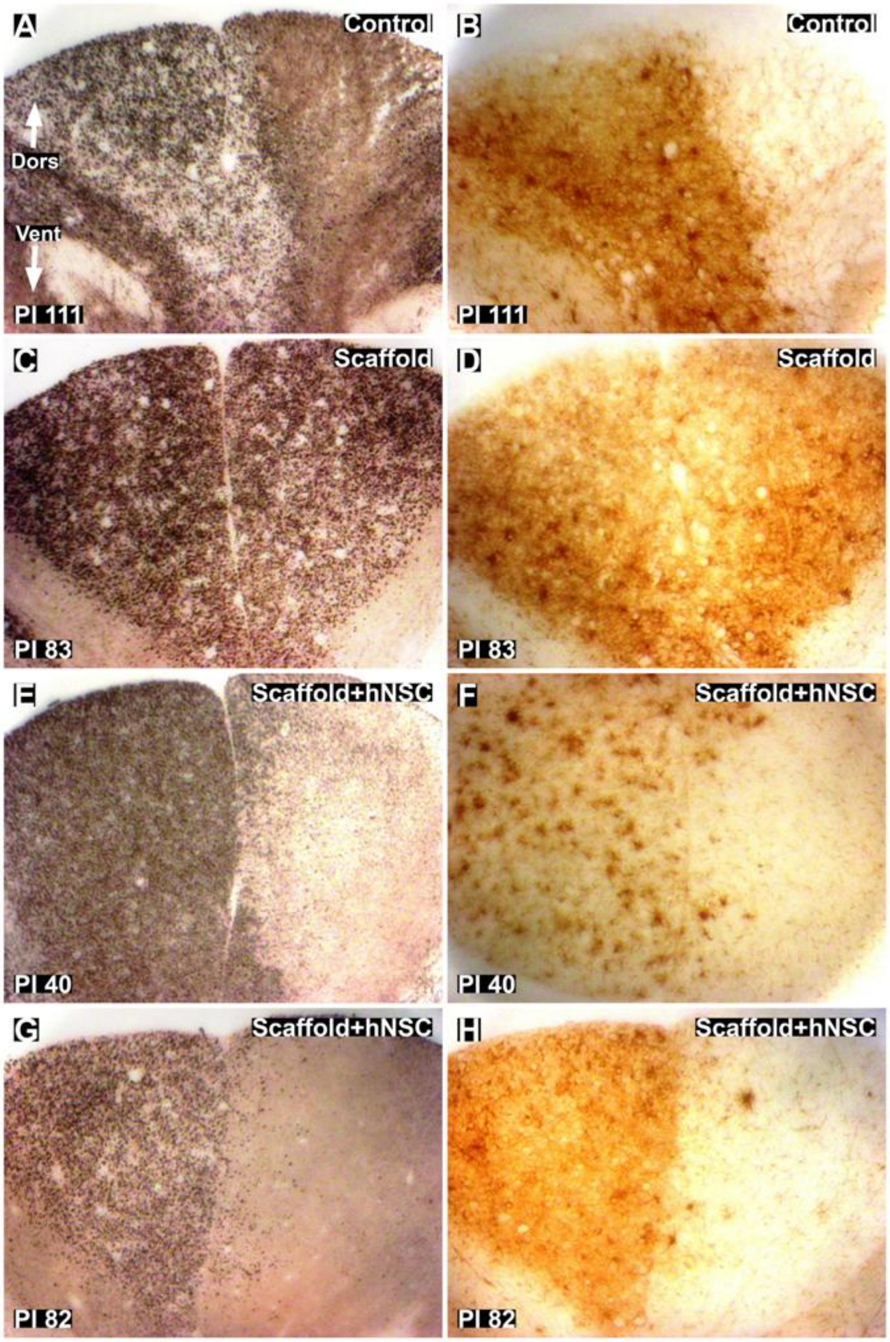

Figure 8. Silver staining and Iba1 staining of the dorsal funiculus in thoracic cross-sections rostral to the injury site. **A-B:** Silver (**A**) and Iba1 (**B**) staining of control subject 111 days post-injury. The lesion crosses the midline slightly in the control subject in the dorsal funiculus. **C-D:** Silver (**C**) and Iba1 (**D**) staining of scaffold treated subject 83 days post-injury. The images show total bilateral damage to the dorsal funiculus in the scaffold treated subject. **E-H:** Silver (**E, G**) and Iba1 (**F, H**) staining of scaffold+hNSC treated subjects 40 (**E, F**) and 82 (**G, H**) days post-injury. The lesion is predominately unilateral, with some axonal degeneration of contralateral dorsal funiculus afferents with spatially correlating microglial and macrophage activation. Dors = dorsal. Vent = ventral. Magnification = 10x.

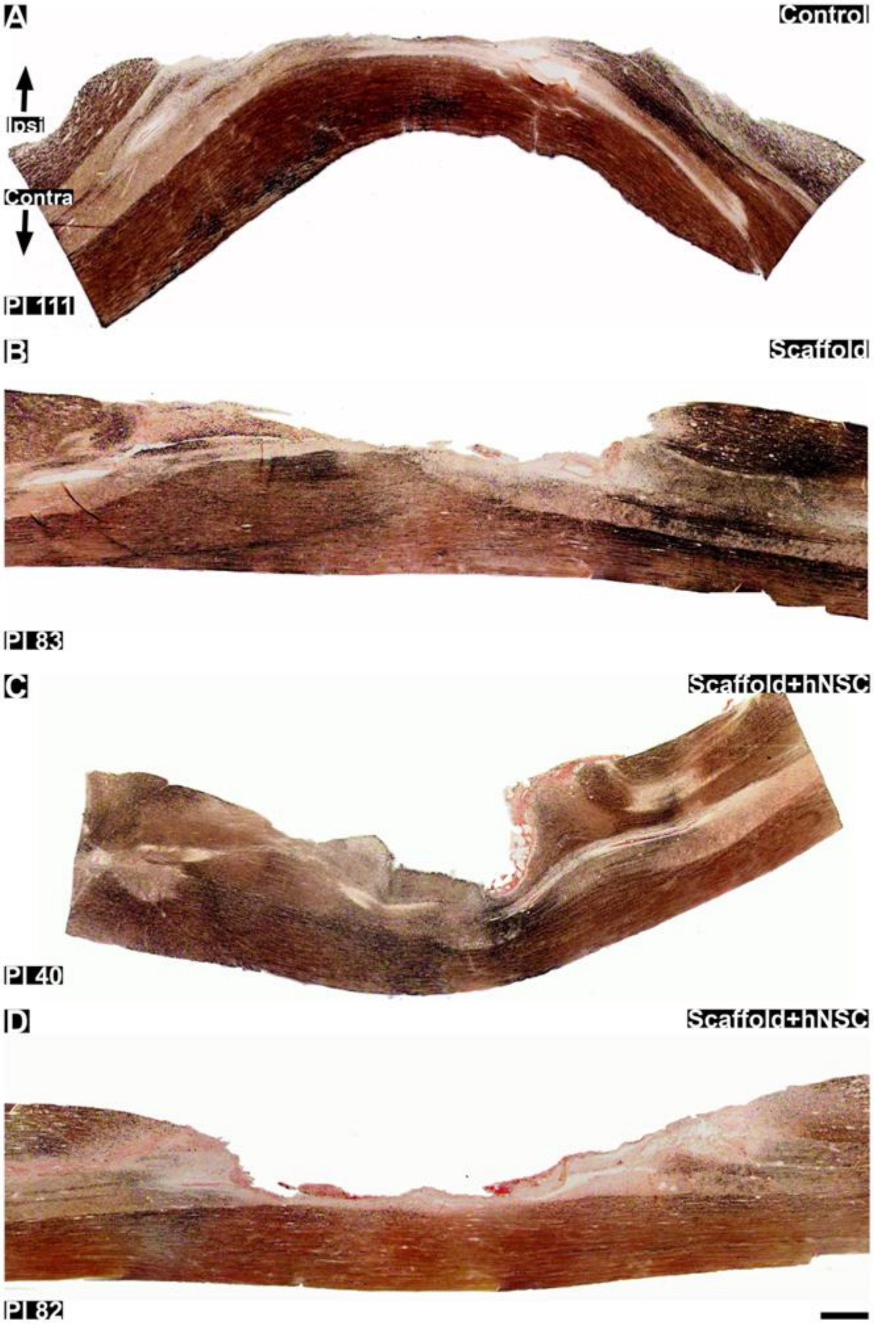

Figure 9. Silver staining for axonal degeneration of in thoracic sagittal sections through the hemisection lesions. Sections shown are closest to the middle of the cord in the rostral-caudal direction. **A:** Control subject 111 days post-injury. **B:** Scaffold treated subject 83 days post-injury. **C-D:** Scaffold+hNSC treated subjects 40 (**C**) and 82 (**D**) days post-injury. The lesion crosses the midline, in reference to the central canal where present, into the contralateral gray matter. In these sections the contralateral lateral funiculi appear to be preserved from the surgical lesion in all subjects. However, some degenerative staining is visible in contralateral efferents. Ipsi = ipsilateral lesioned side. Contra = contralateral unlesioned side. The cords are oriented rostral to caudal from left to right. Scale bar = 1 mm.

Table 3. Quantification of lesion dimensions. All cord widths were normalized to 0.60 cm. All units in cm unless otherwise noted.

Monkey	**Treatment group**	**Sacrifice day**	**Lesion area (cm^2)**	**Maximum lesion width**
X992	Scaffold+hNSC	40	0.24	0.36
Y430	Scaffold+hNSC	82	0.26	0.28
Y464	Scaffold alone	83	0.26	0.24
Y156	Control	111	0.31	0.29

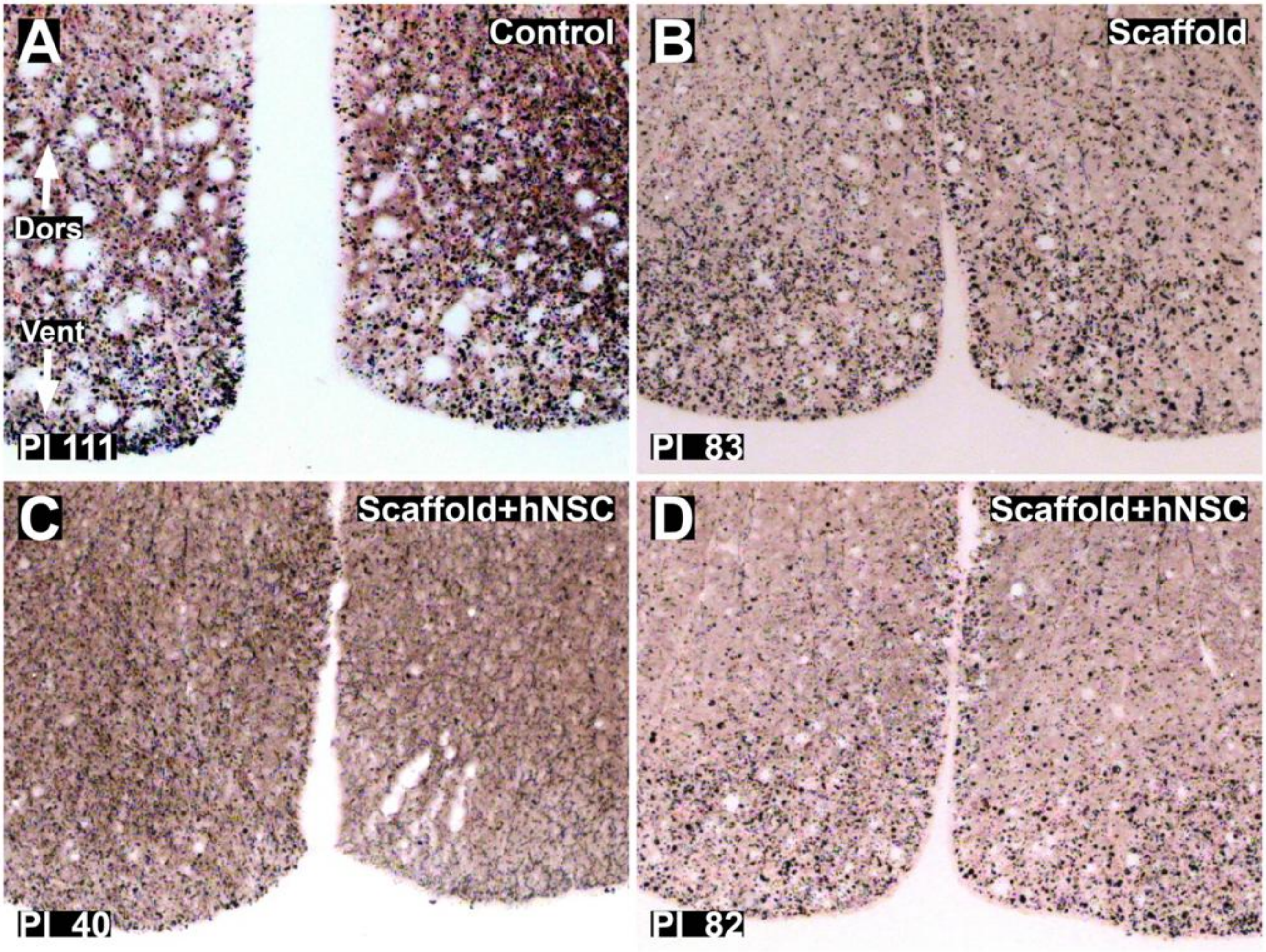

Figure 10. Silver staining for axonal degeneration of ventral funiculus tracts in thoracic cross-sections caudal to the injury site. **A:** Control subject 111 days post-injury. **B:** Scaffold treated subject 83 days post-injury. **C-D:** Scaffold+hNSC treated subjects 40 (**C**) and 82 (**D**) days post-injury. The lesion is bilateral with respect to degeneration of axons in the ventral-medial tracts. Dors = dorsal. Vent = ventral. Magnification = 10x.

Iba1 immunohistochemistry provided an indication of reactive microglial and macrophage abundance and distribution, providing a further measure of the degree to which the impact of the hemisection remained unilateral weeks post-injury. The lesions remained unilateral in the lateral regions, with substantial Iba1 immunoreactivity around ipsilateral lateral CST efferents (Figure 11). A similar degree of variability as observed by silver staining was observed using Iba1 immunohistochemistry in the dorsal funiculus rostral to the injury site (Figure 8 B, D, F, H).

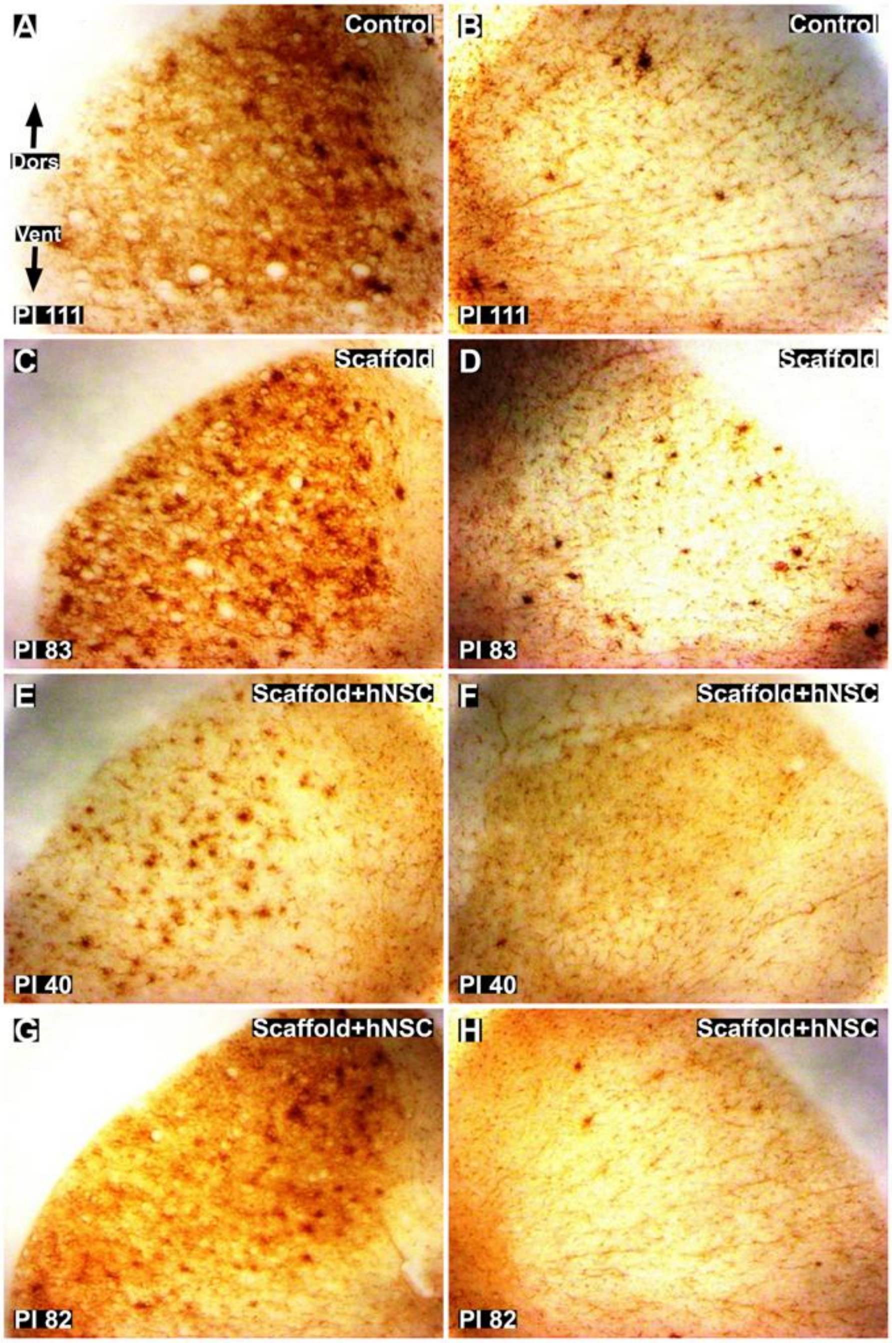

Figure 11. Iba1 staining for microglial and macrophage activation around lateral corticospinal tracts (CST) in thoracic cross-sections caudal to the injury site. **A-B:** Ipsilateral (**A**) and contralateral (**B**) images of control subject 111 days post-injury. **C-D:** Ipsilateral (**C**) and contralateral (**D**) images of scaffold treated subject 83 days post-injury. **E-H:** Ipsilateral (**E, G**) and contralateral (**F, H**) images of scaffold+hNSC treated subjects 40 (**E, F**) and 82 (**G, H**) days post-injury. The lesion is unilateral with respect to microglial and macrophage activation in the cord around the CST. Dors = dorsal. Vent = ventral. Magnification = 10x.

Discussion

Creation of a hemisection in the thoracic spine at the T9-T10 level in the African green monkey resulted in paralysis of the ipsilateral hindlimb, with concomitant sparing of bladder and rectal function and retention of sufficient overall motor function and mobility to allowed the continuation of feeding, grooming and other healthy activities without supplementary veterinary care. Behavioral evaluations confirmed improvement in post-operative paralysis over time, but improvement was gradual with sufficient remaining deficit to allow definition of recovery rate and distinction within subjects between phases of recovery and between subjects exhibiting different degrees of impairment. As such, this African green model of SCI may represent a means by which the safety and efficacy of therapeutic SCI interventions in a clinically relevant species could be assessed humanely.

This study was primarily designed to evaluate the feasibility of implementing a lateral hemisection model of SCI in a non-human primate, and to identify the specific clinically relevant behavioral and pathological endpoints that could be reproducibly obtained. Coupled kinematic and electromyographic measures in previous primate studies have demonstrated the feasibility of obtaining these critical endpoints (Courtine et al., 2005). The associated telemetry and surgical interventions, however, are, in themselves, a significant research investment and variable impacting animal wellbeing, with the established need for prolonged postoperative care. The more critical question addressed in this study was the consequence and tolerance of a T9-10 hemisection lesion, and a characterization of the overall neuromotor phenotype and its evolution over time such that more definitive efficacy and mechanism studies could be rationally and humanely designed. Therefore, the sizes of the treatment groups in the present study were limited and not designed to provide statistical evaluation of the therapeutic efficacy of the implanted PLGA scaffold PLGA scaffold seeded with hNSC at the lesion site. All subjects exhibited a return toward baseline neuromotor scores in the ipsilateral hindlimb, which exhibited complete post-operative paralysis following the T9-T10 lesion. This indicates a degree of recovery and neural plasticity consistent with reported findings in other primate SCI models (Edgerton et al., 2004). This observation encourages additional application of the model for more definitive preclinical studies in a larger study cohort to evaluate the therapeutic efficacy of PLGA scaffolds and human neural stem cells in the promotion of SCI recovery and repair.

Video capture of neuromotor behavior in the ambulation chamber provided a means of documenting and scoring neuromotor deficits and improvement over time. An observation based scoring system, however, may be inadequate to give precise information of neuromotor performance, due to the potential for the contralateral side to compensate for any loss of weight bearing ability and posture resulting from a unilateral interruption of motor and sensory pathways to the injured hindlimb. The application of kinematics, electromyography and evoked potentials would contribute to improved measures of neurologic function and quantification of ipsilateral and contralateral deficit and recovery (Courtine et al., 2009).

Histological analysis confirmed creation of a thoracic lesion in all study monkeys. Hematoxylin and eosin staining provided a definition of the extent of the lesion and degree of injury associated lymphocyte invasion, axonal swelling and macrophage infiltration, as well as a circumscribed degree of hemorrhage and gross necrosis. Silver staining revealed clear degenerative changes consistent with interruption of ipsilateral efferent lateral corticospinal tracts at the thoracic level caudal to the lesion and sensory afferents rostral to the lesion. It was noted that the ventral-medial region of the cord, which contains both important sensory and motor tracts, may be particularly sensitive to different degrees of bilateral surgical injury among subjects. Iba1 immunohistochemistry, exhibited a distribution that paralleled the degenerative findings highlighted by the silver staining. As such, Iba1 constituted an additional measure of the degree of injury and repair.

Histological evaluations confirmed the creation of a lesion with severe degeneration of ipsilateral motor and sensory axons. In no animals were the degenerative changes entirely unilateral. While contralateral corticospinal tracts were extensively preserved in all subjects, in addition to the majority of the dorsal horn in most subjects, contralateral damage was observed in the ventral-medial region in all subjects. Contralateral damage is most due to surgical variability, which will be improved in future, more sophisticated, investigations.

The persistence of the PLGA scaffold for at least 40 days, and degradation and clearance from the spinal cord within 82 days post-implantation was observed. Two important changes were made to the neural stem cells seeded PLGA scaffold used in this study, in comparison with a similar rodent study (Teng et al., 2002). Firstly, human neural stem cells (hNSC) were used instead of murine neural stem cells. Secondly, the PLGA scaffold was redesigned in response to observations made in the rodent study (Teng et al., 2002). The relative volume of the inner scaffold was increased to accommodate more hNSC. It was postulated that a major mechanism of action of the implanted cells may be due to trophic support rather than neuronal replacement. Therefore, it was hypothesized that a larger number of hNSC could increase any therapeutic effect. It was also proposed that the 'outer scaffold' in the rodent study, consisting of longitudinally oriented channels intended to permit axon in-growth, may have also served to prevent meningeal inflammatory cell infiltration. Unpublished *in vitro* data showed that the channels were impermeable to fibroblasts. To maximize the size of the inner scaffold, while providing a physical barrier to meningeal cell infiltration, the outer scaffold was constructed as a

200 micron thin, flexible sheet of PLGA. The observed tolerance of the current implant will guide implant design for further studies.

The ability to model spinal cord injury by lateral, segmental hemisection in African Green monkeys with limited impact on overall well-being presents a useful model for the assessment of spinal cord injury repair and response to intervention. Greater sensitivity and specificity to treatment effects could be achieved through expanded samples sizes to address lesion variability and application of coupled kinematic and electromyographic analyses, as well as further histological markers to identify specific mechanisms involved in secondary injury, repair and regeneration.

Acknowledgements

Human neural stem cells generated and provided by Evan Y. Snyder (Burnham Institute for Medical Research, La Jolla, CA, esnyder@burnham.org). We thank William L. Neeley for assistance with PLGA scaffold fabrication (MIT, Cambridge, MA), Darcy Benedict for assistance with cell culture and seeding (Brigham and Women's Hospital, Boston, MA) and Dr. D. Eugene Redmond Jr. for assistance with surgical procedures and animal care (St. Kitts Biomedical Research Facility, St. Kitts and Nevis). We thank Robert C. Switzer III for assistance with staining protocols (NeuroScience Associates, Knoxville, TN). We thank George Calapai for video editing, Lauren Mitarotondo for writing assistance and Janice Ye for image analysis (InVivo Therapeutics, Cambridge, MA). C.D.P. was supported by the MIT/CIMIT Medical Engineering Fellowship. InVivo Therapeutics thanks its investors and advisors for support. This study was funded by InVivo Therapeutics Corporation.

References

1. Babu RS, Muthusamy R, Namasivayam A. Behavioural assessment of functional recovery after spinal cord hemisection in the bonnet monkey. Journal of Neurological Sciences. 2000;178:136-52.
2. Baptiste DC and Fehlings MG. Update on the treatment of spinal cord injury. Progress in Brain Research. 2007;161:217-33.
3. Basso DM, Beattie MS, Bresnahan JC. Graded histological and locomotor outcomes after spinal cord contusion using the NYU weight-drop device versus transaction. Experimental Neurology. 1996;139:244-56.
4. Brown-Séquard C É. De la transmission croisée des impressions sensitives par la moelle épinière. Comptes rendus de la Société de biologie. 1851;2:33-44.
5. Courtine G, Roy RR, Hodgson J, McKay H, Raven J, Zhong H, Yang H, Tuszynski MH, Edgerton VR. Kinematic and EMG determinants in quadrupedal locomotion of non-human primate (rhesus). J Neurophysiol. 2005;93:3127-45.
6. Courtine G, Bartlett Bunge M, Fawcett JW, et al. Can experiments in nonhuman primates expedite the translation of treatments for spinal cord injury in humans? Nat. Med. 2007;13(5):561-6.
7. Courtine G, Gerasimenko Y, van den Brand R, Yew A, Musienko P, Zhong H, Song B, Ao Y, Ichiyama RM, Lavrov I, Roy RR, Sofroniew MV, Edgerton VR. Transformation of nonfunctional spinal circuits into functional states after the loss of brain input. Nature Neuroscience. 2009;12:1333-42.
8. Crowe MJ, Bresnahan JC, Shuman SL, Masters JN, Beattie MS. Apoptosis and delayed degeneration after spinal cord injury in rats and monkeys. Nature Medicine. 1997;3(1):73-6.
9. De Olmos, JS et al. . Neutrotox and Teratol. 1994. 16: 545-61.
10. Edgerton VR, Tillakaratne NJK, Bigbee AJ, de Leon RD, Roy RR. Plasticity of the spinal neural circuitry after injury. Annu. Rev. Neurosci. 2004;27:145-67.
11. Feringa ER, Johnson RD, Wendt JS. Spinal cord regeneration in rats after immunosuppressive treatment. Theoretic considerations and histologic results. Archives of Neurology. 1975;32(10):676-83.
12. Flax JD, Aurora S, Yang C, et al. Engraftable human neural stem cells respond to developmental cues, replace neurons, and express foreign genes. Nat. Biotech. 1998;16:1033-9.
13. Hall ED, Springer JE. Neuroprotection and acute spinal cord injury: a reappraisal. NeuroRx. 2004;1:80-100.
14. Jones TB, McDaniel EE, Popovich PG. Inflammatory-mediated injury and repair in the traumatically injured spinal cord. Current Pharmaceutical Design. 2005;11:1223-36.
15. Lavik E, Teng YD, Snyder E, Langer R. Seeding neural stem cells on scaffolds of PGA, PLA, and their copolymers. Methods Mol Biol. 2002;198:89-97.

16. Liverman CT, Altevogt BM et al. Spinal Cord Injury: Progress, promises and priorities. 2005. National Academies Press, Washington, D.C.

17. Mikos AG, Sarakinos G, Leite SM, Vacanti JP, Langer R. Laminated three-dimensional biodegradable foams for use in tissue engineering. *Biomat.* 1992;14(5):323-30.

18. Park KI, Teng YD, Snyder EY. The injured brain interacts reciprocally with neural stem cells supported by scaffolds to reconstitute lost tissue. Nat. Biotech. 2002;20:1111-7.

19. Rossignol S, Schwab M, Schwartz M, Fehlings MG. Spinal cord injury: time to move? The Journal of Neuroscience. 2007;27(44):11782-92.

20. Sung HJ, Meredith C, Johnson C, Galis ZS. The effect of scaffold degradation rate on three-dimensional cell growth and angiogenesis. Biomaterials. 2004;25:5735-42.

21. Teng YD, Lavik EB, Qu X, Park KI, Ourednik J, Zurakowski D, Langer R, Snyder EY. Functional recovery following traumatic spinal cord injury mediated by a unique polymer scaffold seeded with neural stem cells. Proc Natl Acad Sci U S A. 2002;99(5):3024-3029.

22. Thuret S, Moon LDF, Gage FH. Therapeutic interventions after spinal cord injury. Nature Neuroscience. 2006;7:628-43.

23. Yu D, Neeley WL, Prichard CD, Slotkin JR, Woodard EJ, Langer R, Teng YT. Blockade of peroxynitrite-induced neural stem cell death in the acutely injured spinal cord by drug-releasing polymer. Stem Cells. 2009;27:1212-22.

III.

Evaluation of an implanted biodegradable polymeric scaffold in a model spinal cord injury in the Rhesus Macaque non-human primate

Christopher D. Pritchard (1), Jonathan R. Slotkin (2), Larry S. Sherman (3),
Francis M. Reynolds (4), Eric J. Woodard (5), Robert Langer (1)

(1) Department of Chemical Engineering
Massachusetts Institute of Technology, Cambridge, MA 02139, USA

(2) Department of Neurosurgery
The Washington Brain and Spine Institute, Washington, DC 20010, USA

(3) Division of Neuroscience
Oregon National Primate Research Center, Beaverton, OR 97006, USA

(4) InVivo Therapeutics Corporation
Cambridge, MA 02141, USA

(5) Department of Neurosurgery
New England Baptist Hospital, Cambridge, MA 02120, USA

Abstract

A porous poly(lactide-co-glycolide)-co-poly(L-lysine) (PLGA-PLL) scaffold was implanted into a non-human primate model (Rhesus Macaque) of experimental acute spinal cord injury (SCI) to assess of safety and efficacy of the medical device. A thoracic lateral hemisection was performed on three subjects followed by histological analysis 12 weeks post-injury. One subject received a customized PLGA-PLL scaffold immediately after surgical spinal cord resection. No adverse events were observed as a result of the biomaterial implants. In addition, a reduction in scarring around the lesion was observed in the primate treated with the scaffold. This result provides a promising preliminary indication of the effect of the scaffold in reducing the degree of secondary injury, measured as astrogliosis, in a model surgical hemisection SCI.

Materials and methods

Synthesis of poly(lactide-co-glycolide)-co-poly(L-lysine)

Poly(lactide-co-glycolide)-co-poly(L-lysine) (PLGA-PLL) was synthesized according to previously published methods (Fig. 1) [1]. Briefly, poly(D,L-lactic-co-glycolic acid) (RG502H, 50:50 ratio; Resomer 502 H, Mn ~ 12,500; Boeringer Ingelheim KG) and poly(ε-carbobenzoxy-L-lysine) (PLL, MW 6300 by LALLS; Sigma) were stored in a desiccator at --20 °C until use. Dimethylaminopyridine (DMAP) and dicyclohexyl carbodiimide (DCC), anhydrous dimethlyformamide (DMF), and hydrogen bromide, 30 wt% in acetic acid, (HBr/HOAc), were from Aldrich and used as received. RG502H and PLL were loaded into a flask in dissolved in DMF under Argon. Two molar equivalents (with respect to the estimated number of carboxylic acid groups present in the PLGA based on molecular weight) of DCC and 0.1 molar equivalents of DMAP were loaded into a separate flask and dissolved under argon. The DCC solution was then added to the polymer solution and the reaction was allowed to run for 48 h under argon at 0 °C in an ice bath. The solution was diluted by the addition of chloroform and filtered to remove the DCU, an insoluble product of the reaction. The polymer product was precipitated in methanol, isolated by vacuum filtration, washed three times in ether, and dried under vacuum for at least 48 h. For deprotection, approximately 1.5 g of the protected polymer was placed in a 100 mL round bottomed flask and purged under argon for 15 min. 10 mL of HBr/HOAc was added via syringe to the polymer under argon to form a slurry and was allowed to stir for 90 min. The polymer was precipitated with ether, separated by vacuum filtration, and washed several times with ether until the polymer took on an off-white color and went from being a sticky mass to a crumbly powder. The product was then redissolved in chloroform, precipitated in ether, separated by vacuum filtration, and dried under vacuum for at least 48 h.

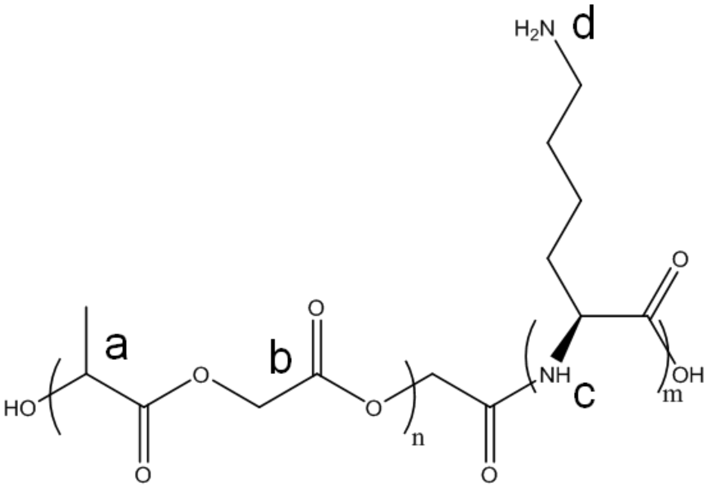

Figure 1. Poly(lactide-co-glycolide)-co-poly(L-lysine). The poly(lactide-co-glycolide) is depicted here as an alternating block copolymer showing only one monomer of lactic acid and glycolic acid for illustrative simplification. Characteristing groups are labeled: **a.** methyl in lactic acid monomer. **b.** ester in glycolic acid monomer. **c.** amide in poly(L-lysine). **d.** primary amine on lysine residue side chain.

Characterization of poly(lactide-co-glycolide)-co-poly(L-lysine)

The lysine content in the resulting PLGA-PLL was assessed by amino acid analysis (AAA Laboratory, Mercer Island, WA). A sample was hydrolyzed for 20 hours in 6N hydrochloric acid (HCl) with 0.05% mercaptoethanol and 0.02% phenol at 115 ºC and analyzed by liquid chromatography. Fourier transform infrared (FT-IR) spectroscopy was taken using an Alpha FT-IR with Eco ATR sampling module (Bruker Optics, Billerica MA). FT-IR spectra were obtained on the dried powder by measuring attenuated total reflection.

Scaffold fabrication

Porous polymer scaffolds were prepared in a similar manner to a previously published protocol [2]. Poly(lactide-*co*-glycolide) (PLGA) with a lactide/glycolide ratio of 50:50 and intrinsic viscosity 0.55-0.75 dl/g was obtained from Lactel (Durect Corp., Pelham, AL). Polymer scaffolds were fabricated by solvent casting/particulate leaching. A blend of PLGA and synthesized PLGA-PLL (1:1) was dissolved in chloroform (Sigma, St. Louis, MO) to obtain a 5 wt % stock solution. The stock solution was mixed with sodium chloride (particle size 180-450 µm by sieving; Sigma) in a 1:1.67 ratio (3 mL / 5 g) and poured into an elliptical aluminum mold with dimensions 5 x 3 x 20 mm. After chloroform was evaporated in a fume hood and rotovap (Büchl, Germany) for 48 hours, the salt particles were leached out by immersion in distilled water for 48 h at room temperature. The water was changed every 4-8 h during the leaching period. Subsequently, the scaffolds were dried on blotting paper and lyophilized overnight to remove residual water. The process yielded a highly porous scaffold with dimensions matching the spinal cord of the African green monkey. The scaffolds were stored in Eppendorf tubes

(Daigger) and Tyvek™ packaging (3 tubes per package) in a secondary container with desiccant (Drierite) at -20 ºC until use.

Scanning electron microscopy

Lyophilized scaffolds were air dried for 24 hours, mounted on aluminum stubs and sputter coated with gold, and imaged using a JEOL 6400 Scanning Electron Microscope with Orion image processing (JEOL, Tokyo, Japan).

Scaffold testing with neuroblastoma cells

Adhesion of neuronal cells on the scaffolds was assessed using neuronal cells (N18RE105 cell line). This cell line is a somatic cell hybrid from the fusion of dissociated embryonic rat neural retina cells with the neuroblastoma cell line N18-TG2. Cells (approx. 300,000) were cultured in T75 flasks (Corning, Midland, MI) an incubator at 37ºC with 5% CO_2 in 15 mL Dulbecco's Modified Eagle Medium (DMEM, Gibco #430-2100) with 4500 mg / L D-glucose and L-glutamine. Medium was replaced twice weekly. Cells were split once a week using a phosphate buffered saline wash (PBS, 10 mL, Invitrogen) followed by trypsin (5 mL, Gibco, 5 minutes at room temperature), addition of 10 mL DMEM, centrifugation at 1000 r.p.m. (5 minutes) and resuspension (10 mL).

Electron beam sterilization validation and procedure

Sterilization testing was conducted using spore strips (Bacillus pumilus, 10^6 per strip, STP-06, NAMSA, Northwood, OH) in closed Eppendorf™ tubes and packaging (Tyvek™) (one wrapped spore per tube, one tube per package. Sterilization was performed by electron beam sterilization (Electron Technologies Corp., South Windsor, CT) at 3, 5 and 10 mRad. Sterilized spore strips and an unsterilized control were removed from tubes and cultured in soybean casein digest broth in test tubes overnight at 35 ºC under vigorous shaking. Optical density was measured at a wavelength of 600 nm in a cuvette with a pathlength of 1 cm on a Spectramax Plus spectrophotometer (Molecular Devices). Scaffolds were sterilized in closed Eppendorf™ tubes and packaging (Tyvek™) in (one scaffold per tube, 3 tubes per package) by electron beam sterilization (Electron Technologies Corp., South Windsor, CT) at 3 mRad.

Scaffold hydration

Prior to seeding or implantation scaffolds were placed in 0.2 μm filtered ethanol (2 mL) for 5 minutes in a sterile polystyrene 6-well culture plate (Corning) in a laminar flow hood, followed by rinsing in PBS (3 x 2 mL). Scaffolds were transferred to the operating room with minimal excess PBS inside sterile polystyrene test tubes (VWR).

Animal selection and protocol approval

3 female rhesus macaques that had been previously ovariectomized were selected based on normal health examinations by Oregon National Primate Research Center (ONPRC) Division of Animal Resources (DAR) veterinary staff and following hematological and blood chemistry analyses. The Oregon Health & Science University (OHSU) Institutional Animal Care and Use Committee gave permission to conduct the overall study (protocol #0840) on January 2, 2009 in accordance with federal and state laws regarding the use of animals in biomedical research. Approval was granted based on a pilot study performed using African Green Monkeys demonstrating minimal post-surgical animal care. Permission to utilize these animals for a second major surgical procedure (spinal cord hemisection; animals had already been

ovariectomized) was granted by the USDA on January 20, 2009. Animals were housed in standard caging, lined with soft toweling following spinal cord hemisection surgeries.

Spinal cord hemisection surgeries

T10 hemisections were performed as indicated (Table 1) as described previously [3]. The scaffolds was implanted in #21948 within five minutes of hemisection. The length of hemisection was measured using a sterile plastic 15 mm ruler, and the scaffold was customized using a surgical blade. All animals were awake and moving in their cages within a few hours post- surgery and were monitored closely by surgical and veterinary staff during the recovery period. Cases #21948 and #24841 experienced urinary retention. These subjects were catheterized and shown to be carrying urine volumes of approximately 150 ml. In these subjects, the bladder was flaccid and could not be expressed manually. This is consistent with a neurological insult resulting in loss of reflexive bladder control, and catheterization was performed on a regular basis. Reflexive bladder control was fully regained within 72 hours post-surgery.

Table 1. Animal assignments.

Animal#	**Age (years)**	**EMG**	**Surgery date**	**Treatment**
21948	9	OK	2/27/09	Scaffold
24841	9	OK	2/28/09	Lesion only
22747	7	OK	2/28/09	Lesion only

Results

Scaffold characterization

The poly(lactide-co-glycolide)-co-poly(L-lysine) had a lysine content of 3.09 wt.% by amino acid analysis. Lysine presence was further confirmed by FT-IR spectroscopy (Fig. 2).

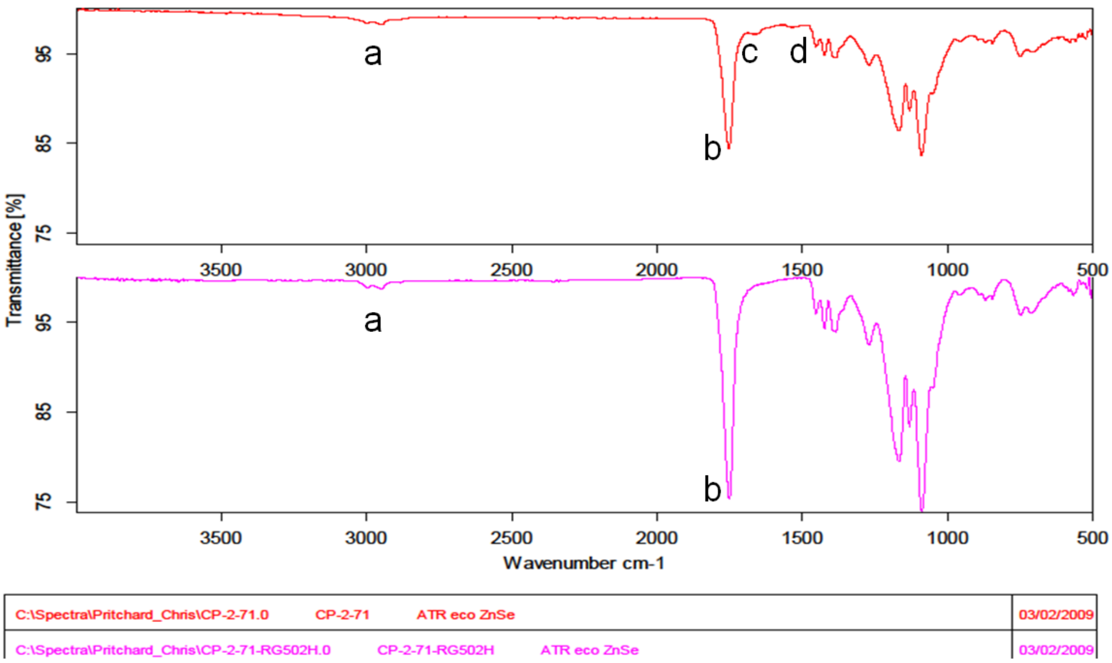

Figure 2. FTIR spectroscopy of PLGA-PLL. Components were identified by peaks at the following wavenumbers: **a.** methyl C-H stretch at 2870 cm^{-1} and 2960 cm^{-1}.**b.** ester C=O stretch at 1735 cm^{-1}. **c.** amide C=O stretch at 1650 cm^{-1}. **d.** primary amine stretch at 1560-1640 cm^{-1}.

Sterilization

Table 2 shows results of electron beam sterilization at increasing dosages. All three dosages were successful in sterilizing the spore strips. To minimize polymer degradation, a dosage of 3 mRad was selected for scaffold sterilization.

Table 2. Optical density measurements of soybean broth supernatant for spore strips sterilized at increasing radiation dosages, compared to an unsterilized spore strip control. Absorbance values were obtained at a wavelength of 600 nm and a 1 cm path length.

mRad	**OD600**
3	0.042
5	0.043
10	0.042
0 (control)	1.206

Scaffold characterization and intraoperative customization

The solvent casting / salt leaching procedure resulted in hemi elliptical scaffolds with a porous interconnected architecture on the order hundred of microns (Fig. 3 A). Once hydrated, the scaffold could be easily customized intraoperatively using a surgical blade (Fig. 3 B). Poly(L-lysine) is well known to promote cell adhesion to scaffolds and cell culture plates [4]. Combined with the porous scaffold architecture, this led to structure highly seeded with neuronal cells *in vitro* (Fig. 3 C, D).

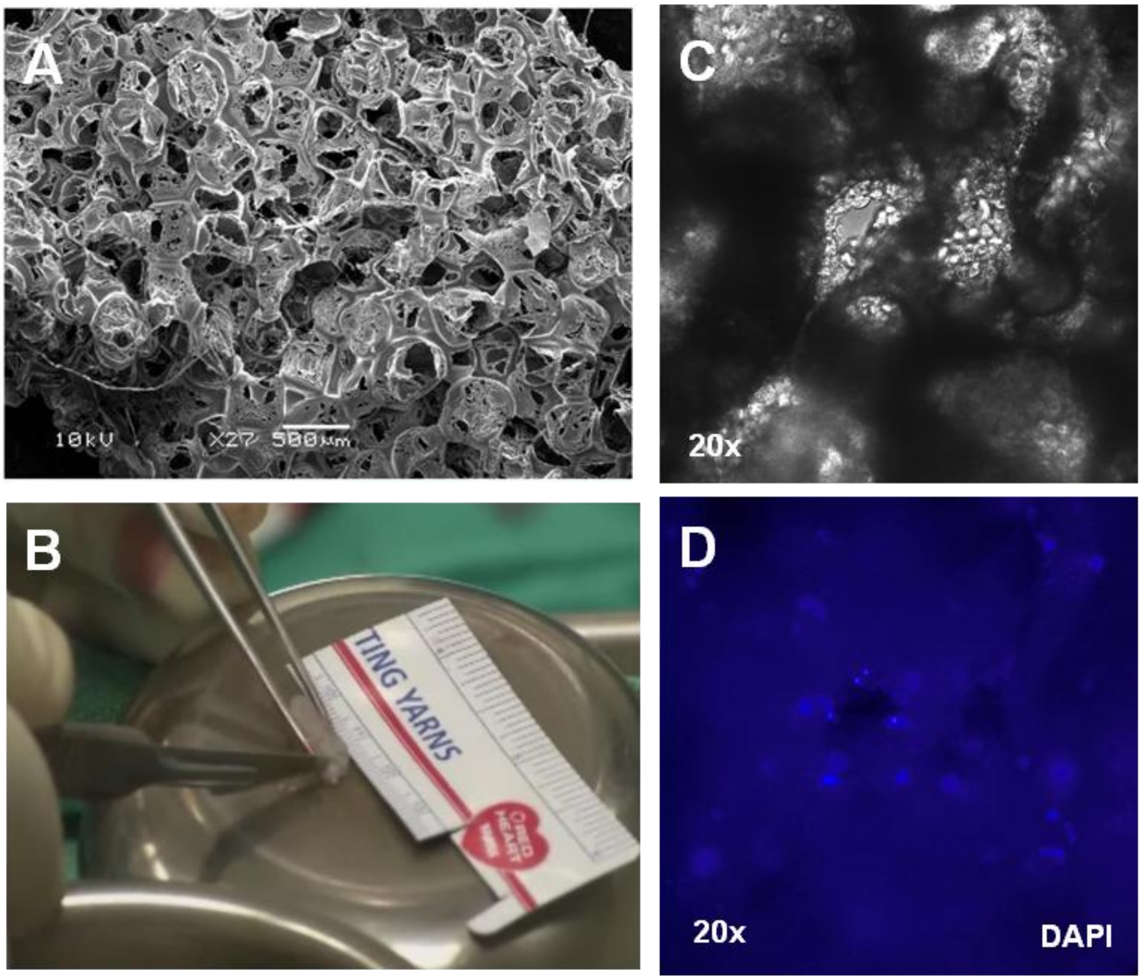

Figure 3. A. Scanning electron microscope image of scaffold. **B.** Intraoperative customization of scaffold. **C-D.** Light microscope (**C**) and DAPI (blue) fluorescence (**D**) image of neuroblastoma cells seeded on scaffold.

PLGA-PLL scaffold reduced astrogliosis following T10 lateral hemisection SCI

Glial scarring and astrogliosis were assessed by glial fibrillary acidic protein (GFAP) immunolabeling. Both control primates, numbered 24841 (Fig. 4 A, B) and 22747 (not shown), had extensive GFAP immunoreactivity both surrounding and distant from the lesion. The scaffold-treated primate,numbered 21948 (Fig 4 C, D), had reduced contralateral GFAP immunoreactivity that was restricted to lesion borders.

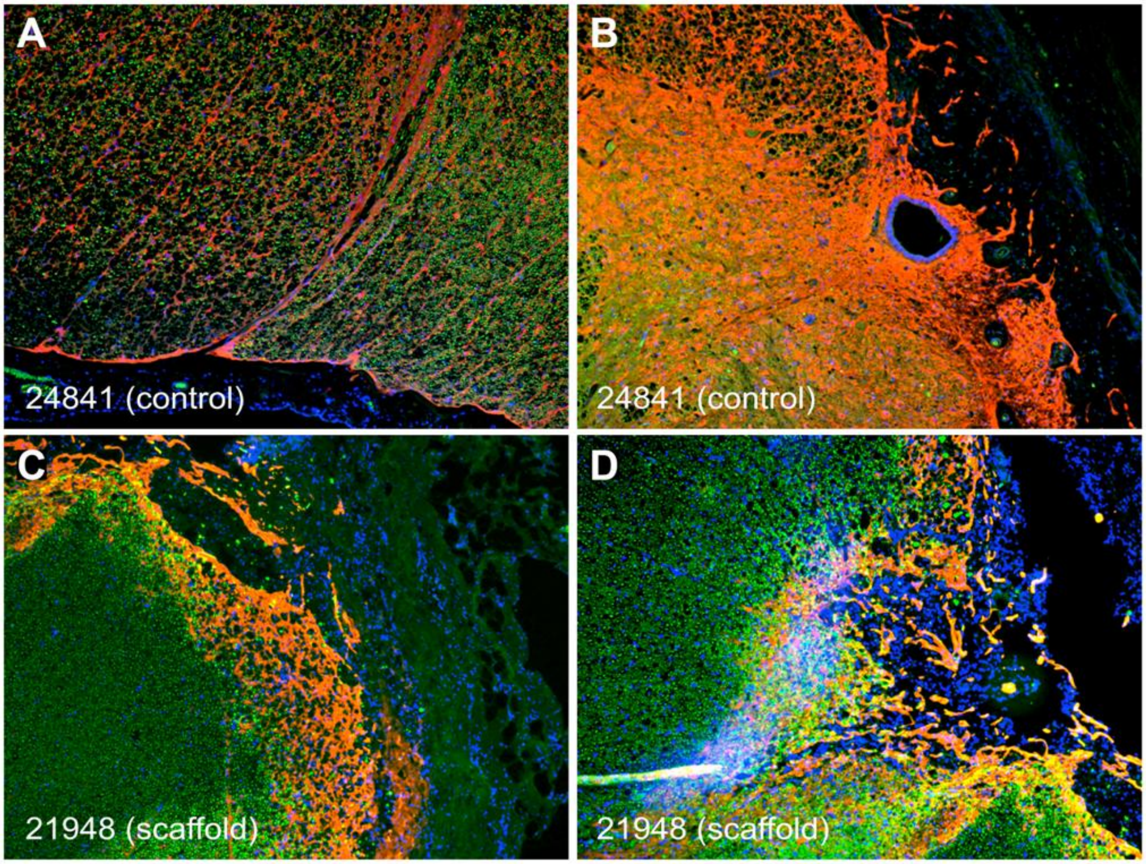

Figure 4. GFAP (red) and neurofilament (green) immunoreactivity in cross-sections of Macaca Mulatta monkey spinal cords near the lesion center following hemi-section surgical injuries. Cell nuclei were labeled with DAPI (blue). **A:** Ventral-lateral spinal cord region in a control subject. **B:** Extensive astrogliosis (red) throughout the tissue near the midline in a control subject. The central canal was preserved (blue). **C-D:** Dorsal and medial portions of the lesion in the scaffold-treated primate, showing reduced contralateral gliosis compared to controls restricted to lesion border.

Extent of lesion

Overall lesion volume, including areas of secondary injury, was estimated by measuring the longitudinal distance from the lesion with high GFAP immunoreactivity in labeled cross-sections (Table 3). The scaffold treated primate exhibited an approximately 56 percent shorter longitudinal distance of glial scarring, or astrocyte activation, rostal and caudal to the lesion 12 weeks post-injury compared to the two controls.

Table 1. Lesion volume, including secondary injury, as measured by elevation of glial fibrillary acidic protein (GFAP).

Treatment group (number)	**Rostral-caudal distance of elevated GFAP (mm)**
Controls (2 primates)	10.5 ± 0.7*
Scaffold (1 primate)	5

* mean ± standard deviation from two primates

References

1. Lavik EB, Hrkach JS, Lotan N, Nazarov R, Langer R. A simple synthetic route to the formation of a block copolymer of poly(lactic-co-glycolic acid) and polylysine for the fabrication of functionalized, degradable structures for biomedical applications. *Journal of Biomedical Materials Research* 2001;58(3):291-4.

2. Teng YD, Lavik EB, Qu X, Park KI, Ourednik J, Zurakowski D, Langer R, Snyder EY. Functional recovery following traumatic spinal cord injury mediated by a unique polymer scaffold seeded with neural stem cells. *Proc Natl Acad Sci U S A* 2002;99(5):3024-9.

3. Pritchard CD, Slotkin JR, Yu D, Dai H, Lawrence MS, Bronson RT, et al. Establishing a model spinal cord injury in the African green monkey for the preclinical evaluation of biodegradable polymer scaffolds seeded with human neural stem cells. *J Neurosci Methods* 2010;188(2):258-69.

4. Yavin E, Yavin Z. Attachment and culture of dissociated cells from rat embryo cerebral hemispheres on polylysine-coated surface. J Cell Biol 1974;62(2):540-546.

Acknowledgements

C.D.P. was supported by the MIT/CIMIT Medical Engineering Fellowship. This research was sponsored by InVivo Therapeutics Corporation.

IV.

The use of surface modified poly(glycerol-co-sebacic acid) in retinal transplantation

Christopher D. Pritchard (1), Karin M. Arnér (2), Rebekah A. Neal (3), William L. Neeley(1),
Peter Bojo (1), Erika Bachelder (4), Jessica Holz (4), Nicki Watson (4),
Edward A. Botchwey (3), Robert S. Langer (1), Fredrik K. Ghosh (2)

(1) Department of Chemical Engineering
Massachusetts Institute of Technology, Cambridge, MA, 02139, USA
(2) Department of Ophthalmology
Lund University Hospital, Lund, SE-22185, Sweden
(3) Department of Biomedical Engineering
University of Virginia, Charlottesville, VA, 22908, USA
(4) W.M. Keck Microscopy Facility
Whitehead Institute, Cambridge, MA, 02142, USA

Reprinted with permission from Elsevier: Biomaterials. 2010 Mar;31(8):2153-62.

Abstract

Retinal transplantation experiments have advanced considerably during recent years, but remaining diseased photoreceptor cells in the host retina and inner retinal cells in the transplant physically obstruct the development of graft-host neuronal contacts which are required for vision. Recently, we developed methods for the isolation of donor photoreceptor layers *in vitro*, and the selective removal of host photoreceptors *in vivo* using biodegradable elastomeric membranes composed of poly(glycerol-co-sebacic acid) (PGS). Here, we report the surface modification of PGS membranes to promote the attachment of photoreceptor layers, allowing the resulting composite to be handled surgically as a single entity. PGS membranes were chemically modified with peptides containing an arginine-glycine-aspartic acid (RGD) extracellular matrix ligand sequence. PGS membranes were also coated with electrospun nanofiber meshes, containing laminin and poly(epsilon-caprolactone) (PCL). Following *in vitro* co-culture of biomaterial membranes with isolated embryonic retinal tissue, composites were tested for surgical handling and examined with hematoxylin and eosin staining and immunohistochemical markers. Electrospun nanofibers composed of laminin and PCL promoted sufficient cell adhesion for simultaneous transplantation of isolated photoreceptor layers and PGS membranes. Composites developed large populations of recoverin and rhodopsin labeled photoreceptors. Furthermore, ganglion cells, rod bipolar cells and AII amacrine cells were absent in co-cultured retinas as observed by neurofilament, PKC and parvalbumin labeling respectively. These results facilitate retinal transplantation experiments in which a composite graft composed of a biodegradable membrane adhered to an immature retina dominated by photoreceptor cells may be delivered in a single surgery, with the possibility of improving graft-host neuronal connections.

Introduction

Retinal degenerative disease currently afflicts over 30 million patients worldwide [1]. This number is expected to increase in coming years, due not only to population growth but also the effect of aging populations, especially in developed countries. Age-related macular degeneration, hereditary retinal degeneration and retinal detachment involving the macula all lead to loss of photoreceptor function. The photoreceptor cells, located in the outer layer of the retina, are responsible for the transduction of light into electrical impulses. These signals are transmitted via neuronal connections through the inner retinal layers to the optic nerve and ultimately to the brain, resulting in a visual image. Therefore, retinal degenerative diseases lead to significant visual impairment and blindness.

When diseased photoreceptors are still present, but dysfunctional, current treatments may slow the progress of retinal degeneration [2] [3]. At this stage of disease, gene therapy may also provide alleviation of symptoms [4]. However, there are currently no therapies that regenerate lost photoreceptors.

The prospect of retinal transplantation offers the possibility of replacing photoreceptors lost by degenerative disease. Experiments have been ongoing for more than two decades in a multitude of animal models, but to date, retinal transplantation is not available as a clinical treatment [5] [6] [7].

A critical issue remaining before clinical trials using retinal transplantation can be attempted is to increase the ability of graft and host retinal neurons to form functional connective neuronal networks. Graft-host neuronal connections have been shown to occur to some extent in rabbit models [8] but not in porcine models, which have a retinal vasculature that is more akin to the human eye [9]. In the porcine model, integration is hampered by the presence of two cell layers, namely remaining inner retinal cells in the transplant and diseased host photoreceptors [6]. In order to improve the probability of functional connection between host and graft retina, it is hypothesized that these two physical barriers must be removed.

A recent development, in this field of study, involves the removal of host photoreceptors by the insertion of a thin biodegradable elastomeric membrane between the retinal pigment epithelium and the outer nuclear layer [10]. The membrane, made from poly(glycerol-co-sebacic acid) (PGS) [11] disrupts blood supply from the choroid to the retina leading to selective removal of the photoreceptor layer. *In vivo*, the membrane degrades completely within 14 days, leaving a host retina composed of isolated inner retinal layers prepared to receive a complementary photoreceptor transplant.

In the current study, we aimed to combine the PGS membrane with donor retinal tissue, to create a composite graft that can be transplanted into the subretinal space in a single surgery. The creation of such a composite graft composed of a biodegradable membrane adhered to a retina dominated by photoreceptor cells may in future experiments enhance neuronal integration by providing close contact of grafted photoreceptors with host inner retinal cells. PGS membranes were chemically modified with peptides containing an arginine-glycine-aspartic acid (RGD) extracellular matrix ligand sequence [12]. Additionally, nanofiber meshes, composed of laminin, poly(epsilon-caprolactone) (PCL) or a blend of laminin and PCL, were electrospun onto PGS membranes.

The biomaterial membrane is intended ultimately to serve as a clinical paradigm that can be modified further to incorporate drugs or proteins with the aim of enhancing synaptic connections between grafts and the host nervous system. For example, neurotrophic factors such as brain derived neurotrophic factor (BDNF) or glial cell derived neurotrophic factor (GDNF) have the ability to stimulate neuron growth [13] and may promote neurite sprouting from the transplant.

Materials and Methods

All compounds and solvents were obtained from Sigma-Aldrich, St. Louis, MO, USA unless otherwise stated.

Preparation of poly(glycerol-co-sebacic acid) Membranes

Poly(glycerol-co-sebacic acid) (PGS) branched polymer was prepared by poly-condensation as previously described [11]. Briefly, equimolar amounts (0.989 mol) of re-crystallized sebacic acid and anhydrous glycerol were charged to an oven-dried round bottom flask and reacted with stirring at 120°C under argon. After 21 hours, vacuum was applied and the mixture was reacted for another 64 hours. The resulting material formed a white wax at room temperature.

Cross-linking of the PGS to an elastomer was carried out in a class 10,000 clean room. A 10:1 prepolymer:hardener mixture of poly(dimethylsiloxane) (PDMS) (Sylgard 184, Dow Corning, Midland, MI) was outgassed under vacuum and cured in a 10 cm Petri dish for 1 hour at 60°C. The resulting 10 cm diameter PDMS slab was plasma oxidized for 1 minute to create a hydrophilic surface. The top surface was spin coated at 3000 rpm for 30 seconds with a 61.5 wt. % aqueous sucrose solution (saturated at room temperature and 0.45 µm syringe filtered). The sucrose-coated PDMS was subsequently baked at 130 °C for 10 min and transferred to a hotplate at 120°C. Molten PGS wax (120 °C) was poured onto the sucrose-coated PDMS slab, covering the entire surface, and subsequently cured at 120 °C under a 15 millitorr vacuum until the PGS lost any adhesiveness to a stainless steel spatula.

Subsequently, the mold was submerged in 18 MOhm water overnight and the PGS was peeled from the PDMS underwater. The resultant PGS disk was approximately 3 mm thick.

The PGS disk was cut into 5 x 5 x 3 mm blocks, embedded in Tissue-Tek OCT compound (Sakura, Torrance, CA) and rapidly frozen by immersion in ethanol cooled with dry ice. Frozen PGS was cryo-sectioned into 30 µm membranes at -30˚C with a Shur/Sharp Heavy Duty razor blade (TBS, Durham, NC). Thicker blades (0.5 mm or greater) and slow sectioning speeds were necessary to reduce vibration and warming of the blade from friction. Membrane thickness and uniformity was confirmed by scanning electron microscopy.

PGS – Peptide coupling

Membrane activation

PGS samples (5 mm x 5 mm) were individually treated in a 0.1 w/v % solution of 1-(3-dimethylaminopropyl)-3-ethylcarbodiimide (EDC; 0.1 g) in 0.1 N (2-(N-morpholino)-ethanesulfonic acid (MES; 2.13 g) buffer in 18 MOhm water (100 mL, pH 3.5). Each sample was immersed in 1.5 mL of the EDC solution in 1.7 mL Eppendorf tubes at room temperature for 1 hour, whilst shaking with a vortex mixer. The samples were washed in MES buffer (1 x 10 minutes; 1.5 mL / sample), and then in 18 MOhm water (2 x 10 minutes; 2 x 1.5 mL / sample). The activated PGS samples were directly used in the coupling reactions.

Membrane coupling to peptide GRGDS

The activated PGS sample (5 mm x 5 mm) was immersed into a 1 mM solution of the peptide sequence GRDGS (Anaspec, Freemont, CA) in phosphate buffered saline (PBS; pH 7.3) (1.5 mL) during 2 hours at room temperature, under shaking. The sample was rinsed 3 times for 10 minutes with 1 mL PBS and then with 1 mL 18 MOhm water for 10 minutes.

X-ray photoelectron spectroscopy analysis of peptide modified membranes

The surface chemical composition of the sample was determined by X-ray photoelectron spectroscopy (XPS) using a Surface Science Instruments SSX-100, equipped with a monochromatic aluminum X-ray source at 1486.8 eV. Charge neutralization was achieved using an electron flood gun. The vacuum in the analysis chamber was less than $2x10^{-9}$ torr during analysis. Photoelectrons were collected at an angle of 55 ° from the surface normal. A hemispherical analyzer was used with a pass energy of 150 eV for surveys and 50 eV for high-resolution scans. The peak areas were determined using Shirley background subtraction. The intensity ratios were converted into atomic concentration ratios using CasaXPS processing software (Casa Software Ltd., Cheshire, UK), which takes into account the instrument transmission function and provides a standard library of empirically-determined relative sensitivity factors.

Fabrication of electrospun nanofibers

Nanofibers consisting of poly(epsilon-caprolactone) (PCL) laminin and a blend of 10 wt. % laminin in PCL of approximately 100 nanometers were electrospun onto 30 micron PGS sheets to create a bi-layer biomaterial membrane. Neuroretinal explants were subsequently cultured on a culture membrane with the outer layers facing downward and the PGS-nanofiber membranes on top, with the nanofiber side of the PGS sheet facing downward. Type 1 Laminin was isolated from murine Englebreth-Swarm-Holme tumor as previously described [14]. The laminin was provided as a gift by Stemgent, Inc. (Cambridge, MA). Electrospinning followed previously described protocols [15]. For laminin nanofibers, lyophilized laminin was dissolved in 1,1,1,3,3,3-hexafluoro-2-propanol (HFP) at 3 w/v % at 4 °C overnight. The solution was then mounted into an Aladdin syringe pump (World Precision Instruments, Sarasota, FL) using a

disposable syringe and 18 gauge needle. PGS sheets mounted on glass cover slips were placed on the collector plate, and the laminin solution was dispensed at a flow rate of 1 mL/hr and driving voltage of 15 kV across a 15 cm vertical gap onto the grounded copper collector, and hence onto the PGS sheets. Samples were dried completely and stored in dessicant at -20 °C. Laminin-PCL blend nanofibers were electrospun in a similar manner. A solution consisting of 10 wt. % laminin and 90 wt. % PCL with 8 w/v % total polymer dissolved in HFP was used as the initial solution. The same procedure as for laminin was used to electrospin the blend onto PGS sheets, though the driving voltage was increased to 20 kV to compensate for the higher viscosity of this solution.
18 wt. % PCL was dissolved in 1:1 THF:DMF and electrospun at 20 kV in the same manner to fabricate PCL nanofibers.

Characterization of electrospun nanofibers

Samples were air dried for 24 hours, mounted on aluminum stubs, and coated with a thin layer of carbon for scanning electron microscopy. A JSM-5910 General Purpose Scanning Electron Microscope(JEOL, Tokyo, Japan) was used to image the samples. To study the effect of hydration, samples were air dried after 5 days in culture medium. For scanning electron microscopy, samples were mounted on aluminum stubs and sputter coated with gold, and imaged using a JEOL 6400 Scanning Electron Microscope with Orion image processing (JEOL, Tokyo, Japan). Diameter measurements were made using the *measure* tool in Image J (NIH, Bethesda, MD), with at least 50 measurements per sample.

Culture procedure

Porcine tissue isolation

Eyes from Yorkshire/Hampshire pigs (gestational age of 114 days) were obtained from a local breeder (Lund, Sweden) and used for all experiments. Retinal tissue from E45 (45 days after conception) and E49-50 was used for culturing experiments, and E60 and E70 specimens were obtained as *in vivo* controls. The pregnant sow was euthanized by means of captive bolt and incision of the carotid arteries. The fetuses were collected by caesarean section and euthanized by decapitation. Both eyes were enucleated and immediately immersed in ice-cold CO_2-independent medium. The neuroretinas were carefully dissected free from the retinal pigment epithelium (RPE) and hyaloid vascular system with fine forceps. The optic nerve was thereafter cut with micro-scissors and neuroretinal pieces measuring approximately 4x4 mm were explanted on Millicell®-HA 0.45- µm culture plate inserts with the photoreceptor layer towards the membrane. All neuroretinas were put in culture within 240 minutes.

Explants were cultured in 1.2 mL Gibco D-MEM F12 medium –L-Glutamine (Gibco, Paisley, UK) supplemented with 10 vol. % fetal calf serum. A cocktail containing 2 mM L-glutamine, 100 U/mL penicillin and 100 ng/mL streptomycin was added, and the retinas were maintained at 37 °C with 95 % humidity and 5 % CO_2.

Co-culture of retinal layers with biomaterial membranes

After two days, PCL-PGS and Laminin-PCL-PGS membranes measuring 2x3 mm were added to the explanted retinal specimens (12 each) while another 12 pieces were kept in culture without the addition of a membrane as *in vitro* controls. At this time half of the culture medium was exchanged, and this procedure was then repeated every second day. Specimens were kept under culture conditions for either 1 or 2 weeks (7-9 or 14-16 days).

All proceedings and treatment of animals were in accordance with the guidelines and requirements of the Government Committee on Animal Experimentation at Lund University and with the ARVO Statement for the Use of Animals in Ophthalmic and Vision Research.

Histology

For histologic examination, the explants were fixed for 1 hour in 4% formalin, pH 7.3 in a 0.1 M Sørensen's phosphate buffer (PB). After fixation, the specimens were washed with 0.1 M Sørensen's PB, and then washed again using the same solution containing sucrose of rising concentrations (5-25%). They were then sectioned at 12 µm on a cryostat, and each 10th slide was stained with hematoxylin and eosin according to standard procedures.

For immunohistochemical staining, sections were incubated at room temperature with phosphate buffered saline (PBS) containing 0.25 % Triton X-100 and 1 % bovine serum albumin for 30 minutes. This was followed by incubation of the slides overnight with primary antibodies (Table 1). After incubation, the slides were rinsed in PBS and incubated with Texas-red-conjugated secondary antibodies (Jackson Immunoresearch, West Grove, PA, USA) for 50 minutes. in room temperature and thereafter rinsed again and finally mounted in custom made Vectashield mounting media containing DAPI (4´,6-diaminidin-2-phenylindoldihydrochloride; Vector laboratories, California, USA).

For recoverin and vimentin double-labeling, the tissue was incubated with recoverin and vimentin antibodies for 18 to 20 hours and rinsed in PBS-Triton. Subsequently, the tissue was incubated for 45 minutes in darkness with a mixture of the secondary antibodies conjugated with two fluorophores: anti-rabbit fluorescein isothiocyanate (FITC; Southern Biotechnology;

Birmingham, AL, USA) and anti-mouse Texas red. The dilution of each secondary antibody was 1:200.

Neuroretinas derived from E60 and E70 eyes were used to compare cultured specimens with the corresponding *in vivo* counterparts. Sections from adult porcine retinas were used as positive controls. Negative controls were obtained by performing the complete labeling procedure without primary antibody on retinal sections from adult pigs. Photographs were obtained with a digital camera system (Olympus, Tokyo, Japan). Photographs were adjusted for brightness and contrast digitally.

Table 1. Specification of immounohistochemical markers.

Antigen	**Antibody name**	**Target cell**	**Species**	**Dilution**	**Source**
Neurofilament 160 KDa	Anti-neurofilament 160 clone NN18	Ganglion cells (Horizontal cells)	Mouse monoclonal	1:500	Sigma, St Louis, MO, USA
Recoverin	Anti-recoverin	Rod and cone photoreceptors	Rabbit polyclonal	1:10000	Chemicon International, Ca, USA
Vimentin	Mouse anti-vimentin	Müller cells	Mouse monoclonal	1:500	Chemicon International, Ca, USA
Rhodopsin	Rho4D2	Rod photoreceptor	Mouse monoclonal	1:100	Kind gift of Prof. RS Molday, Vancouver, Canada
Parvalbumin	Mouse anti-Parvalbumin	AII amacrine cells	Mouse monoclonal	1:1000	Sigma, St Louis, MO, USA
PKC	Phospho-PKC (pan)	Rod bipolar cells (Photoreceptor outer segments)	Rabbit polyclonal	1:200	Cell Signaling, Beverly, MA, USA

Results

Membrane properties

PGS sheets

A variety of approaches for the fabrication of PGS membranes were attempted. A microtome was used with and without the PGS embedded in paraffin. The microtome was unable to cut PGS, and the material compressed at the point of contact with the microtome blade. Subsequently, a cryo-sectioning technique employed to fabricate PGS sheets was able to create 30µm thick membranes (Fig. 1A). A slightly wavy surface was produced due to blade vibrations, as seen in the image by light and dark contours on the membrane surface. Compared to the edge of the membrane, which was cut by a standard laboratory razor blade, the cryo-sectioning technique created a smooth surface. To optimize the cryo-sectioning technique, the type of blade, temperature of the instrument, temperature of the frozen block, size of the frozen block and surface area of the PGS pieces were varied to identify conditions that would allow sectioning. After suitable parameters were obtained, we investigated how thin the PGS could be sectioned. A thickness of 30 µm was found to be the limit, as 20 µm sections were too fragile and readily folded upon themselves.

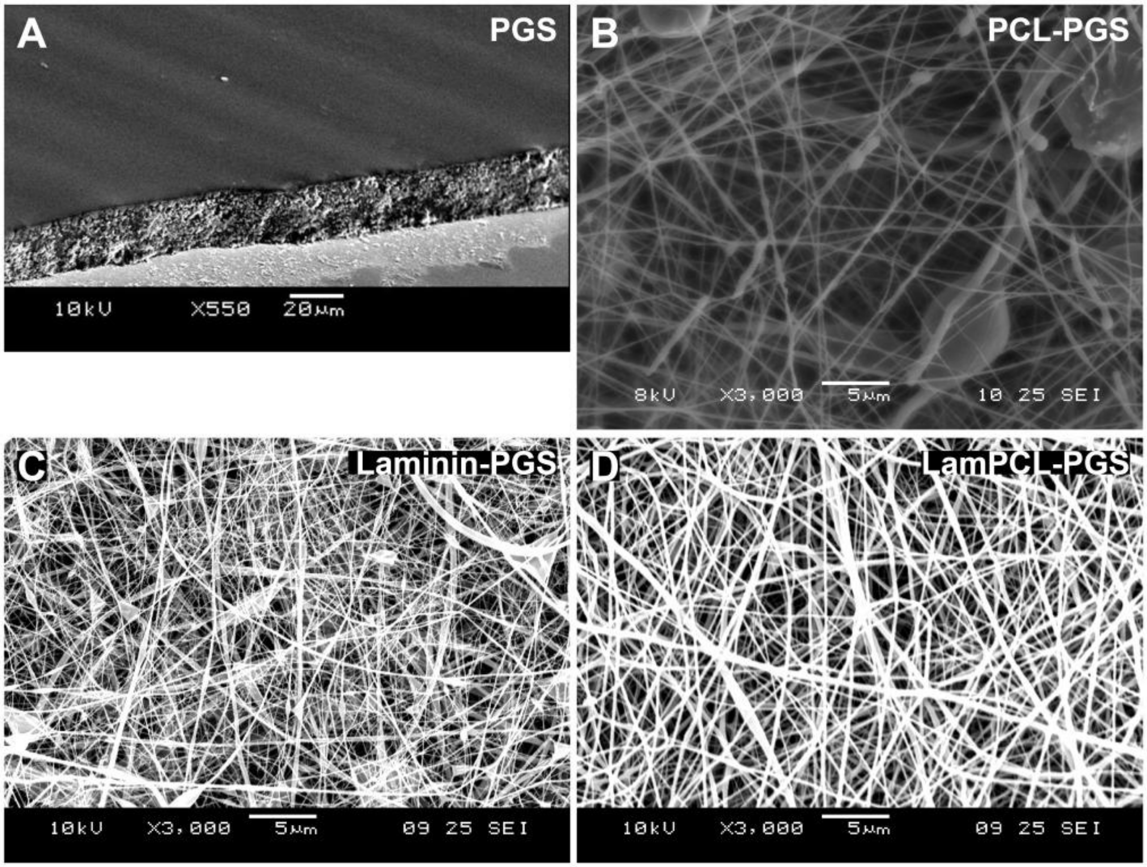

Figure 1. Scanning electron microscope images of membranes. **A:** 30 µm PGS sheet. Edge view at 60°. **B-D:** Nanofibers electrospun onto PGS sheets (**B:** PCL, **C:** Laminin, **D:** Laminin-PCL nanofibers). Top view.

GRGDS peptide modification of PGS sheets

Analysis by XPS gave: C1s: 284.526 eV (98.56 %); N1s: 399.335 eV (1.44 %). Considering the theoretical monomer unit ((PGS)y+(PGS-GRGDS)x), i.e. (($C_{13}H_{22}O_5$)y+($C_{30}H_{52}N_8O_{13}$)x), where $x + y = 1$, we calculated the atomic ratios as: $N/C = 8x/(30x+13(1-x))$ and $O/C = (13x+5(1-x))/(30x+13(1-x))$. From the experimental value ($N/C = 0.0146$), we found $x = 0.0245$, i.e. approximately 2.45 % surface functionalization.

Characterization of electrospun nanofibers on PGS sheets

A thin-layered random network of PCL nanofibers was created on top of the PGS sheets (Fig. 1B). While some bead defects are visible, the overall morphology remains fibrous in structure. The laminin-PCL blended nanofibers created a denser network with fewer bead defects and visibly thicker fibers than PCL alone (Fig. 1D). Electrospinning of laminin alone also created a dense network with few defects, but markedly finer nanofibers than PCL and laminin-PCL blends (Fig. 1C). Table 2 reports the diameters of the three meshes. The mean diameters for dry nanofibers increased significantly with decreasing concentration of laminin from 65.38 nm for pure laminin to 101.50 nm for laminin-PCL blends to 175.12 nm for pure PCL. A one-way ANOVA showed significance for differences among groups ($p < 0.01$). Following hydration in culture medium, the mean diameter of the laminin-PCL blended nanofibers almost doubled to 199.21 nm, indicating that the networks are prone to swelling under aqueous conditions; however, the fibrous morphology of the mesh was retained (image not shown). Furthermore all of the networks possess a significant distribution of nanofiber size as evidenced by the standard deviations.

Table 2. Measurements of diameters of nanofibers electrospun onto PGS membranes. ANOVA shows significant difference between all groups ($p < 0.01$).

	Nanofiber material			
Size (nm)	***PCL***	***Laminin***	***Laminin-PCL***	***Laminin-PCL (hydrated)***
Mean	175.12	65.38	101.50	199.21
Minimum	93.04	15.74	22.26	62.50
Maximum	294.22	140.81	267.41	447.43
St.Dev.	39.70	23.34	49.09	90.59

Surgical handling results

Table 3 shows the results of mechanical integrity of the co-cultured membranes during loading/unloading into the transplantation instrument for a variety of biomaterial membranes and retinas. The PGS membranes without chemical or physical modifications cultured for 7 to 14 days with E40 porcine retinas demonstrated insufficient adherence between the biomaterial and retina during transplantation.

By contrast, the RGD peptide modified membranes (RGD-PGS), as well as the PGS membrane coated with pure laminin nanofibers (Laminin-PGS), demonstrated improved adherence over PGS. However, the membrane and retina dissociated after the composite was pushed out of the transplantation device, rendering the RGD-PGS and Laminin-PGS membranes unsuitable for *in vivo* transplantation in pig models.

Two of the nanofiber mesh coated PGS membranes (PCL-PGS and Laminin-PCL-PGS) seemed to integrate quite well with the porcine retinas. It was possible to dissect these composites from the culture membrane, place them in the transplantation device, and eject them without the two components dissociating.

Table 3. Surgical handling results. Letter N represents no attachment. Letter A represents attachment, but insufficient for surgical application. Letter Y represents sufficient attachment for retinal transplantation.

	Membrane type				
Retina type	***PGS***	***RGD-PGS***	***PCL-PGS***	***Laminin-PGS***	***Laminin-PCL-PGS***
Pig (E40-50)	N	A	Y	A	Y
Pig (E99)			Y		Y

Histology and immunohistochemistry

Histological sections showed that some porcine retinal explants were double folded, whether or not they were co-cultured with biomaterial membranes. This was probably due to the fact that some of the vitreous membrane remained in place during isolation of the retinal layer. The vitreous membrane should ideally be completely removed prior to transplantation. PGS membranes co-cultured for 7 to 14 days with E40 porcine retinas developed photoreceptors (images not shown). The cells in the retinas co-cultured with PGS were somewhat less organized than *in vitro* controls (images not shown). However, the controls were more folded, indicating that the addition of PGS membranes flattened the retinal cultures. In retinas co-cultured with RGD-PGS sheets, processes extending from retinal cultures towards the RGD-PGS sheets were observed in some sections (images not shown).

Neurofilament staining in retinas co-cultured *in vitro* with PCL-PGS or Laminin-PCL-PGS membranes for 9 or 16 days demonstrated an absence of ganglion cells in these retinas (Fig. 2A-D). Neurofilament labeling was evident in the ganglion cell layer for E49 *in vitro* controls cultured for 7 days (Fig. 2E), but eventually disappeared from the nerve fiber layer (NFL) after 14 days (Fig. 2F). By comparison, neurofilament positive axons were intensely labeled in the NFL of *in vivo* controls (Fig. 2G, H).

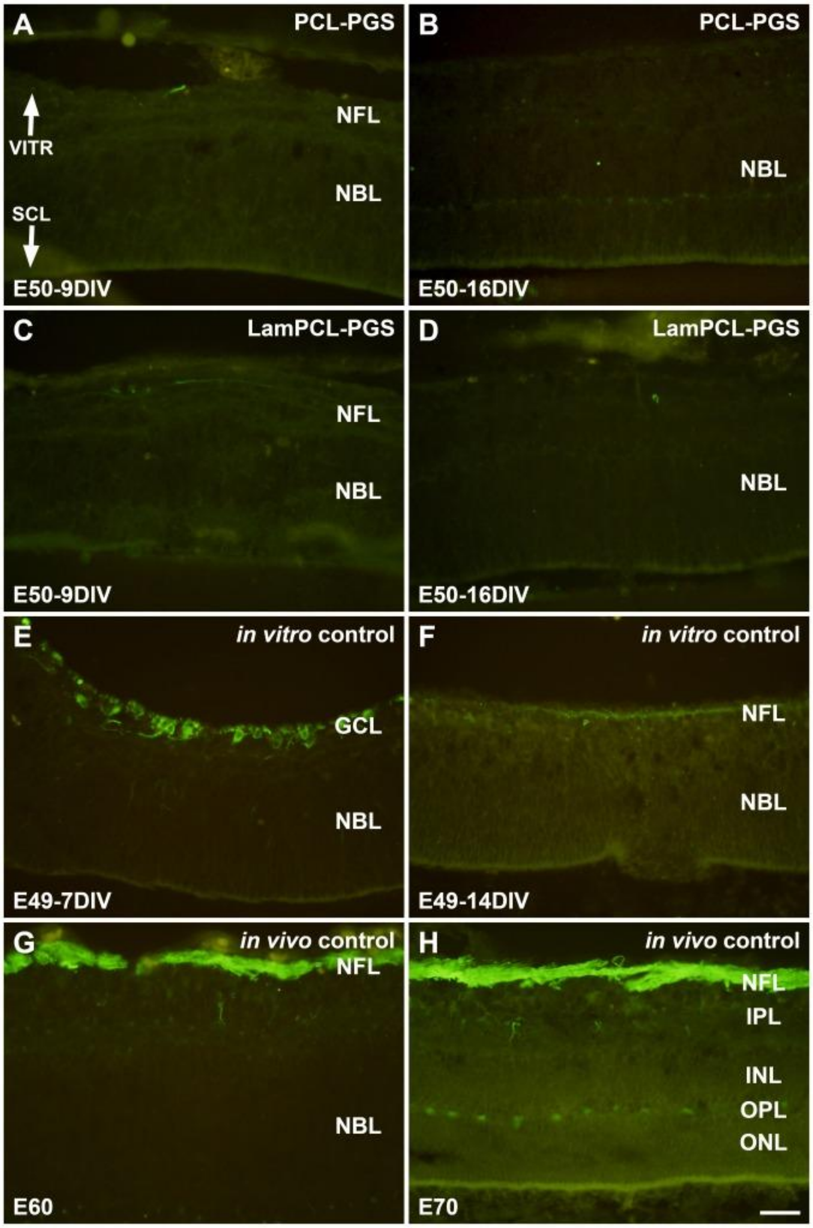

Figure 2. Neurofilament staining of fetal porcine retina. **A-D:** E50 retinas co-cultured for 9 (**A**, **C**) and 16 (**B**, **D**) days *in vitro* with PGS membranes coated with PCL (**A**, **B**) or laminin-PCL blend (**C**, **D**) nanofibers. Neurofilament staining is absent in the retinas co-cultured with nanofiber coated PGS membranes. **E-F:** E49 retinas cultured for 7 (**E**) and 14 (**F**) days *in vitro*. Neurofilament positive ganglion cells are visible in the ganglion cell layer (**E**). However, neurofilament staining is less evident following longer culture *in vitro* (**F**). G-H: E60 (**G**) and E70 (**H**) *in vivo* retina specimens. Neurofilament positive axons are visible in the nerve fiber layer (**G**). Intensely labeled neurofilament positive axons in the nerve fiber layer are visible, and horizontal cells in the outer part of the INL are also labeled (**H**). Neurofilament staining is less pronounced in *in vitro* specimens (**E-F**) compared to *in vivo* specimens (**G-H**). VITR, vitreal (inner) aspect, SCL, sclera (outer) aspect. Scale bar = 50 microns.

PKC labeled rod bipolar cells and parvalbumin labeled AII amacrine cells were not evident in retinas co-cultured with biomaterial membranes or in *in vitro* controls (Fig. 3A-F). Tube-like structures appeared as rosettes in some sections (indicated by arrows in Fig. 3B, C). In E70 *in vivo* controls, PKC labeled rod bipolar cells were visible in the inner nuclear layer (INL) and ganglion cell layer (GCL). Neurites were intensely labeled with PKC in the inner plexiform layer (IPL) (Fig. 3G). Parvalbumin labeled amacrine cells were present in the GCL (Fig. 3H).

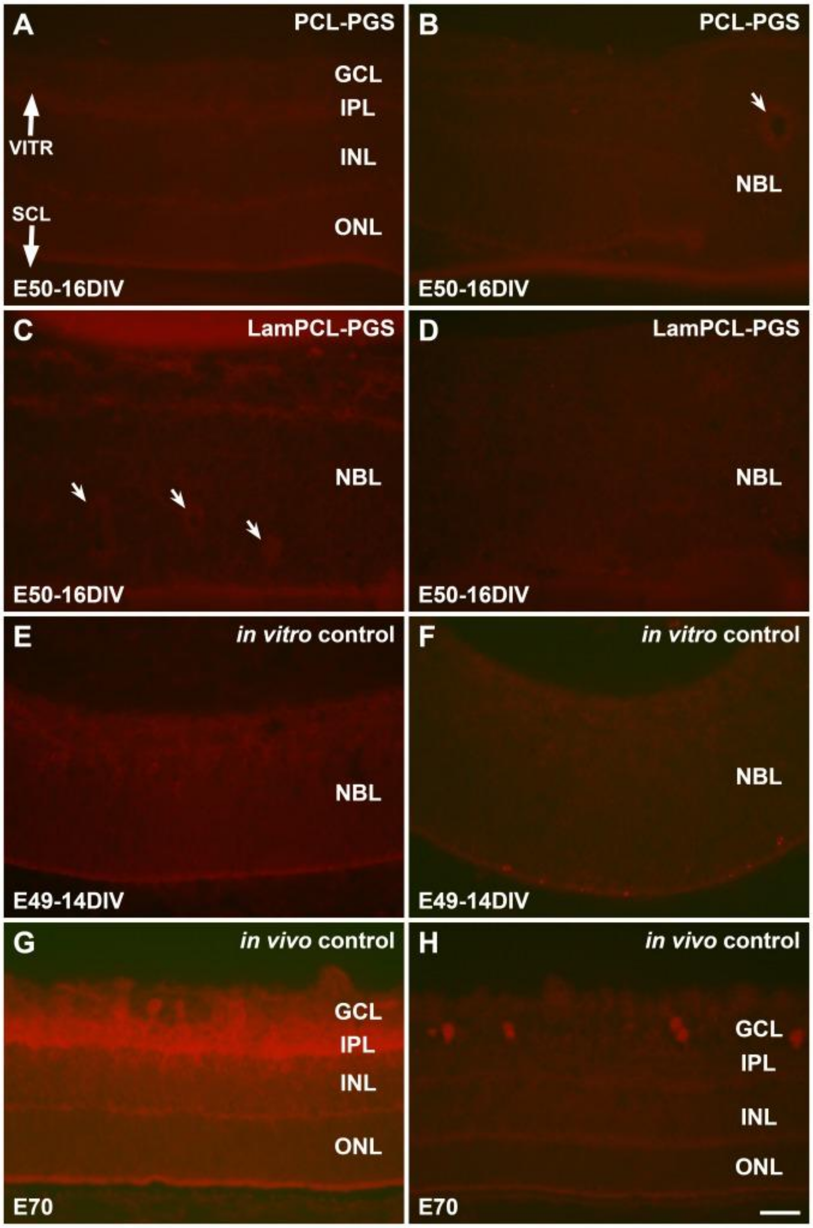

Figure 3. PKC (left column) and parvalbumin (right column) staining of fetal porcine retina. **A-D**: E50 retinas co-cultured for 16 days in vitro with PGS membranes coated with PCL (**A**, **B**) or laminin-PCL blend (**C**, **D**) nanofibers. Rosettes (arrows) are present in some sections (**B**, **C**). **E-F:** E49 retinas cultured for 14 days *in vitro*. PKC labeled rod bipolar cells and parvalbumin labeled amacrine cells are not abundant in any retinas cultured *in vitro* (**A-F**). **G-H:** E70 *in vivo* retina specimens. PKC labeled rod bipolar cells are seen in the inner part of the INL and in the GCL with intense labeling of neurites in the IPL (**G**). Parvalbumin labeled amacrine cell bodies are found in the GCL (**H**). VITR, vitreal (inner) aspect, SCL, sclera (outer) aspect. Scale bar = 50 microns.

Large populations of recoverin labeled photoreceptors were present in all retinas co-cultured with biomaterial membranes (Fig. 4A-D). Recoverin labeled photoreceptors were located predominately in the outer retinal layers of *in vitro* controls (Fig. 4E, F), and in the outer nuclear layer (ONL) of *in vivo* controls (Fig. 4G, H).

Vimentin labeled Müller cells were well organized in retinas co-cultured with biomaterial membranes, with processes apparently extending into the nanofiber networks (Fig. 4A-D). Vertically arranged vimentin labeled fibers were present in inner retinal layers of *in vitro* and *in vivo* controls (Fig. 4E-H). The retinas co-cultured with membranes did not express vimentin at the same intensity as the controls.

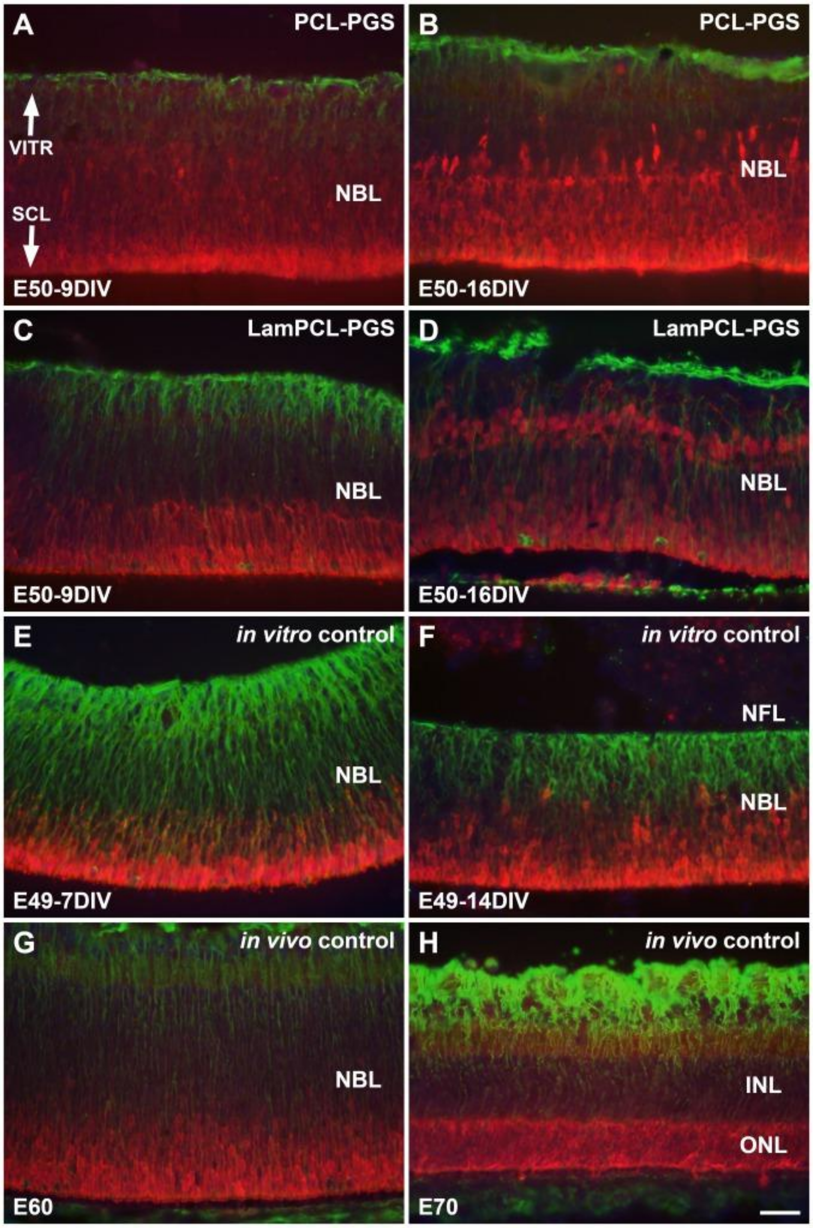

Figure 4. Recoverin (red) and vimentin (green) double-labeling of fetal porcine retina. **A-D:** E50 retinas co-cultured for 9 (**A**, **C**) and 16 (**B**, **D**) days in vitro with PGS membranes coated with PCL (**A**, **B**) or laminin-PCL blend (**C**, **D**) nanofibers. Müller cells are well organized, large populations of recoverin labeled photoreceptors are visible, and vimentin labeled processes extend into the nanofiber network. **E-F:** E49 retinas cultured for 7 (**E**) and 14 (**F**) days *in vitro*. Recoverin labeled photoreceptors are found mainly in outer retinal layers, and vertically arranged vimentin labeled fibers are visible with strong intensity corresponding to inner retinal layers. **G-H:** E60 (**G**) and E70 (**H**) *in vivo* retina specimens. Recoverin labeled photoreceptors are visible with highest intensity in the outer retinal layers, and vertically arranged vimentin labeled fibers are visible (**G**). Recoverin labeled photoreceptor cells are seen in the entire ONL, and Müller cell processes display vimentin labeling throughout the retina with strong intensity

corresponding to the inner retinal layers (**H**). Vimentin labeling of Müller cells is less intense in retinas co-cultured with PGS-nanofiber membranes (**A-D**) compared to controls (**E-H**). VITR, vitreal (inner) aspect, SCL, sclera (outer) aspect. Scale bar = 50 microns.

Rhodopsin labeling revealed an abundance of rod photoreceptors in outer nuclear layer (ONL) of retinas co-cultures with biomaterial membranes (Fig. 5A-D). Rhodopsin labeled rods were also present in *in vitro* and *in vivo* controls (Fig. 5E-H).

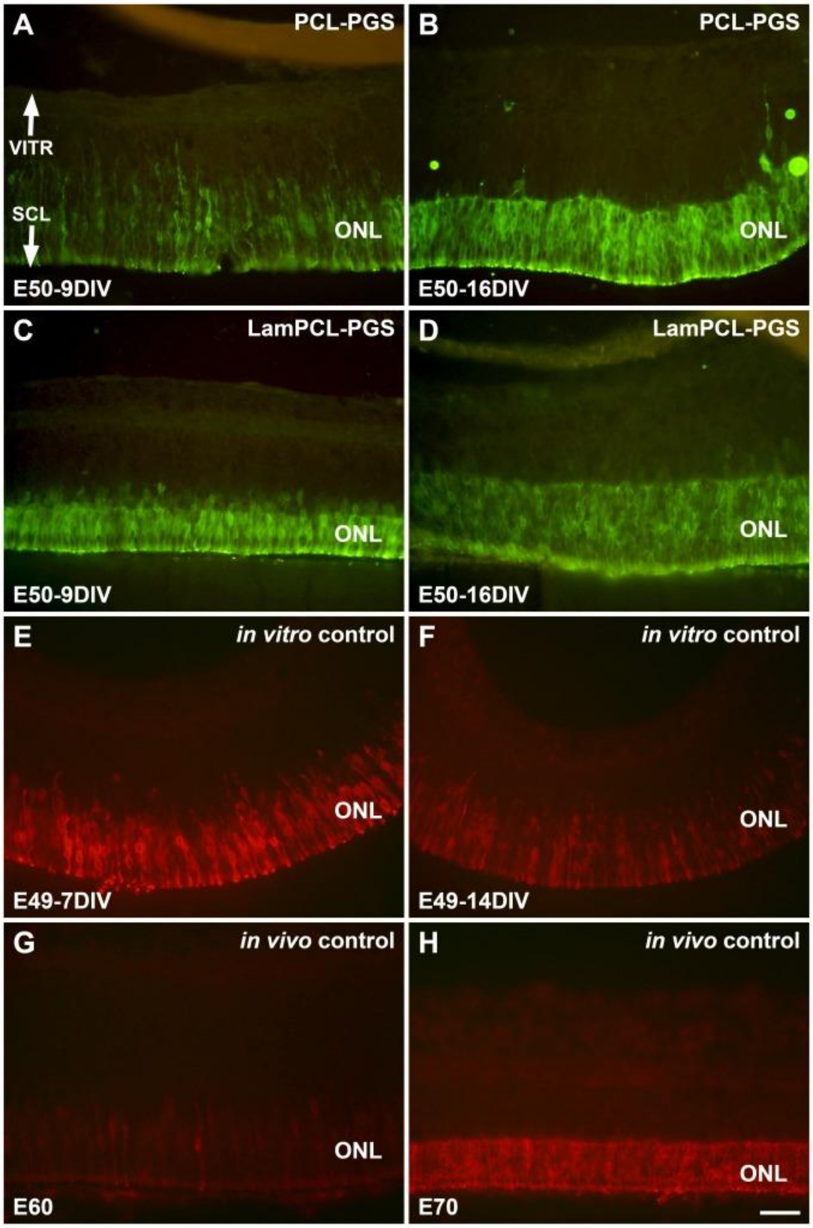

Figure 5. Rhodopsin staining of fetal porcine retina. **A-D:** E50 retinas co-cultured for 9 (**A**, **C**) and 16 (**B**, **D**) days *in vitro* with PGS membranes coated with PCL (**A**, **B**) or laminin-PCL blend (**C**, **D**) nanofibers. Rhodopsin labeled rod photoreceptors are visible in the outer nuclear layers of retinas, and survive at least 16 days in co-culture with PGS-nanofiber membranes. **E-F:** E49 retinas cultured for 7 (**E**) and 14 (**F**) days *in vitro*. Rhodopsin labeled rod photoreceptors are visible in the outer nuclear layer. **G-H:** E60 (**G**) and E70 (**H**) *in vivo* retina specimens. Rhodopsin labeled rod photoreceptors with neurites extending inwards as well as outwards to the margin of the retina are visible (**G**). Rhodopsin labeled rod photoreceptors are visible in the outer nuclear layer (**H**). VITR, vitreal (inner) aspect, SCL, sclera (outer) aspect. Scale bar = 50 microns.

Discussion

In a previous study, 45 µm thick membranes were implanted into the subretinal space of rabbits, with one case of mechanical noncompliance resulting in damage to the RPE and choroid [10]. In this study, we were able to fabricate 30 µm membranes using a cryo-sectioning technique. By making the membranes thinner, they also became more flexible. Therefore mechanical disruption of the retina during and following implantation, as well as subretinal gliosis, may be reduced by using 30 µm membranes. PGS membranes without modification did not adhere firmly to the cultured retinas. However, the controls were more folded, indicating that the addition of PGS membranes flattened the retinal cultures. This is considered desirable, as it may help preserve the laminated morphology of the photoreceptor layer following transplantation.

A nanofiber architecture was necessary to provide sufficient attachment of porcine retinal layers for surgical handling and transplantation. Nanofibers have been demonstrated to be effective at providing a bridge within peripheral nerve tubes for axonal regeneration both *in vitro* and *in vivo* [16] [17] [18]. Polymeric nanofibers have also exhibited nerve guidance capabilities in the central nervous system. Structure and geometry have been shown to play very significant roles in cell adhesion and guidance. For example, smaller diameter nanofibers appear to yield longer and faster outgrowth of neurites than larger diameter nanofibers [19]. The paper also reports significantly longer outgrowth of neurites occurred on laminin coated fibers compared to fibronectin fibers with fibers of the same diameter. In another study, collagen-functionalized nanofibers improved cell adhesion and migration compared to non-functionalized nanofibers [20]. The authors suggested that functionalizing nanofibers with fibronectin or laminin may potentially have a greater effect than collagen by stimulating integrin binding through peptide sequences such as RGD, IKVAV and YISGR. The addition of laminin to the nanofibers coating the PGS sheets was to promote neurite in-growth into the membrane and to facilitate neuronal connection between graft and host following degradation of the biomaterial by orienting graft neurites towards host inner nuclear layers. However, no evidence of neurite in-growth into the nanofiber mesh was observed *in vitro* in this study. Furthermore, based on the antibodies tested in this study, no differences were detected between membranes with PCL nanofibers and membranes with PCL and laminin blended fibers. The structural arrangement and bioactivity of the laminin following electrospinning warrants further investigation.

In some histological sections of retinas co-cultured with nanofiber coated membranes, it appeared as though some tissue elements have penetrated the fiber network showing promising in-growth (images not shown). These processes label for vimentin and are thus at least partly of Müller origin. Comparing retinas co-cultured with membranes to *in vitro* controls it was observed that the retinas with membranes do not express vimentin in Müller cells at the same intensity as controls. Low vimentin expression in Müller cells is difficult to interpret. The cells display a normal structure, but the membrane may influence nutrition.

Persisting inner nuclear cells in the donor tissue are thought to inhibit integration of donor photoreceptors with the host inner nuclear layers. Therefore, the removal of these cells prior to transplantation may be favourable for neuronal connection of the co-cultured retinal layer upon degradation of the biomaterial. Neurofilament remains for some time in E49 *in vitro* controls cultured for 7 days (E49-7DIV), but not in the PCL-PGS or Laminin-PCL-PGS cultured specimens. This removal of ganglion cells may be due to retrograde degeneration as the optic nerve is cut, enhanced by the ischemia induced by the sectioning of retinal vessels as well as placing the biomaterial membranes on top of the retinal layers *in vitro*. Even in E60 *in vivo* controls, PKC (rod bipolars) and parvalbumin (amacrine cells) are not abundant, indicating that retinal tissue isolated prior to 60 days post-embryogenesis is ideal for transplantation.

In a prior study, the 45 µm PGS membranes degraded within 28 days in the subretinal space in rabbits [10]. This duration was sufficiently long enough for the selective removal of host photoreceptors in rabbit eyes. Whilst the 30 µm PGS membranes will degrade more rapidly, PCL is likely to degrade over a longer period of time *in vivo* than PGS. Therefore, the nanofibers may persist for longer than the PGS membrane. This may or may not be advantageous. Pig photoreceptors are likely to be more resilient to ischemic trauma than rabbits, and may require a longer separation time from the retinal pigment epithelium (RPE). On the other hand, a prolonged separation between donor photoreceptors and the host inner nuclear layer (INL) may lead to undesired subretinal gliosis.

Conclusion

We have shown that electrospun nanofibers composed of laminin and PCL promoted sufficient cell adhesion for simultaneous transplantation of isolated photoreceptor layers and PGS membranes. Composites developed large populations of recoverin and rhodopsin labeled photoreceptors. Furthermore, ganglion cells, rod bipolar cells and AII amacrine cells were absent in co-cultured retinas as observed by neurofilament, PKC and parvalbumin labeling respectively. It may now be possible to conduct retinal transplantation experiments in which a composite graft composed of a biodegradable membrane adhered to an immature retina dominated by photoreceptor cells are delivered in a single surgery. By selective removal of host photoreceptors and delivery of a photoreceptor transplant without inner retinal cells, this approach may improve graft-host neuronal connections.

Acknowledgements

We thank Kurt Broderick for assistance with clean room operation (MTL, MIT, Cambridge, MA), Dr. Anthony Garratt-Reed and Libby Shaw for assistance with SEM and XPS (CMSE, MIT, Cambridge, MA), Jonathan Shu for assistance with XPS (Cornell, NY), the staff of the Edgerton Center Student Shop for assistance with building the electrospinning apparatus (MIT, Cambridge, MA), and Kerry Mahon for providing lab space and materials for electrospinning (Stemgent, Inc., Cambridge, MA). We thank Elizabeth Pritchard for writing assistance (Starnberg, Germany). This work was supported by The Faculty of Medicine, University of Lund, The Swedish Research Council, The Princess Margaretas Foundation for Blind Children, the Torsten and Ragnar Söderberg Foundation, the National Institutes of Health (Grants DE013023 and HL060435), and the Richard and Gail Siegal Gift Fund. C.D.P. was supported by the MIT/CIMIT Medical Engineering Fellowship. C.D.P. and P.B. were supported by a gift to MIT by InVivo Therapeutics Corporation. W.L.N. was supported by the NIH under Ruth L. Kirschstein National Research Service Award 1 F32 EY018285-01 from the National Eye Institute.

References

1. Ambati J, Ambati BK, Yoo SH, et al. Age-related macular degeneration: etiology, pathogenesis, and therapeutic strategies. Surv Ophthalmol 2003;48:257–93.

2. Berson EL, Rosner B, Sandberg MA, Weigel-DiFranco C, Moser A, Brockhurst RJ, et al. Further evaluation of docosahexaenoic acid in patients with retinitis pigmentosa receiving vitamin A treatment: subgroup analyses. Arch Ophthalmol 2004;122:1306–14.

3. Berson EL, Rosner B, Sandberg MA, Hayes KC, Nicholson BW, Weigel-DiFranco C, Willett W. A randomized trial of vitamin A and vitamin E supplementation for retinitis pigmentosa. Arch Ophthalmol 1993;111:761–72.

4. Acland GM, Aguirre GD, Bennett J, Aleman TS, Cideciyan AV, Bennicelli J, et al. Long-term restoration of rod and cone vision by single dose rAAV-mediated gene transfer to the retina in a canine model of childhood blindness. Mol Ther 2005;12:1072-82.

5. Turner JE and Blair JR. Newborn rat retinal cells transplanted into a retinal lesion site in adult host eyes. Brain Res 1986;391:91-104.

6. Ghosh F, Wong F, Johansson K, Bruun A, Petters RM. Transplantation of full-thickness retina in the rhodopsin transgenic pig. Retina 2004;24:98-109.

7. Maclaren RE, Pearson RA, Macneil A, Douglas RH, Salt TE, Akimoto M, et al. Retinal repair by transplantation of photoreceptor precursors. Nature 2006;444:203-7.

8. Ghosh F, Bruun A, Ehinger B. Graft-host connections in long-term full thickness embryonic rabbit retinal transplants. Invest Ophthalmol Vis Sci 1999;40:126-32.

9. Prince JH, Diesem DC, Eglitis I, Ruskell GL. The Pig Anatomy and Histology of the Eye and Orbit in Domestic Animals. Springfield: Charles C Thomas; 1960, p. 210-33.

10. Ghosh F, Neeley WL, Arnér K, Langer RS. Tissue Engineering Part A. -Not available-, ahead of print. doi:10.1089/ten.tea.2008.0450.

11. Wang Y, Ameer GA, Sheppard BJ, Langer RS. A tough biodegradable elastomer. Nat Biotechnol 2002;20:602-6.

12. Hersel U, Dahmen C, Kessler H. RGD modified polymers: biomaterials for stimulated cell adhesion and beyond. Biomaterials 2003;24:4385–4415.

13. Thanos C, Emerich D. Delivery of neurotrophic factors and therapeutic proteins for retinal diseases. Expert Opin Biol Ther 2005;5:1443–52.

14. Kleinman HK, McGarvey ML, Liotta LA, Robey PG, Tryggvason K, and Martin GR. Isolation and characterization of type IV procollagen, laminin and heparin sulfate proteoglycan from the EHS sarcoma. Biochemistry 1982;21:6188-93.

15. Neal RA, McClugage SG, Link MC, Sefcik LS, Ogle RC, and Botchwey EA. Laminin nanofiber meshes that mimic morphological properties and bioactivity of basement membranes. Tissue Eng Part C Methods 2009;15:11-21.

16. Corey JM, Lin DY, Mycek KB, Chen Q, Samuel S, Feldman EL, et al. Aligned electrospun nanofibers specify the direction of dorsal root ganglia neurite growth. J Biomed Mater Res A 2007;83:636-45.
17. Kim YT, Haftel VK, Kumar S, Bellamkonda RV. The role of aligned polymer fiber-based constructs in the bridging of long peripheral nerve gaps. Biomaterials 2008;29:3117-27.
18. Clements IP, Kim YT, English AW, Lu X, Chung A, Bellamkonda RV. Thin-film enhanced nerve guidance channels for peripheral nerve repair. Biomaterials 2009;30:3834-46.
19. Wen X, Tresco PA. Effect of filament diameter and extracellular matrix molecule precoating on neurite outgrowth and Schwann cell behavior on multifilament entubulation bridging device in vitro. J Biomed Mater Res A 2006;76:626-37.
20. Gerardo-Nava J, Führmann T, Klinkhammer K, Seiler N, Mey J, Klee D, et al. Human neural cell interactions with orientated electrospun nanofibers in vitro. Nanomed 2009;1:11-30.

V.

Retinal transplantation using surface modified poly(glycerol-co-sebacic acid) membranes.

Christopher D. Pritchard (1), Karin M. Arnér (2), Robert S. Langer (1), Fredrik K. Ghosh (2)

(1) Department of Chemical Engineering
Massachusetts Institute of Technology
Cambridge, MA 02139, USA

(2) Department of Ophthalmology
Lund University Hospital
S-22185 Lund, Sweden

Reprinted with permission from Elsevier: Biomaterials. 2010 Nov;31(31):7978-84.

Abstract

In retinal transplantation experiments it is hypothesized that remaining diseased photoreceptor cells in the host retina and inner retinal cells in transplants physically obstruct the development of graft-host neuronal contacts which are required for vision. Recently, we developed methods for the isolation of donor photoreceptor layers *in vitro*, and the selective removal of host photoreceptors *in vivo* using biodegradable elastomeric membranes composed of poly(glycerol-co-sebacic acid) (PGS). We also coated PGS membranes with electrospun nanofibers, composed of laminin and poly(epsilon-caprolactone) (PCL), to promote attachment of embryonic retinal explants, allowing the resulting composites to be handled surgically as a single entity. Here, we report subretinal transplantation of these composites into adult porcine eyes. In hematoxylin and eosin stained sections of composite explants after 5-7 days *in vitro,* excellent fusion of retinas and biomaterial membranes was noted, with the immature retinal components showing laminated as well as folded and rosetted areas. The composite grafts could be transplanted in all cases and, 3 months after surgery, eyes displayed clear media, attached retinas and the grafts located subretinally. Histological examination revealed that the biomaterial membrane had degraded without any signs of inflammation. Transplanted retinas displayed areas of rosettes as well as normal lamination. In most cases inner retinal layers were present in the grafts. Laminated areas displayed well developed photoreceptors adjacent to an intact host retinal pigment epithelium and degeneration of the host outer nuclear layer (ONL) was often observed together with occasional fusion of graft and host inner layers.

Introduction

Retinal transplantation experiments have the common goal of alleviating symptoms in patients suffering from retinal degeneration by replacing diseased photoreceptors with healthy cells. In the past two decades, a multitude of experimental approaches involving many different animal models have been explored but, to date, retinal transplantation is not available as a clinical treatment.

To transfer the retinal transplantation paradigm from the laboratory to the clinic, several key requirements must first be demonstrated. First, photoreceptors must survive the transplantation procedure and avoid rejection in the foreign host. Once in place, grafted cells have to organize properly and display structural properties as well as biochemical machinery compatible with phototransduction. Finally, the transduced signal must be transferred from the grafted cells to host neurons in a manner which allows visual perception.

Early protocols of retinal transplantation involved enzymatically and mechanically disrupted donor tissue in soluble form which, with comparatively little surgical effort, could be transferred to the confined subretinal space of the host eye. These experiments, as well as more recent ones built on the concept of cell-suspensions of retinal, progenitor or stem cells, have shown that disruption of the donor tissue may not be beneficial for graft survival, development, organization and integration [1-4].

To improve graft survival and organization, transplantation of non-disrupted tissue in the form of full-thickness retina has been explored by a few groups [5-8]. The rationale of the full-thickness paradigm is to limit antigen exposure to the host immune system, and retain the laminated organization of the donor retina with its delicate intrinsic microcircuitry. From experiments in large-eye animal models, the surgical procedure for full-thickness transplantation has been shown to be safe and relatively atraumatic to the eye in both normal and diseased eyes. Further, full-thickness grafts develop and retain morphologically normal photoreceptors for extended time periods in the foreign environment. In accordance with the initial hypothesis, these grafts elicit almost no immune response, as long as the graft is kept intact in both allogeneic as well as xenogeneic donor tissue paradigms [9-11].

The remaining issue that needs to be resolved pending clinical trials is the formation of functional connective neuronal networks so that transduced signals from grafted photoreceptors can be transferred to the host CNS. Graft-host neuronal connections have been demonstrated to some extent in the rabbit model [12-13] but not in the more relevant porcine one, in which integration of the two entities is hampered by the presence of remaining inner retinal cells in the transplant and remaining photoreceptors in the host [14]. To enhance the chance of useful integration of host and graft retina, these physical barriers should ideally be removed.

We have previously described the creation of a graft retina composed of isolated photoreceptors supported by Müller cells in an *in vitro* rodent model [15]. This was accomplished by separating immature full-thickness retinas from their inherent retinal circulation which, in combination with optic nerve transection, caused regression of inner retinal layer development. Next, we were able to remove photoreceptor cells from a defined area in adult rabbit eyes without damaging remaining inner retinal cells [16]. The photoreceptor cells are dependent on nutritive support from the choroid and, by implanting a 50 μm thick biodegradable PGS elastomer in the subretinal space of normal rabbits, selective outer retinal ischemia was accomplished. Implantation of the PGS membrane, however, did inflict damage on the retinal pigment epithelium. To limit the risk of this and other complications, transplantation of the neuroretinal tissue and implantation of the PGS membrane in the same session would be preferable. To this end, we constructed a composite graft consisting of an immature porcine full-thickness retina fused with a degradable PGS membrane [17]. We found that the PGS membranes coated with electrospun nanofibers adhered very well to the retina after 7 days of co-culture *in vitro*, and did not separate after placement and ejection from the transplantation instrument. The addition of the PGS membrane had no observed adverse effects on the developing donor tissue.

In the present study, we explore transplantation of the PGS-retina composite graft. We hypothesize that a graft composed of well-organized photoreceptors within a Müller glia cell scaffold fused with a biodegradable membrane will have an increased likelihood of recreating the complete retina with outer layers derived from the graft and inner retinal layers from the host (Fig. 1).

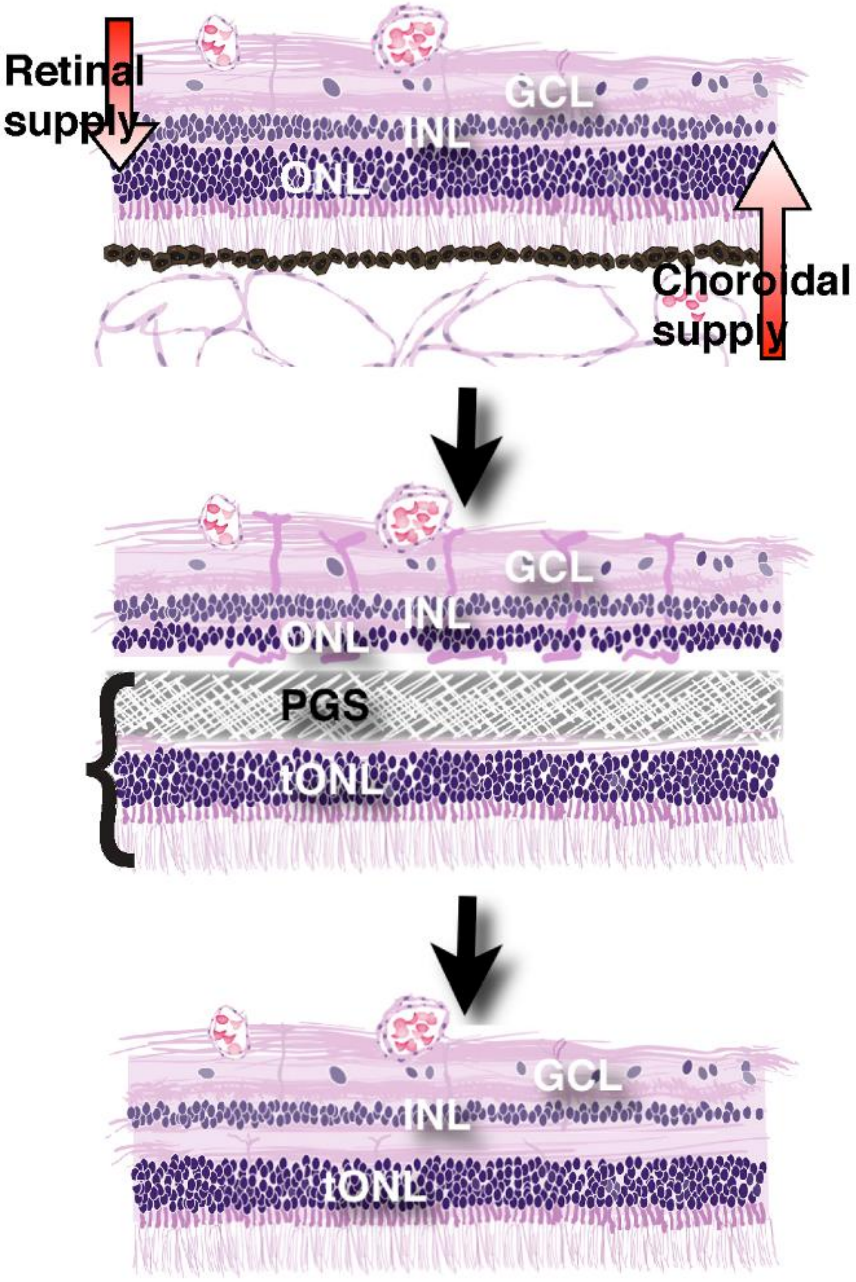

Figure 1. Illustration of the composite retinal graft model. **Top**: The *in vivo* host retina is dependent on a dual blood supply. The choroid supplies the photoreceptors in the outer nuclear layer (ONL) while the retinal vessels supply the inner retinal cells in the inner nuclear and ganglion cell layer (INL and GCL). **Middle**: When the composite graft, consisting of photoreceptors in a transplant outer nuclear layer (tONL) fused with a PGS membrane, is placed in the subretinal space, the membrane blocks the nutritive support to the host ONL which induces ischemia and removes host photoreceptors. **Bottom**: Following PGS membrane degradation, the remaining inner retina of the host integrates with the transplanted photoreceptors (tONL) creating a new retina with all normal layers.

Materials and methods

All compounds and solvents were obtained from Sigma-Aldrich, St. Louis, MO, USA, unless otherwise stated.

Preparation of poly(glycerol-co-sebacic acid) membranes

Poly(glycerol-co-sebacic acid) (PGS) branched polymer was prepared by poly-condensation as previously described [18]. Briefly, equimolar amounts (0.989 mol) of re-crystallized sebacic acid and anhydrous glycerol were charged to an oven-dried round bottom flask and reacted with stirring at 120°C under argon. After 21 hours, vacuum was applied and the mixture was reacted for another 64 hours. The resulting material formed a white wax at room temperature.

Cross-linking of the PGS to an elastomer was carried out in a class 10,000 clean room [19],[16]. A 10:1 prepolymer:hardener mixture of poly(dimethylsiloxane) (PDMS) (Sylgard 184, Dow Corning, Midland, MI) was degassed under vacuum and cured in a 10 cm Petri dish for 1 hour at 60°C. The resulting 10 cm diameter PDMS slab was plasma oxidized for 1 minute to create a hydrophilic surface. The top surface was spin coated at 3000 rpm for 30 seconds with a 61.5 wt. % aqueous sucrose solution (saturated at room temperature and 0.45 µm syringe filtered). The sucrose-coated PDMS was subsequently baked at 130 °C for 10 minutes and transferred to a hotplate at 120°C. Molten PGS wax (120 °C) was poured onto the sucrose-coated PDMS slab, covering the entire surface, and subsequently cured at 120 °C under a 15 millitorr vacuum until the PGS lost any adhesiveness to a stainless steel spatula.

Subsequently, the mold was submerged in 18 MOhm water overnight and the PGS was peeled from the PDMS underwater. The resultant PGS disk was approximately 3 mm thick.

The PGS disk was cut into 5 x 5 x 3 mm blocks, embedded in Tissue-Tek OCT compound (Sakura, Torrance, CA) and rapidly frozen by immersion in ethanol cooled with dry ice [17]. Frozen PGS was cryo-sectioned into 30 µm membranes at -30˚C with a Shur/Sharp Heavy Duty razor blade (TBS, Durham, NC). Thicker blades (0.5 mm or greater) and slow sectioning speeds were necessary to reduce vibration and warming of the blade from friction. Membrane thickness and uniformity was confirmed by scanning electron microscopy.

Fabrication of electrospun nanofibers

Nanofibers consisting of poly(epsilon-caprolactone) (PCL) laminin and a blend of 10 wt. % laminin in PCL of approximately 100 nanometers were electrospun onto 30 micron PGS sheets to create a bi-layer biomaterial membrane. Neuroretinal explants were subsequently placed on a culture membrane with the outer layers facing downward and the PGS-nanofiber membranes on top, with the nanofiber side of the PGS sheet placed onto the inner layers of the explant. Type 1 Laminin was isolated from murine Englebreth-Swarm-Holme tumor as previously described [20]. The laminin was provided as a gift by Stemgent, Inc. (Cambridge, MA). Electrospinning followed previously described protocols [21],[17]. For laminin nanofibers, lyophilized laminin was dissolved in 1,1,1,3,3,3-hexafluoro-2-propanol (HFP) at 3 w/v % at 4 °C overnight. The solution was then mounted into an Aladdin syringe pump (World Precision Instruments, Sarasota, FL) using a disposable syringe and a 18 gauge needle. PGS sheets mounted on glass cover slips were placed on the collector plate, and the laminin solution was dispensed at a flow rate of 1 mL/hr and driving voltage of 15 kV across a 15 cm vertical gap onto the grounded copper collector, and hence onto the PGS sheets. Samples were dried completely and stored in dessicant at -20 °C. Laminin-PCL blend nanofibers were electrospun in a similar manner. A solution consisting of 10 wt. % laminin and 90 wt. % PCL with 8 w/v % total polymer dissolved in HFP was used as the initial solution. The same procedure as for laminin was used to electrospin the blend onto PGS sheets, though the driving voltage was increased to 20 kV to compensate for the higher viscosity of this solution. 18 wt. % PCL was dissolved in 1:1 THF:DMF and electrospun at 20 kV in the same manner to fabricate PCL nanofibers.

Porcine tissue isolation

Eyes from Yorkshire/Hampshire pigs (gestational age of 114 days) were obtained from a local breeder (Lund, Sweden) and used for all experiments. Retinal tissue from E40 (40 days after conception) was used for culturing experiments. The pregnant sow was euthanized by means of captive bolt and incision of the carotid arteries. The fetuses were collected by caesarean section and euthanized by decapitation. Both eyes were enucleated and immediately immersed in ice-cold CO2-independent medium. The neuroretinas were carefully dissected free from the retinal pigment epithelium (RPE) and hyaloid vascular system with fine forceps. The optic nerve was thereafter cut with micro-scissors and neuroretinal pieces measuring approximately 3x4 mm were explanted on Millicell®-HA 0.45- µm culture plate inserts with the photoreceptor layer towards the membrane. All neuroretinas were put in culture within 240 minutes of euthanasia. Explants were cultured in 1.2 mL Gibco D-MEM F12 medium –L-Glutamine (Gibco, Paisley, UK) supplemented with 10 vol. % fetal calf serum. A cocktail containing 2 mM L-glutamine, 100 U/mL penicillin and 100 ng/mL streptomycin was added and the retinas were maintained at 37 °C with 95 % humidity and 5 % CO2.

All proceedings and treatment of animals were in accordance with the guidelines and requirements of the Government Committee on Animal Experimentation at Lund University and with the ARVO Statement for the Use of Animals in Ophthalmic and Vision Research.

Co-culture of retinal layers with biomaterial membranes

After two days *in vitro*, PCL-PGS and Laminin-PCL-PGS membranes measuring 3x4 mm were added to the explanted retinal specimens, while remaining pieces were kept in culture without the addition of a membrane as controls. At this time, half of the culture medium was exchanged, and this procedure was then repeated every second day. The composite explants were kept for 5-7 days *in vitro*. At the end of the culture period, the PGS membrane had attached firmly to the neuroretina.

To establish the fate of the composite explants prior to transplantation, neuroretinal explants with and without PGS membranes were fixed and prepared for histology at the end of the culture period. For these experiments, culture plate inserts were fixed in 4% paraformaldehyde in 0.1 M phosphate buffer (PB), pH 7.2, for 4 h at 4°C. Several rinses in PB followed, and then the specimens were infiltrated with 0.1 M PB containing sucrose in increasing concentrations, and finally embedded for cryosectioning. After serial sectioning on a cryostat, every 10th slide was stained with hematoxylin and eosin. Photographs were obtained with a digital camera system (Olympus, Tokyo, Japan) and were adjusted for brightness and contrast digitally.

Surgery

Twelve normal Yorkshire/Hampshire pigs, aged 3 months were used as hosts and received one PGS-retina composite graft in the right eye (PCL-PGS n=5, and Laminin-PCL-PGS n=7). The surgical procedure for full-thickness transplantation has been described in detail in previous articles [14]. In summary, a two-port central vitrectomy, including a posterior vitreous detachment, was performed, after which a local retinal bleb was created in a vessel-free area 2–3 mm superior and nasal to the optic nerve by infusing Ames´ medium subretinally (Fig. 2). A second retinotomy was then made to provide a valve. The compound graft, consisting of PGS membrane and neuroretina was transferred from the culture system to an embryonic cryodish filled with Ames´ solution. The Ames´ solution was exchanged several times, to ensure that no culture medium remained with the explants. The graft was drawn into a polyethylene tube (Becton Dickinson and company, MD, USA) attached to a syringe filled with Ames´ solution. The polyethylene tube had an original inner diameter of 1.4 mm and an outer diameter of 1.9 mm, and was flattened mechanically to accommodate the flat PGS-retina graft. The tube was introduced into the eye, and advanced until its tip was adjacent to the first retinotomy. The graft was then eased out, into the subretinal space. Eyes from the first and second day of surgery received a 3x4 mm graft, and in these eyes, some bleeding from the retinotomy was evident. On the second day of surgery, smaller (2x3 mm) grafts were used which reduced the incidence of retinal hemorrhage.

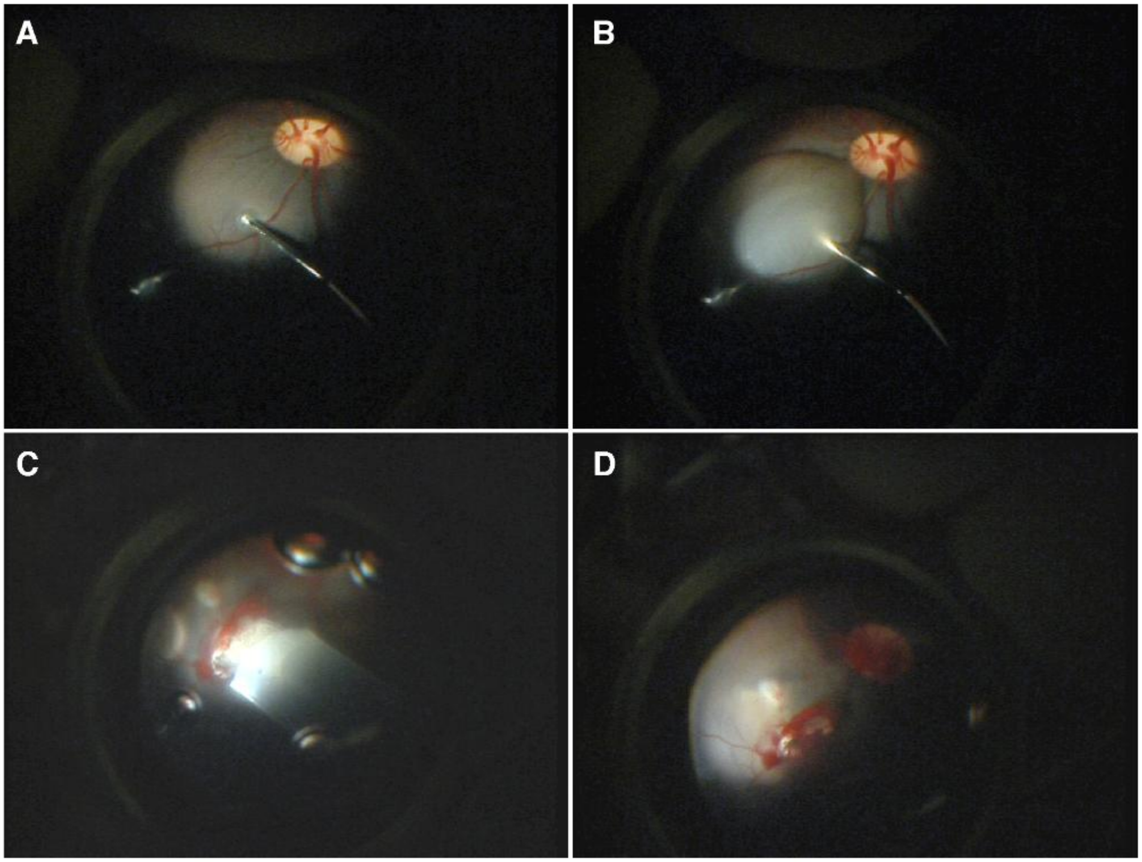

Figure 2. Intra-operative photographs, demonstrating the formation of a subretinal bleb (**A** and **B**) and introduction of the graft into the subretinal space (**C** and **D**).

Postoperative management and follow-up

No postoperative treatment was given. Eyes were examined externally daily for the first week. An ophthalmoscopic examination was performed on one occasion, 4-6 days postoperatively. At the end of the follow-up period, animals were euthanized by means of captive bolt and incision of the carotid arteries. The eyes were enucleated, a cut made at the pars plana, and the eyes were fixed in 4% paraformaldehyde in 0.1 M PB, pH 7.2, for 30 minutes. The anterior segment was then removed and the posterior eyecup was fixed in the same solution for 4 hours. After fixation, the specimens were handled in the same way as the explants fixed directly after culture (see above).

All procedures and animal treatment were in accordance with the guidelines and requirements of the Government Committee on Animal Experimentation at Lund University and with the ARVO Statement for the Use of Animals in Ophthalmic and Vision Research.

Results

Macroscopic findings

At ophthalmoscopic examination, most eyes displayed clear media with the graft placed flat in the subretinal space. One pig showed signs of infection (blepharitis and slight opacification of the cornea) and was terminated 5 days postoperatively. At dissection, the interior of this eye was clear, and the graft was found in place in the subretinal space. Remaining eyes were followed for 3 months. At dissection, these eyes displayed clear media, an attached retina with no signs of inflammation. In most cases, the graft was visible in the subretinal space as a rectangular gray tissue (Fig. 3).

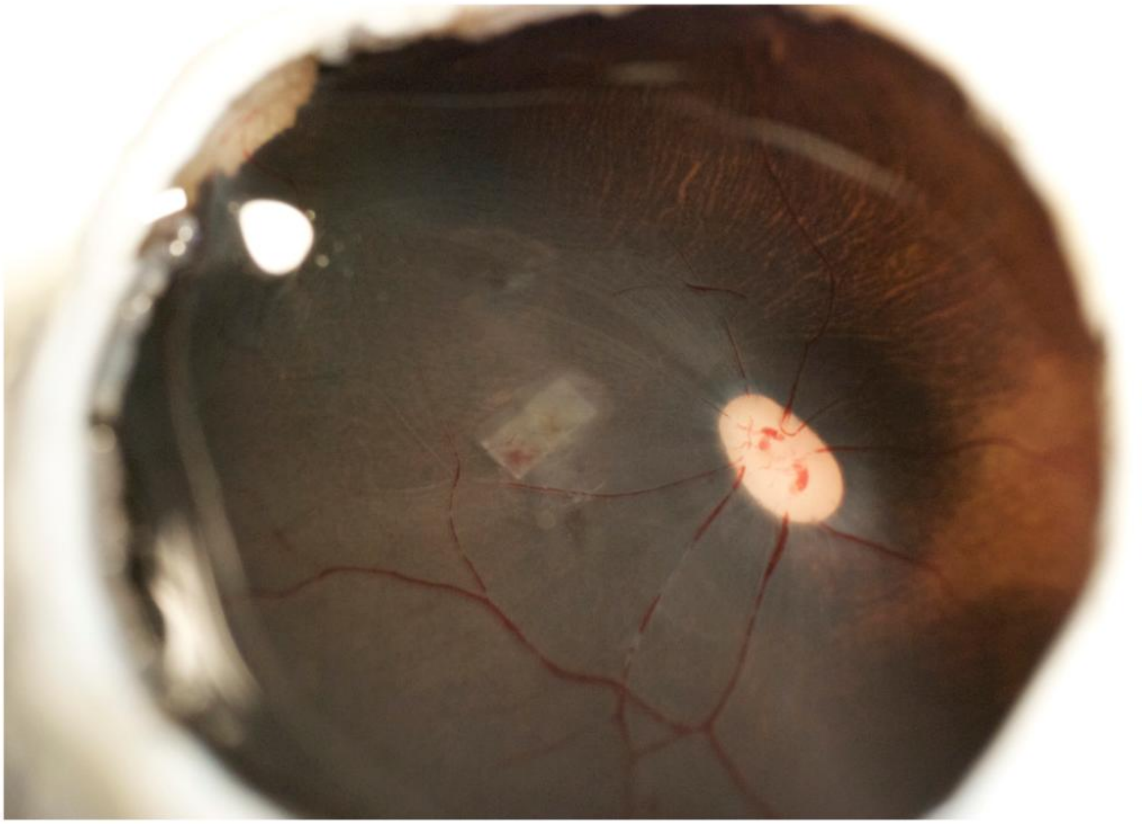

Figure 3. Dissected eyecup 3 months after transplantation of a PGS-Retina explant. The graft is present as a gray rectangular shape under the folded host retina.

Histology

PGS-retina explants

In hematoxylin and eosin stained sections, explants cultured for a total of 7-9 days displayed areas of laminated retina as well as areas with folded retina and rosettes (Fig. 4). Retinal explants without addition of PGS membrane (n=7) displayed minimal folding/rosettes in one case, mixed rosettes and lamination in 4 cases, and in 2 cases mostly rosettes. Laminin-PCL-PGS explants (n=5) displayed minimal folding/rosettes in 2 cases, mixed rosettes and lamination in one case, and in 2 cases mostly rosettes. PCL-PGS explants (n=6) had minimal folding/rosettes in 3 cases, mixed rosettes and lamination in 2 cases, and in one case mostly rosettes. Laminated areas of explants without PGS membrane displayed a neuroblastic cell layer (NBL) consisting of multiple rows of undifferentiated cells, a thin inner plexiform layer (IPL), a ganglion cell layer (GCL) with one row of cells and a nerve fiber layer (NFL) in the innermost part (Fig.4A). In composite explants, the PGS membrane could be seen well-attached to the inner surface of the immature neuroretina (Fig. 4C-E). Laminated areas were thinner compared to specimens without PGS membrane and consisted of a NBL, a thin IPL and GCL and no discernible NFL (Fig. 4D).

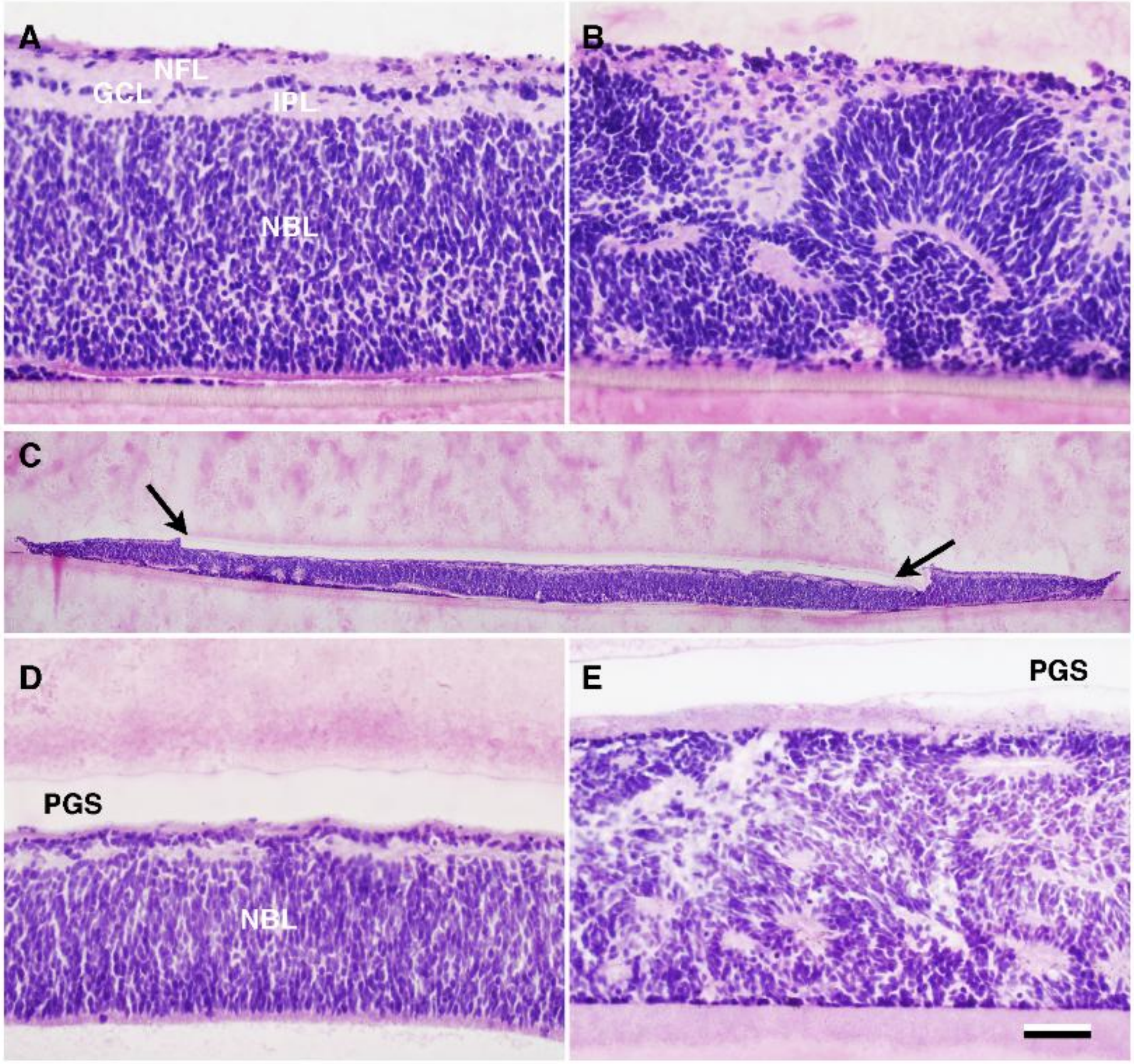

Figure 4. Donor tissue after 7-9 days *in vitro*. Hematoxylin and eosin staining. **A** - **B**: E40 neuroretinal explants without addition of PGS membrane. In **A**, a well laminated explant is seen with a neuroblastic cell layer (NBL) consisting of multiple rows of undifferentiated cells, a thin inner plexiform layer (IPL), a ganglion cell layer (GCL) with 1 row of cells and a nerve fiber layer NFL in the innermost part. In **B** severe folding of the retinal architecture is seen in another explant.

C - **E**: PGS-Retina explants: In **C**, the full extent of the composite explant with the Laminin-PCL-PGS membrane (between arrows) attached to the inner retina can be seen. **D**: Detail. The explanted retina displays a NBL and rudimentary inner layers. **E**: Rosetted explant without any apparent lamination.

Scale bar = 50 µm (**A**-**B** and **D**-**E**) and 500 µm (**C**)

Transplanted eyes

In hematoxylin and eosin stained sections, the one eye with a PCL-PGS composite graft terminated on postoperative day 5 displayed the graft upside down in the subretinal space, with the membrane adjacent to the host retinal pigment epithelium (RPE), and the grafted neuroretina severely degenerated (Fig. 5A). The host retina had an epiretinal hemorrhage in the transplantation area and the outer nuclear layer (ONL) was thinner than normal.

In transplanted eyes 3 months postoperatively, grafts were found in all 11 eyes which had received a PGS-retina composite graft (Fig. 5B-E). Eyes with Laminin-PCL-PGS composite grafts (n=7) displayed a laminated retina with minimal folding/rosettes in one case, mixed rosettes and lamination in 2 cases and mostly rosettes in 4 cases. Eyes with PCL-PGS composite grafts (n=4) displayed a laminated retina with minimal folding/rosettes in one case, with the remaining 3 consisting mostly of rosettes. Laminated areas of 3-month composite grafts displayed outer segments apposed to the host RPE, inner segments, a well developed ONL, an outer plexiform layer (OPL), INL, thin IPL and cells with small perikarya in the GCL. The host RPE was found to be continuous in all areas where a laminated graft was found. In rosetted areas, the RPE was occasionally discontinuous, and in one case, an invasion of cells from the choroid was evident. No other signs of inflammation were seen. The host retina appeared normal in all eyes, except for the part covering the transplant. Here, the photoreceptors in the ONL had degenerated to varying degrees. In some sections no ONL was found, while in others 3 to 4 rows of cells without outer segments remained. The inner retinal layers were preserved in most cases but occasionally disruption of the INL was evident. The PGS membrane could not be identified in any 3-month specimen. However, between graft and host, especially in areas of rosette formation, yellowish deposits were found in 5 specimens (4 Lam-PCL-PGS and 1 PCL-PGS), and reddish material in one case, suggestive of remnants of foreign material possibly derived from the degraded biomaterial membrane (Fig. 5D-E). Occasionally fusion of graft and host retina was seen and the innermost layers of the graft had integrated with the host INL.

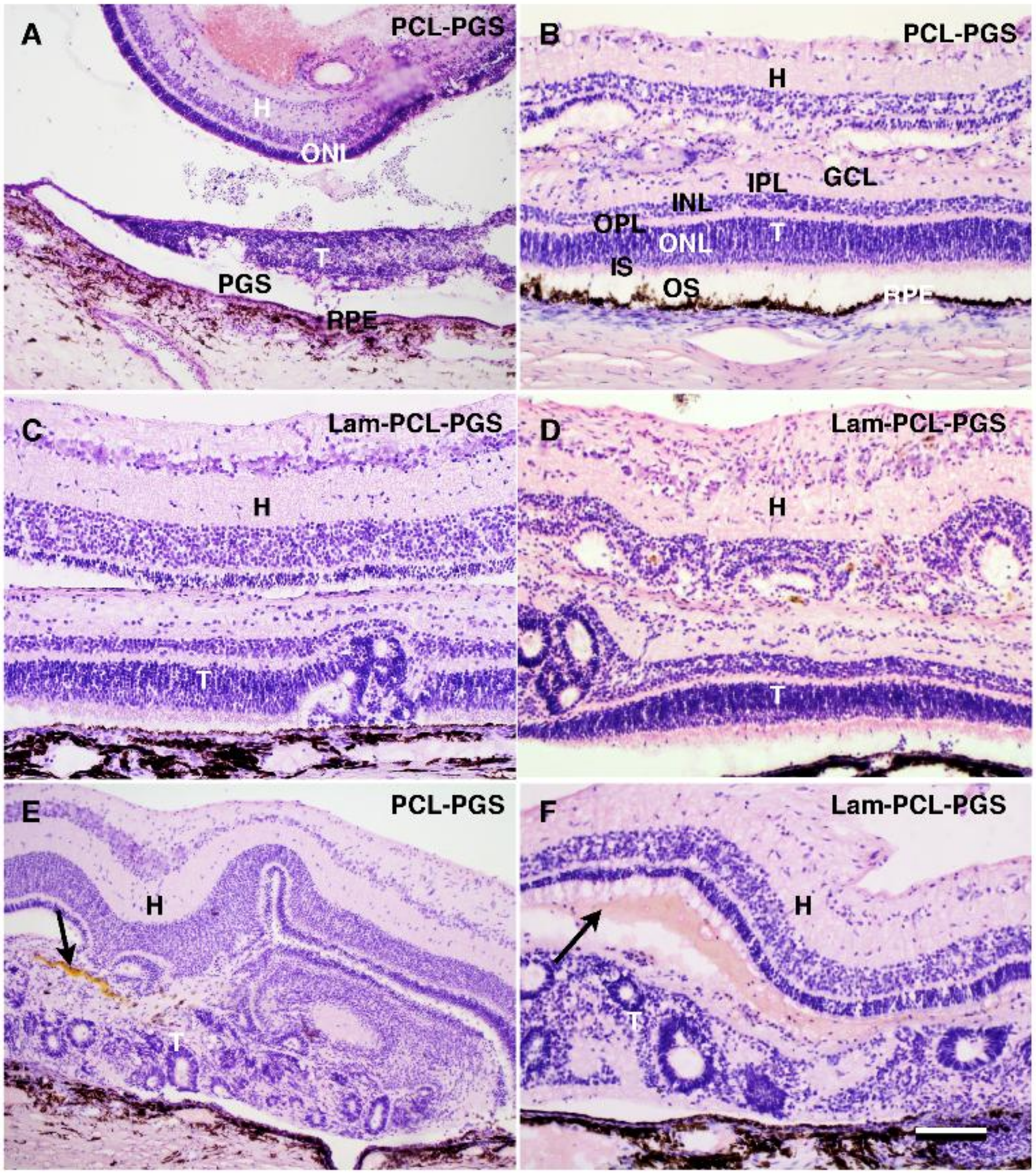

Figure 5. PGS-Retina transplants. Hematoxylin and eosin staining. **A**: PCL-PGS composite graft 5 days postoperatively. The transplant (T) is upside down in the subretinal space with the membrane (PGS) adjacent to the host Retinal Pigment Epithelium (RPE). The grafted neuroretina in severely degenerated. The host retina (H) has an epiretinal hemorrhage and the outer nuclear (ONL) is thinner than normal. **B** - **D**: 3-month transplants (T). **B** - **D** shows laminated areas where the graft consists of outer segments (OS) apposed to the host retinal pigment epithelium (RPE), inner segments (IS), outer nuclear layer (ONL), outer plexiform layer (OPL), inner nuclear layer (INL), inner plexiform layer (IPL), and cells with small perikarya in the ganglion cell layer (GCL). In the host retina (H), the ONL is absent in **B** and **D** and severely

reduced in **C**. Fusion of the graft with the inner nuclear layer is evident in **B** and **D** while the two entities remain separate in **C**. **E** and **F** shows rosetted transplants areas with yellowish and reddish material between the host and graft (arrows).
Scale bar = 200 µm (**A**), and 100 µm (**B** - **F**).

Discussion

Surgical considerations

In the present paper we have explored the concept of retinal transplantation in combination with a degradable membrane for the purpose of enhancing graft-host neuronal integration. Eyes transplanted with the PGS-retina graft fared well postoperatively, displaying clear media, attached retina, and the graft securely in place in the subretinal space, suggesting that the surgical procedure for composite graft transplantation works efficiently.

Transplantation of full-thickness retina has been reported in several animal models previously [6-8],[14]. In earlier work in pig and rabbit eyes, we used a siliconized glass cannula for transplantation in which the elastic retinal graft adopted a rolled-up shape. This allowed us to use a relatively small sclerotomy and retinotomy. In the present study, the added PGS membrane made the composite graft less flexible, requiring a different approach using a wider device in which the graft could be kept flat. This, in turn, necessitated a wider sclerotomy and retinotomy, which was associated with some degree of retinal hemorrhage. We are currently developing a more flexible biomaterial membrane, with a lower elastic modulus, to reduce the risk of complications. This may be accomplished by changing the curing time of PGS to reduce the degree of cross-linking, or the selection of different monomer precursors [22-23].

Transplanted retina

Surviving grafts were found in all transplanted eyes confirming the low degree of antigenicity of full-thickness retina. This also suggests that the addition of PGS membrane does not provoke immune rejection. Laminated areas of the grafts displayed well-developed photoreceptors organized in an outer nuclear layer comparable in size to the one found in the normal adult porcine retina. However, somewhat surprisingly, inner layers also developed and were retained, which hampered neuronal contacts between grafted photoreceptors and the host inner retina. In a previously published paper where E45-E50 porcine retina cultures were explored, we found that addition of PGS membrane drastically suppressed inner retinal cell development while photoreceptors were unaffected [17]. Except for the use of E40 instead of E45-50 porcine retina, the same culturing protocol as in our previous work was used in the present work. In spite of several steps which should theoretically ensure photoreceptor isolation (optic nerve transection, separation from the developing retinal circulation, and placement of PGS membrane on the inner part of the explants), inner layers were observed consistently in transplanted eyes. Cell type differentiation in the porcine retina commences at approximately E39-40 with a large population of cells still retained in an undifferentiated state [24]. The relative immaturity of the E40 specimens may thus account for a seemingly normal inner retinal development in spite of the culturing process. The results suggest that, to obtain photoreceptor isolation in the graft, more mature donor tissue should be used.

The PGS-retina composite grafts all displayed areas of rosette formation. Rosettes are an abnormal form of retinal development where the retina forms folds and then rolls of retinal tissue. The phenomenon has been attributed to abnormal development, and is not seen in the adult retina, even after trauma [25]. The exact origin of rosettes has not been established but they were first described in tumors (retinoblastoma) and later in retinal cultures, as well as in fragmented retinal transplants. Rosettes have been described in full-thickness retinal transplants but, in our previous work, laminated areas have invariably dominated the more atypical rosetted architecture [14]. Photoreceptors in rosettes display short or absent outer segments due to lack of proper contact with the RPE. In addition, visual processing in the retina is completely dependent on a precise organization of the retinal subtypes for transduction, as well as visual processing, and it is unlikely for rosetted grafts to result in functional restoration of vision. A strong association between Müller cell trauma and rosette formation in the developing retina has been postulated [25]. In the present work, the E40 retinal explants with or without added PGS membrane displayed a considerable degree of folding and rosette formation, indicating that the culturing procedure prior to transplantation induces abnormal retinal development. In our previous paper on E45-E50 porcine retina cultures, we found only minimal folding [17]. Further, the addition of PGS membrane attenuated this phenomenon. As mentioned above, E39-40 is a critical time-point in porcine retinal development and it is possible that disturbance of early cell type differentiation disrupts retinal lamination [24]. Again, this indicates that the use of more mature donor tissue may be favorable.

Host retina

One of the main aims of the present work was to eliminate host photoreceptors without disturbing the inner retinal architecture. In all specimens, the ONL was reduced in the part straddling the transplant and, in some areas, it was completely missing while inner retinas were generally well-preserved. The reduction of ONL was more prominent compared with our earlier work involving transplantation of full-thickness retinas into porcine eyes. This suggests that the PGS-membrane contributed to host photoreceptor death [14]. However, the host ONL was still present in some areas, indicating that a membrane with a longer degradation time may be even more effective. This may be accomplished by the selection of different monomer precursors with altered hydrophobicity in order to reduce the rate of hydrolysis of ester bonds in the elastomer [22-23].

Conclusion

We show that a composite graft composed of retinal tissue fused with a PGS membrane can be transplanted into an adult porcine eye with minimal complications. The PGS component of the graft degrades without signs of inflammation after inducing selective elimination of host photoreceptors. The remaining grafted retina survives well but often displays an atypical retinal architecture in the form of rosettes which can already be observed prior to transplantation *in vitro*. In spite of the culturing procedure, inner retinal layers develop and persist in laminated areas of the graft which hampers proper integration of graft photoreceptors with the remaining inner retina of the host. Future work will be directed towards optimization of graft retinal architecture prior to transplantation.

Acknowledgements

We thank Kurt Broderick for assistance with clean room operation (MTL, MIT, Cambridge, MA), Nikki Watson assistance with cryo-sectioning (Whitehead Institute, Cambridge, MA), Rebekah Neal for electrospinning (University of Virginia, Charlottesville, VA), and Kerry Mahon for providing lab space and materials for electrospinning (Stemgent, Inc., Cambridge, MA). We thank Elizabeth Pritchard for writing assistance (Starnberg, Germany). This work was supported by The Faculty of Medicine, University of Lund, The Swedish Research Council, The Princess Margaretas Foundation for Blind Children, the Torsten and Ragnar Söderberg Foundation, the National Institutes of Health (Grants DE013023 and HL060435), and the Richard and Gail Siegal Gift Fund. C.D.P. was supported by a MIT/CIMIT Medical Engineering Fellowship and a gift to MIT by InVivo Therapeutics Corporation.

References

1. Turner JE, Blair JR. Newborn rat retinal cells transplanted into a retinal lesion site in adult host eyes. Brain Res 1986;391:91-104.
2. Juliusson B, Bergström A, van Veen T, Ehinger B. Cellular organization in retinal transplants using cell suspensions or fragments of embryonic retinal tissue. Cell Transplant 1993;2:411–8.
3. MacLaren RE, Pearson RA, MacNeil A, Douglas RH, Salt TE, Akimoto M, et al. Retinal repair by transplantation of photoreceptor precursors. Nature 2006;444:203-7.
4. Canola K, Angénieux B, Tekaya M, Quiambao A, Naash MI, Munier FL, et al. Retinal Stem Cells Transplanted into Models of Late Stages of Retinitis Pigmentosa Preferentially Adopt a Glial or a Retinal Ganglion Cell Fate. Invest Ophthalmol Vis Sci. 200;48(1):446-54.
5. Schuschereba ST, Silverman MS. Retinal cell and photoreceptor transplantation between adult New Zealand Red rabbit retinas. Exp Neurol 1992;115(1):95-9.
6. Ghosh F, Arnér K, Ehinger B. Transplant of full-thickness embryonic rabbit retina using pars plana vitrectomy. Retina 1998;18:136-42.
7. Seiler MJ, Aramant RB. Intact sheets of fetal retina transplanted to restore damaged rat retinas. Invest Ophthalmol Vis Sci 1998;39(11):2121-31.
8. Seiler MJ, Aramant RB, Seeliger MW, Bragadottir R, Mahoney M, Narfström K. Functional and structural assessment of retinal sheet allograft transplantation in feline hereditary retinal degeneration. Vet Ophthalmol 2009;12:158-69.
9. Wassélius J, Ghosh F. Adult rabbit retinal transplants. Invest Ophthalmol Vis Sci 2001;42:2632-8.
10. Engelsberg, K, Ghosh, F. Transplantation of Cultured Adult Porcine Full-Thickness Retina. Cell Transplant 2007;16(1):31-9.
11. Ghosh F, Rauer O, Arnér K. Neuroretinal xenotransplantation to immunocompetent hosts in a discordant species combination. Neuroscience 2008;152:526-33.
12. Ghosh F, Bruun A, Ehinger B. Graft-host connections in long-term full thickness embryonic rabbit retinal transplants. Invest Ophthalmol Vis Sci 1999;40:126-32.
13. Ghosh F, Johansson K, Ehinger B. Long-term full-thickness embryonic rabbit retinal transplants. Invest Ophthalmol Vis Sci 1999;40:133-40.
14. Ghosh, F.; Arnér, K. Transplantation of full-thickness retina in the normal porcine eye: Surgical and morphologic aspects. Retina 2002; 22:478–486.
15. Ghosh, F, Arnér, K, and Engelsberg, K. Isolation of photoreceptors in the cultured full-thickness fetal rat retina. Invest Ophthalmol Vis Sci 2009;50:826-35.
16. Ghosh F, Neeley WL, Arnér K, Langer R. Selective Removal of Photoreceptor Cells *In Vivo* Using the Biodegradable Elastomer Poly(Glycerol Sebacate). Tissue Eng Part A. -Not available-, ahead of print. doi:10.1089/ten.tea.2008.0450.

17. Pritchard CD, Arnér KM, Neal RA, Neeley WL, Bojo P, Bachelder E, et al. The use of surface modified poly(glycerol-co-sebacic acid) in retinal transplantation. Biomaterials 2010;31(8):2153-62.
18. Wang Y, Ameer GA, Sheppard BJ, Langer RS. A tough biodegradable elastomer. Nat Biotechnol 2002;20:602-6.
19. Neeley WL, Redenti S, Klassen H, Tao S, Desai T, Young MJ et al. A microfabricated scaffold for retinal progenitor cell grafting. Biomaterials 2008;29(4):418-26.
20. Kleinman HK, McGarvey ML, Liotta LA, Robey PG, Tryggvason K, Martin GR. Isolation and characterization of type IV procollagen, laminin and heparin sulfate proteoglycan from the EHS sarcoma. Biochemistry 1982;21:6188-93.
21. Neal RA, McClugage SG, Link MC, Sefcik LS, Ogle RC, Botchwey EA. Laminin nanofiber meshes that mimic morphological properties and bioactivity of basement membranes. Tissue Eng Part C Methods 2009;15:11-21.
22. Bettinger CJ, Bruggeman JP, Borenstein JT, Langer RS. Amino alcohol-based degradable poly(ester amide) elastomers. Biomaterials 2008;29(15):2315-25.
23. Bruggeman JP, de Bruin BJ, Bettinger CJ, Langer R. Biodegradable poly(polyol sebacate) polymers. Biomaterials 2008;29(36):4726-35.
24. Ghosh F and Arnér K. Cell type differentiation dynamics in the developing porcine retina. Dev Neurosci. 2010;32:47-58.
25. Ghosh F, Juliusson B, Arnér K, Ehinger B. Partial and Full-Thickness Neuroretinal Transplants. Exp Eye Res 1999;68:67-74.

VI.

Evaluation of viscoelastic poly(ethylene glycol) sols as vitreous substitutes

Christopher D. Pritchard (1), Sven Crafoord (3), Sten Andréasson (2), Karin M. Arnér (2),
Timothy M. O'Shea (1), Robert Langer (1), Fredrik K. Ghosh (2)

(7) Department of Chemical Engineering
Massachusetts Institute of Technology
Cambridge, MA 02139, USA

(8) Department of Opthalmology
Lund University Hospital
Lund SE 22184, Sweden

(9) Department of Opthalmology
Örebro University Hospital
Örebro SE 70185, Sweden

Reprinted with permission from Elsevier: Acta Biomateralia. 2011 Mar;7(3):936-43.

Abstract

The aim of this study was to employ an experimental protocol for in vivo evaluation of sols of 5 wt.% poly(ethylene glycol) (PEG) in phosphate buffered saline (PBS) as artificial vitreous substitutes. A 20 gauge pars plana vitrectomy and posterior vitreous detachment were performed in the right eye of 8 pigmented rabbits. Approximately 1 mL of the viscoelastic PEG sols were then injected into the vitreous space of 6 eyes. PEG with an average molecular weight of 300,000 g mol^{-1} and 400,000 g mol^{-1} was used in 2 and 4 eyes respectively. 2 eyes received balanced salt soultion (BSS) and served as controls. Full-field electroretinography (ERG) and intraocular pressure (IOP, palpation) was measured pre-and post-operatively at regular intervals up to 41 days. The rabbits were sacrificed and the eyes were examined by retinal photography, gross macroscopic examination and histology. The viscoelastic sols were successfully injected and remained translucent throughout the postoperative period, with some inferior formation of precipitates. None of the eyes displayed IOP elevation postoperatively, but in 3 of the PEG sol injected eyes, transient hypotony was noted. One eye sustained a retinal detachment during surgery and another 2 in the postoperative period. ERG recordings confirmed preservation of retinal function in 3 out of 4 eyes injected with 400,000 g mol^{-1} PEG. Histological examination revealed upregulation of glial acidic fibrillary protein (GFAP) in Müller cells in PEG sol injected eyes, but normal overall morphology in eyes with attached retinas. The viscosity of the sol was not retained throughout the postoperative period, indicating the demand for polymer crosslinking to increase residence time. The results provide promising preliminary results of the use of PEG hydrogels as a vitreous substitute.

Introduction

Synthetic vitreous replacement is an important part of vitreoretinal surgery, for use as a tamponade in retinal detachment, diabetic retinopathy, trauma or possibly as a depot for long-term drug delivery. Currently gases, perfluorocarbon liquids or silicone oil are most predominately applied clinically to separate water from the retinal rupture to prevent subretinal fluid accumulation leading to further retinal detachment. However, these agents have several disadvantages, including cataracts and elevation of intraocular pressure (IOP), and they are unsuitable as long term vitreous substitutes [1-2]. The vitreous is a hydrogel composed of collagen and hyaluronic acid, with reported values of 98-99% water. pH 7.0-7.4, with and elastic modulus of 4.2-4.7 Pa and a loss modulus of 1.9-3.7 Pa and a refractive index of 1.3345-1.3348 [3]. Synthetic hydrogels are a promising form of vitreous substitute that could tamponade water influx through a rupture and simultaneously provide a normal vitreous biochemistry. Material requirements include optical translucence and homogeneity, atoxicity and physiological isotonicity. The material must also permit transport of salts, nutrients and water and be stable to enzymatic or hydrolytic degradation as well as being immunologically inert. In addition, it should be able to be administrated through a 20 gauge needle without inducing structural damage to the gel. Therefore, an injectable hydrogel that cross-links *in situ* is theoretically an ideal solution. A wide variety of synthetic polymers, in solution or as cross-linked hydrogels, have been tested experimentally and shown to satisfy a wide range of necessary properties. However, to date, no material has been successfully translated for clinical use that can meet all desired properties for an ideal vitreous substitute [4-15].Problems have included gel fragmentation, opacification, retinotoxicity and IOP elevation. In a prior study, a polymer using in reconstructive surgery, poly(alkyl-imide) (Bio-Alcamid™), was tested as a potential substitute

[16-17]. However, this material caused central retinal edema one day after surgery, accompanied by pathological electroretinography (ERG) [18]. Poly(ethylene glycol) (PEG) is a synthetic water soluble polymer that has been FDA approved for use in a wide range of biomedical applications, including injectable hydrogels [19]. It has also been tested in formulations for intravitreal drug delivery, repair of scleral incisions and sealing retinal detachments [20-22]. In this study, we investigated the injection of viscoelastic sols of high molecular weight (> 200 kDa) PEG in phosphate buffered saline (PBS) into the vitreous bodies of rabbit eyes following vitrectomy. The molecular weights and concentration of PEG were chosen to approximate the mechanical properties of the natural vitreous. The aim of the study was to ascertain whether the PEG sols preserve normal intraocular pressure (IOP), retinal function and attachment as vitreous substitutes after experimental vitrectomy.

Materials and methods

Characterization of PEG sols

Sols of 5 wt.% poly(ethylene glycol) (PEG, Sigma Aldrich, St. Louis, MO) were prepared in sterile phosphate buffered saline (PBS, pH 7.4, Invitrogen, Carlsbad, CA), with molecular weights of 200, 300 and 400 kDa. The sols are referred to as S200, S300 and S400 respectively in subsequent sections. pH was measured using a digital pH probe (Russell RL060P, Thermo Scientific, Waltham, MA). Dynamic rheology was performed using an AR G-2 with a 40 mm diameter 2° cone and plate set-up (TA Instruments, New Castle, DE) at 10 rad s^{-1} oscillation and 5 % strain. Refractive indices were measured using a handheld Brix refractometer (PAL-1, Atago, Tokyo, Japan). Sols were sterilized by ultraviolet irradiation for 12 hours prior to surgery.

Animal selection and study protocol

The study was approved by The Regional Ethics Committee for Animal Experiments in Lund and it also conformed to the ARVO Resolution on the Use of Animals in Vision and Ophthalmic Research.

Eight pigmented rabbits, aged 4 months were used in the experiment. The right eye was operated upon and injected with 0.8-1 mL solutions following vitrectomy (3 with S300, 3 with with S400, 2 with balanced salt solution (BSS)) while the left eye served as a control. Examination including ophthalmoscopy and IOP measurement (palpation) was performed at postoperative day 6, 20 and 41. The rabbits were sacrificed at day 41, at which time the eyes were gross examined, photographed and prepared for histological examination with routine microscopy.

Surgery

All procedures were performed by clinically well experienced vitreoretinal surgeons. General anesthesia was provided with a combination of ketamine (35 mg/kg) and xylazine (5 mg/kg) intramuscularly. The right eye was instilled with cyclopentolate (1%) and phenylephrine (10%) 30 minutes before surgery. Topical tetracaine (0.5%) was applied just before surgery. The conjunctiva was incised limbally 270° from 9 to 6 o'clock with a vertical incision at 12 o'clock, creating two flaps. A 20G infusion cannula was sutured to the sclera in the 4 o'clock position 1 mm posterior to the limbus and a balanced salt solution (BSS, Endosol, Allergan Medical Optics) was started. Two 20G sclerotomies were made in the 10 and 2 o'clock positions. A BIOM 90-D lens (Oculus) was used to visualize the fundus, and an Accurus surgical system machine (Alcon, Fort Worth, TX) was used for surgery. A standard endo-illuminating light probe (Alcon) was introduced through the 10 o'clock sclerotomy (illumination level 80%), and a vitreous cutter (Innovit, Alcon) was inserted through the 2 o'clock sclerotomy. Posterior vitreous detachment (PVD) was created by positioning the vitrectomy probe at the margin of the disk and applying suction (100 mmHg) while pulling on the probe. PVD was confirmed visually as the posterior vitreous cortex separated from the posterior pole. All vitreous in the central fundus (approximately 50% of the total volume) was removed while peripheral parts were left because of the risk of instrument touch to the comparatively large lens. In one case (#1 S300) a retinal touch with the vitrector occurred causing a retinal rupture and anterior chamber bleeding. After vitreous removal, a fluid-air exchange was performed after which PEG sol was injected under visual control through a 19 gauge needle. The amount of sol injected varied from 0.8 to 1.5 mL (Table 2). In one case, there was backflow during gel injection and a volume of 1.5 mL sol was administered (#6 S400). The sclerotomies and conjunctiva were sutured and 25 mg gentamicin and 2 mg betamethasone were injected subconjunctivally. No postoperative treatment was given. The eyes were examined externally daily and with an external ophthalmoscope at days 6 and 20. Images of the retinas were taken at day 20 (RetCam, Clarity Medical Systems, Pleasanton, CA). Two eyes, used as controls, underwent the above surgery but were injected with balanced salt solution (BSS) instead of PEG sol.

Full-Field ERG

A standardized full-field electroretinography (ERG) was recorded 7 days before surgery and 41 days postoperatively on the right eye using a Nicolet Viking analysis system (Nicolet Biomedical Instruments, Madison Wisconsin) as previously described [23]. During examination the rabbits were sedated with Hypnorm, (fentanyl 0.2 mg/ml and fluanisone 10 mg/ml) 0.1 ml/kg, intramuscularly and the pupils were dilated with Cyclogyl (cyclopentolate hydrochloride 1%) to a pupil diameter of 8–9 mm. After 30 minutes of dark adaptation a Burian-Allen bipolar ERG contact lens electrode was applied on the topically anesthetized cornea together with a subcutaneous ground electrode on the neck. The lens was lubricated with methylcellulose (2%). Responses were obtained with a wide band filter (-3 dB at 1 Hz and 500 Hz), stimulating with single full-field flashes (30 µs) with dim blue light (Wratten filters # 47, 47A and 47B) and of white light (0.8 cd.s/m2). Cone responses were obtained with 30 Hz flickering white light (0.8 cd s/m2) averaged from 20 sweeps with and without a background light of 10 fL. The luminances of the three different light stimuli refer to the light reflected from the Ganzfeld sphere.

Tissue preparation

At day 41, the rabbits were sacrificed and the eyes were dissected, gross examined and fixed for 1 h in 4% formalin, pH 7.3 in a 0.1 M Sørensen’s phosphate buffer (PB). After fixation, the specimens were washed with 0.1 M Sørensen's PB, and then washed again using the same solution containing sucrose of rising concentrations (5-25%). The specimens were sectioned at 12 µm on a cryostat, and each 10th slide was stained with hematoxylin and eosin according to standard procedures. For glial fibrillary acidic protein (GFAP) immunolabeling, sections were washed in 0.1 M of sodium phosphate-buffered saline pH 7.2 (PBS) with 0.25% Triton X-100 (PBS/Triton) and incubated with the primary antibody (anti-GFAP, clone G-A-5; Boehringer Mannheim Scandinavia, Bromma, Sweden, diluted 1:4 with PBS/Triton with 1% bovine serum albumin) overnight at +4°C. After incubation, the slides were rinsed in PBS/Triton, incubated with fluorescein isothiocyanate (FITC)-conjugated antibodies for 45 min, rinsed, and mounted in custom-made anti-fading mounting media. Unoperated eyes served as controls. For negative controls, the same labeling procedure without the primary antibody was performed on both the normal left and the operated right eye of the animals.

Results

Sol physical properties

Table 1 shows the physical properties measured for the sols. The addition of PEG to pH 7.4 PBS resulted in a decrease in pH, which remained above 7 in all cases. Both the elastic and loss moduli increased with increasing molecular weight at constant PEG concentration in PBS of 5 wt.%. Refractive indices decreased slightly with increasing molecular weight and were approximately n_D of 1.339 at 25ºC converted from Brix % in all sols. The sols were not as clear as pure water, but permitted transmission of meaningful visual information (Fig. 1A). Transparency appeared unchanged when heating the sols from 4 ºC to 37 ºC. S200 could be drawn in via a 23 gauge cannula and S300 and S400 via a 19 gauge cannula and this appeared unchanged at 37 ºC. A small amount of PEG remained insoluble, observed by addition of a blue hydrophilic dye to the sols. This fraction is larger in S400 compared with S200 and S300 (Fig. 1B).

Table 1. Sol physical properties

Sol name	**PEG molecular weight (kDa)**	**pH**	**Elastic modulus G' (Pa)**	**Loss modulus G" (Pa)**	**Refractive index at 25 ºC (Brix %)**
S200	**200**	7.04	0.05	1.05	5.2
S300	**300**	7.13	0.74	4.68	5.1
S400	**400**	7.06	7.59	20.56	5.0

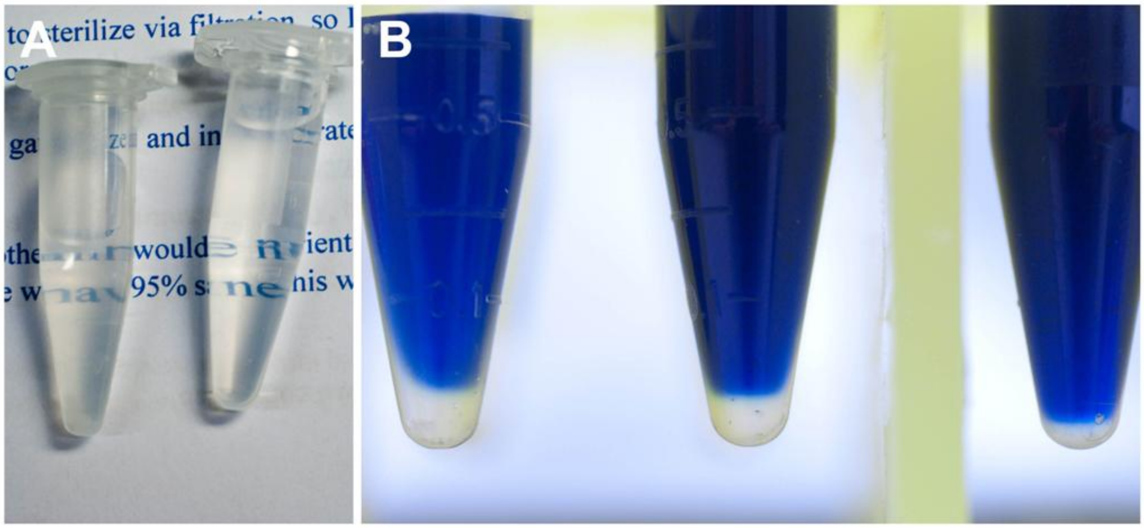

Figure 1. Poly(ethylene glycol) (PEG) sols. **A.** Transparency of PEG sol (left) compared to distilled water (right). **B.** Addition of hydrophilic blue dye to PEG sols showed a hydrophobic precipitate. The hydrophobic region was larger, the higher the molecular weight of PEG. S400 (left), S300 (middle), S200 (right).

Post-operative evaluation

Results are summarized in Table 2. During surgery, one eye had a retinal rupture and bleeding in the anterior chamber due to contact with a surgical instrument (#1 S300). After 6 days post-operatively, two eyes injected with the PEG solutions displayed hypotony, with an intra-ocular pressure (IOP) approximately 0 mmHg (#1 S300, #8 S400), while the remaining 4 had an IOP of approximately 10-15 mmHg. Hypotonic eyes had a slight cataract superiorly but the majority of the lens was clear. No outer signs of inflammation were observed. One retina had a retinal detachment of approximately 40% due to the surgery (#1 S300). The remaining eyes displayed a normal retina without signs of edema. The vitreous was clear in the central and superior part. However, all eyes containing PEG displayed small white aggregates in the inferior vitreous body (Fig. 2). After 20 days post-operatively the precipitate was greatly reduced compared to 6 days post-operatively in most PEG injected eyes. No precipitate was present in BSS eyes. One eye had a total retinal detachment (#1 S300) (Fig. 3 A, B). Two eyes had peripheral retinal detachments (#2 S400, #6 S400), possibly due to ruptures at the sclerotomy sites. No inflammation was observed externally or internally (Fig. 3 C, E). The lens was partly opaque in one eye (#2 S400), but remained clear in all others. IOP was not elevated in any eye but 2 eyes with detachment were hypotonic, between 0-5 mmHg (#1 S300, #6 S400). Upon termination, after 41 days post-operatively, the vitreous was clear in all animals (Fig. 3 B, D, F). The IOP was normal in all eyes. Minimal cataract was noted in some eyes, but appeared to be reduced. Precipitates were found in the inferior vitreous in a few eyes (#6 S400, #8 S400), but was reduced compared to earlier examination time points. The retina was completely detached in two eyes (#1 S300, #6 S400) and some folding was also noted (#4 BSS, #5 S300, #6 S400) (Fig. 3 F). The sols in all eyes were completely resorbed.

Table 2. Pre-, per-, and post-operative data.

Case # and vitreous substitute	Injection volume. Surgical notes	Day 6	Day 20	Day 41	Dissection	H&E	GFAP
#1 S300	0.8 mL Surgery: Retinal rupture and anterior chamber bleeding.	Clear, Conjunctiva ok. Temporal detachment, otherwise attached. Some precipitate centrally. IOP 0	No injection. Cornea clear. No cataract. Clear vitreous. Total funnelshaped RD. IOP 0 (palp)	No external inflammation. Minimal cataract nasally. Clear vitreous. Total retinal detachment. IOP normal.	Total RD, highest inferiorly. Seems inflamed here	Total retinal detachment with destruction of the retina. Choroidal inflammation and dissolved RPE	Upregulated, Müller disorganized
#2 S400	0.9 mL	Minimal conj. injection. IOP approx. 20. Cornea clear. Moderate cataract. Minimal vitreous haemorrhage No precipitate	No injection, cornea clear. Lens clear anteriorly, posterior cataract. RD in the periphery inferiorly, centrally ok. Some precipitate on the posterior lens capsule. IOP 10.	Minimal cataract. Vitreous clear. Retina attached and normal. IOP ok	Normal dissection	Retina appears normal. Epi and intraretinal clusters of brownish large cells (leucocytes?).	Upregulated generally, Normal Müller Morphology
#3 BSS		Not examined	No injection. Cornea clear. Lens and vitreous clear. IOP 10 (palp).	Clear, retina ok, IOP ok	OK	Normal	Minimal upregulation
#4 BSS		Not examined	No injection. Cornea clear. Mild cataract corresp. To the right sclerotomy. Vitreous clear IOP 10 (palp).	Clear, retina ok, IOP ok	Minimal retinal folds, artefact?	Normal	Minimal upregulation
#5 S300	1.3 mL	Minimal injection. Precipitate in the vitreous	No injection. Cornea clear. Mild cataract. Vitreous	Minimal cataract, vitreous clear without precipitate.	Some retinal folding. No gel	Minimal central detachment (fold?). Retina looks	Some elongation of Müller cell nuclei

		inferiorly IOP approx. 10. Minimal cataract.	clear. Some precipitate inferiorly. Retina ok. IOP 10 (palp).	Retina ok, IOP ok		ok, but inflammatory cells subretinally and large cells in the ONL are present on some sections	
#6 S400	1.5 mL (backflow)	Minimal injection. Precipitate in the inferior vitreous. Photo taken. IOP approx. 15. Minimal cataract.	No injection. Lens clear. Some precipitate inferiorly. RD superiorly by the myelinated streak and inferiorly. Centrally ok. IOP 0-5	No cataract. Vitreous clear but slightly brownish with precipitate inferiorly. One retinald fold superiorly, otherwise ok. IOP ok	Total RD, artefact from dissection ? No gel, Retina missing superiorly	Total RD, swollen choroid. Outer/Inner segments missing. developed a low detachment in the postoperative period	Upregulated generally, Normal Müller Morphology
#7 S400	1.2 mL	Minimal injection. Precipitate in the vitreous inferiorly IOP approx. 10. Minimal cataract.	No injection. Cornea clear. No cataract. Clear vitreous. Retina ok. Some precipitate inferiorly. IOP 10.	Clear, retina ok, IOP ok	Normal, no gel	Normal	Upregulated generally, Normal Müller Morphology
#8 S400	1.0 mL	Minimal injection. Precipitate in the inferior vitreous. Photo taken. IOP approx. 0. Minimal cataract.	No injection. Cornea clear. No cataract. Clear vitreous. Retina ok. Some precipitate inferiorly. IOP 10.	No cataract, vitreous with minimal precipitate inferiorly, retina ok, IOP ok.	Some precipitate inferiorly, otherwise normal. No gel	Normal.	Upregulated generally, Normal Müller Morphology

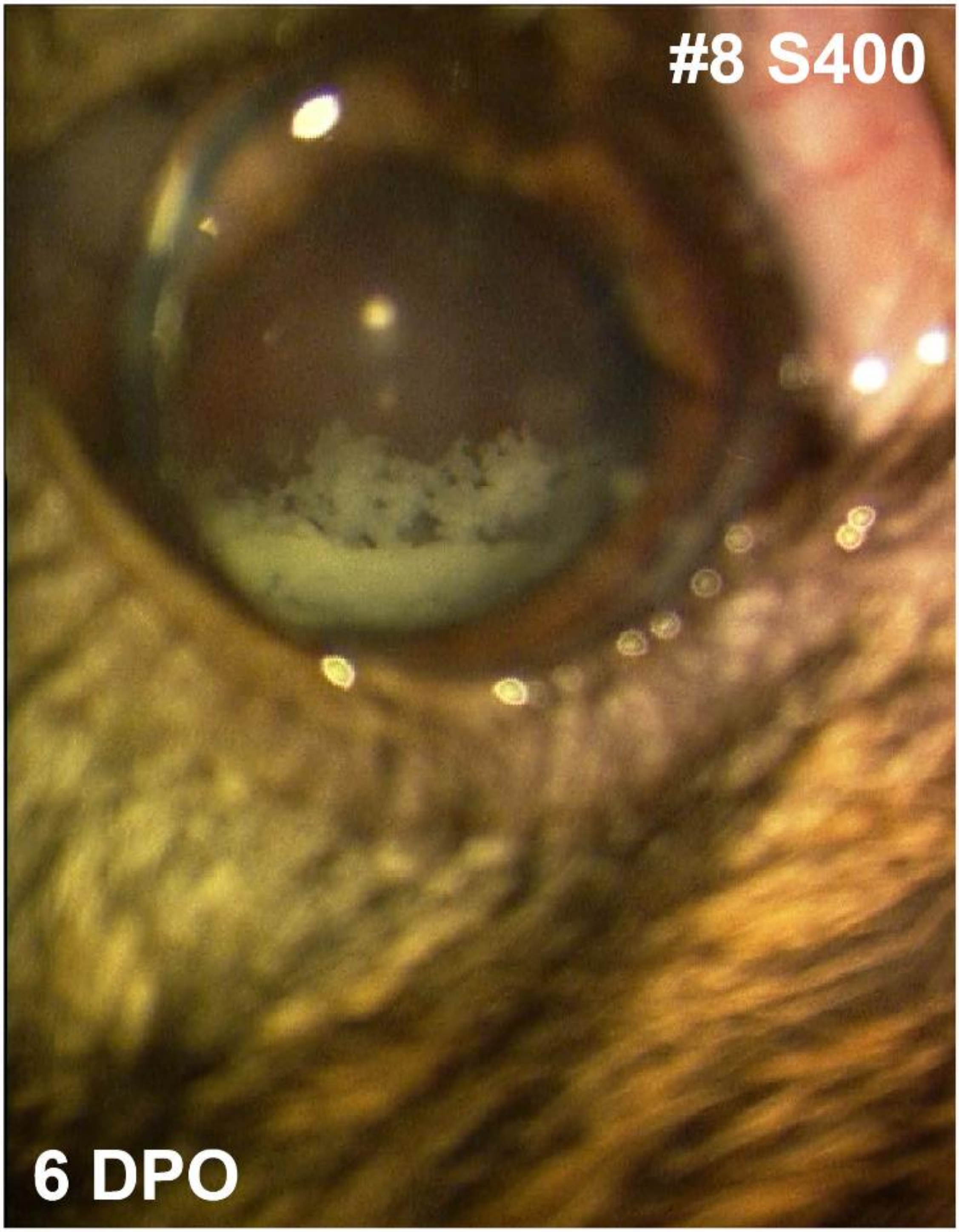

Figure 2. Ophthalmoscopic examination 6 days postoperatively. PEG injected eyes displayed white precipitate in the inferior vitreous body. DPO = days postoperatively.

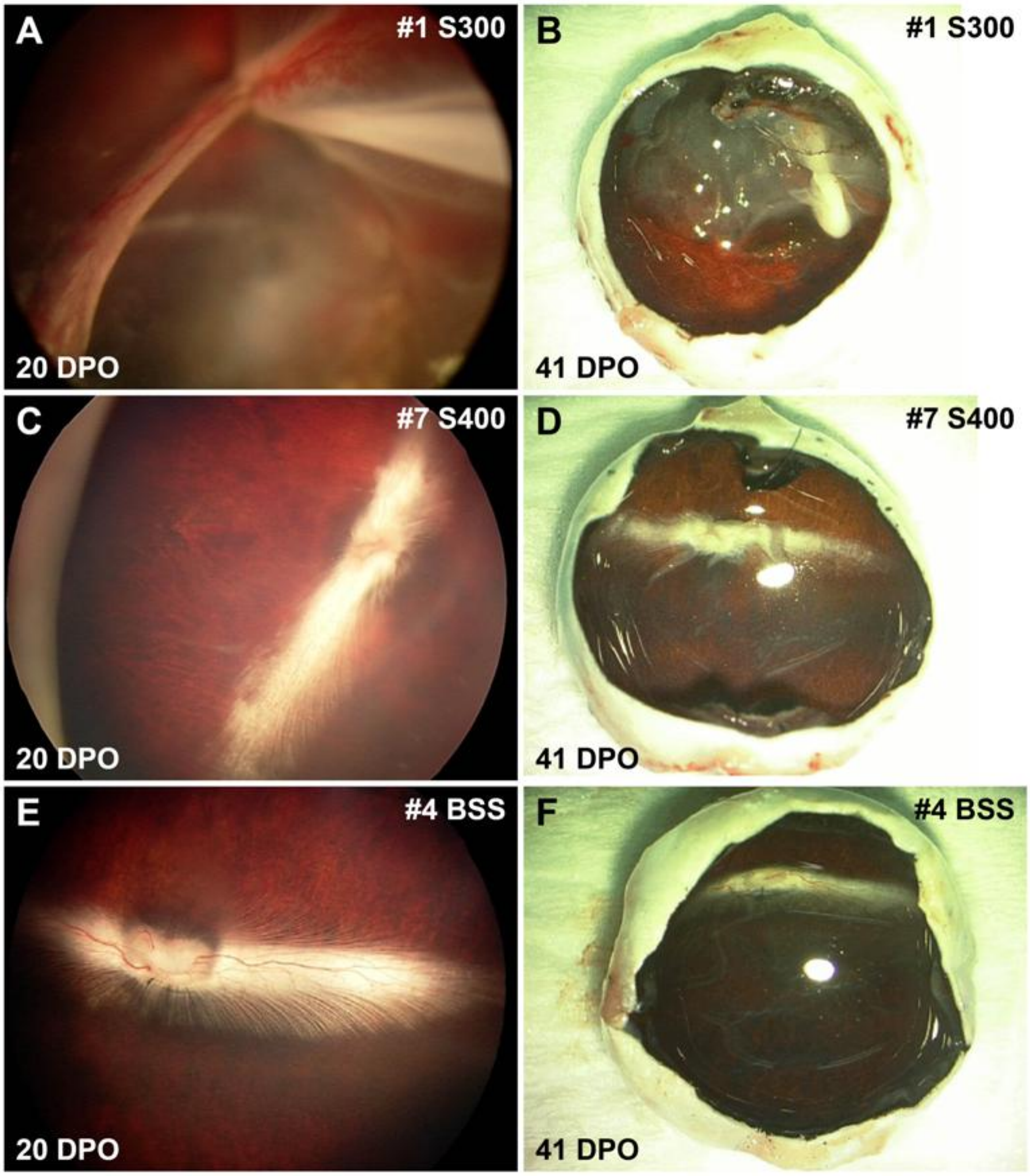

Figure 3. Images of retinas 20 days postoperatively (**A, C, E**) and eyes at dissection 41 days postoperatively (**B, D, F**). **A-B.** #1 S300. Total retinal detachment caused during surgery (**A**) with no sol remaining (**B**). **C-D.** #7 S400. Eye injected with PEG sol was normal with retina attached (**C**) and no sol remaining (**D**). **E-F.** #4 BSS. Eye injected with balanced saline solution displayed attached retina (**E**) and minimal retinal folds (**F**). DPO = days postoperatively.

Histology

#1 S300 developed a retinal detachment during surgery displayed a pathological retina in hematoxylin and eosin (H&E) stained sections, confirming total detachment destruction of the retina, choroidal inflammation and dissolved retinal pigment epithelium (RPE) (Fig. 4A). #6 S400 developed a retinal detachment post-operatively. This eye displayed total retinal detachment, swollen choroid and missing outer and inner photoreceptor segments. #5 S300 had a minimal central detachment, large inflammatory cells in the outer nuclear layer (ONL) and subretinal space (Fig. 4D). The macroscopically observed precipitates seen in #2 S400 were observed in histological sections as brown clumps on the retinal surface, and also in an area within the inner retinal layers, with presence of macrophages (Fig. 4 E, F). The remaining eyes had normal retinal morphology (Fig. B, C).

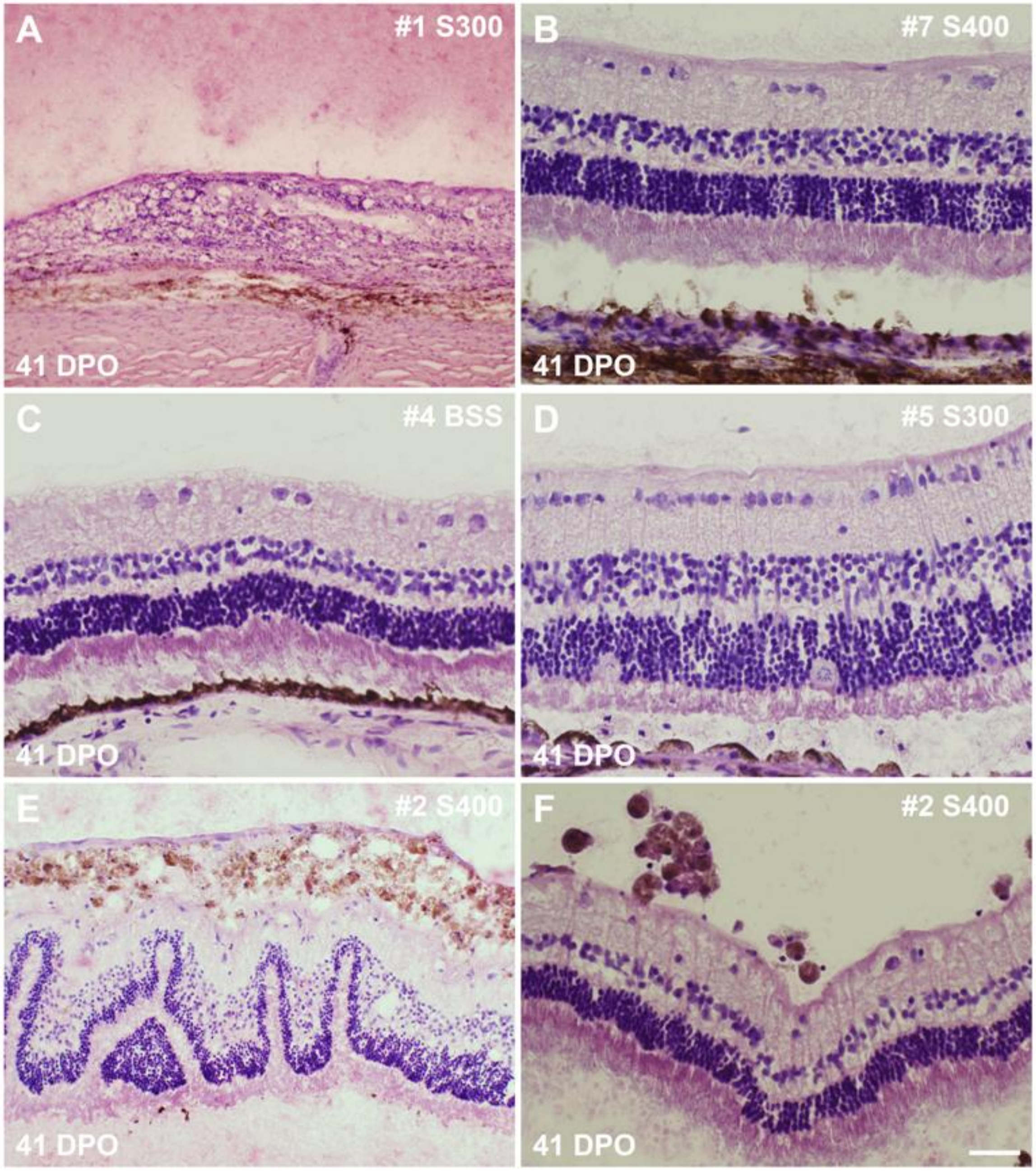

Figure 4. Hematoxylin and eosin (H&E) stained sections. **A.** #1S300. Total destruction of the retina with choroidal inflammation and dissolved retinal pigment epithelium (RPE). **B-C.** #7 S400 (**B**) and #4 BSS (**C**) displayed normal retinal morphology. **D.** #5 S300. The retina of had some elongation of Müller cell nuclei, large cells in the ONL and subretinal inflammatory cells. **E-F.** #2 S400. Brown precipitate and macrophage invasion on retinal surface (**E**) and inner retinal layers (**F**). Scale bar = 200 microns (**A**), 50 microns (**B-F**). DPO = days postoperatively.

Immunofluorescence labeling

All eyes injected with PEG sols displayed upregulation of glial fibrillary acidic protein (GFAP), as a sign of Müller cell activation (Fig. 5). The eye with surgically induced total retinal detachment displayed disorganized Müller cells (#1 S300). Another eye, which had a minimal central detachment, had elongated Müller cell nuclei (#5 S300). In BSS injected eyes GFAP labeling was comparable with normal unoperated controls with discrete labeling of Müller cells seen only in the periphery.

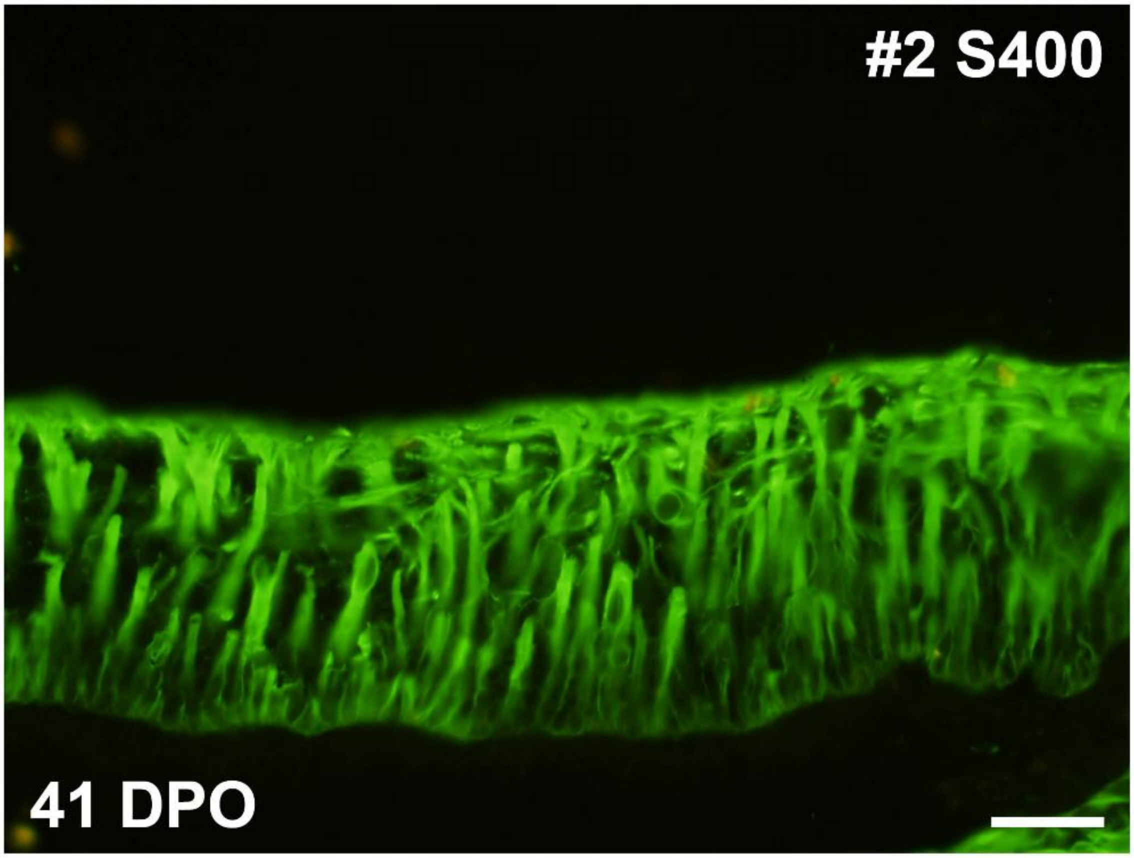

Figure 5. Glial fibrillary acidic protein (GFAP) immunofluoresence stained section. #2 S400. Eye injected with PEG sol displayed upregulation of GFAP in Müller cells. Scale bar = 50 microns. DPO = days postoperatively.

Electroretinography

Full-field electroretinography (ERG) measurements were obtained pre- and post-operatively in all 8 eyes (Table 3). All but one case followed the histological results. The two eyes with total retinal detachment displayed no residual response could be measured (#1 S300, #6 S400). Another eye, with a minimal central detachment, also displayed no response (#5 S300). All other eyes displayed only minor changes compared to pre-operative baseline recordings.

Table 3. Pre- and post-operative (day 41) ERG data. Values are given of the wave amplitudes (μV) for rod ERG (blue light), combined ERG (white light), and dark-adapted single-flash cone ERG (30 Hz flicker).

Eye # and vitreous substitute	**Blue light**		**White light**		**30 Hz flicker**		**Summary**
	Pre-op	**Post-op**	**Pre-op**	**Post-op**	**Pre-op**	**Post-op**	
#1 S300	89.8	0	61.2	0	20.8	0	All modalities reduced to 0
#2 S400	72.9	78.1	50.8	69	10.4	8.16	No change
#3 BSS	76.8	53.4	50.1	50.1	20.8	12.3	Reduced rods and cones
#4 BSS	39.1	89.8	27.3	31.3	10	3.94	Reduced cones, increased rods
#5 S300	56	0	59.9	0	26.3	0	All modalities reduced to 0
#6 S400	91.1	0	65.8	0	19.7	0	All modalities reduced to 0
#7 S400	40.4	147	46.9	84.6	12.7	12.2	Increased rods and combined
#8 S400	56	52.1	65.8	57.3	12.5	15.4	No change

Discussion

The vitreous is a hydrogel composed of collagen and hyaluronic acid, with reported values of 98-99% water. pH 7.0-7.4, with and elastic modulus of 4.2-4.7 Pa and a loss modulus of 1.9-3.7 Pa and a refractive index of 1.3345-1.3348 [3]. 5 wt.% PEG sols with average molecular weights between 200,000 and 400,000 g mol^{-1} approximated the viscoelastic properties of the natural retina, with a high polymer content. Using phosphate buffered saline (PBS), the pH values of the resulting sols were slightly above 7, and all sols had similar refractive indices (1.339 at 25ºC) to the natural vitreous. PEG sols presented an attractive vitreous substitute to test in an experimental vitrectomy model, especially given promising results indicating ocular biocompatibility of PEG hydrogels [20-22].

Both eyes injected with S300 had retinal detachment and loss of electrical function (#1, #5). In one eye, the retinal detachment was caused during surgery (#1 S300). In the other, a minimal central detachment and subretinal and ONL inflammation was observed upon histological examination (#5 S300). It is uncertain why this eye had no postoperative ERG responses after 41 days. In 3 out of 4 eyes with S400, the PEG sol had no apparent effect on retinal morphology and electrical function. One eye with S400 developed a postoperative retinal detachment (#6 S400). However, all eyes injected with PEG sols exhibited elevated GFAP expression, indicative of retinal stress and Müller cell activation, which was not observed in BSS eyes. BSS was well tolerated and resulted in minimal GFAP upregulation. S400 affected the retina to a lesser degree than a previously tested material, poly(acryl-imide), which caused retinal edema [18]. The tolerability of S300 was inconclusive, limited by the small sample size.

Following removal of the natural vitreous, metabolical and physiological changes occur within the eye, involving oxygen concentration, osmotic balance and molecular transport that may affect both the lens and the retina [24, 25]. The normal morphology and ERG responses observed in the majority of eyes injected with S400 may indicate that the nutritional demands of the retina are met by the PEG sol. Furthermore, the PEG sols did not result in IOP elevation, an important clinical consideration. However, the PEG sols were not retained in the vitreous body throughout the post-operative period. It takes about 3-7 days for the laser phototherapy to form permanent adhesions and in complex cases a tamponade may be required for several months [26]. Future work will focus on cross-linking PEG following injection, so that the resulting viscoelastic insoluble gel is retained for a longer period in the vitreous body. This could be achieved, for example, through the use of PEG with thiol and acrylate functional groups to form cross-links *in situ* [27, 28].

References

1. Parel JM, Gautier S, Jallet V,Villain FL. Silicon Oils: Physicochemical Properties. In: Ryan SJ, editor. Retina, third edition. St. Louis: Mosby 2001;2173–94.
2. Kirchhof B, Wong D, Van Meurs J, Hilgers RD, Macek M, Lois N et al. Use of perfluorohexyloctane as a long-term internal tamponade agent in complicated retinal detachment surgery. *Am J Ophthalmol* 2002;133(1):95-101.
3. Swindle KE and Ravi N. Recent advances in polymeric vitreous substitutes. *Exp Rev Ophthalmol* 2007;2(2):255-65.
4. Denlinger J, Balazs E. Replacement of the Liquid Vitreus with Sodium Hyaluronate in Monkeys I. Short-term Evaluation. *Exp Eye Res* 1980;31:81-99.
5. Denlinger J, El-Mofty A, Balazs E. Replacement of the Liquid Vitreus with Sodium Hyaluronate in Monkeys II. Long-term Evaluation. *Exp Eye Res* 1980;30:101-17.
6. Koster R, Stilma JS. Comparison of vitreous replacement with Healon and with HPMC in rabbits´eyes. *Documenta Ophthalmologica* 1986;61:247-53.
7. Koster R, Stilma JS. Healon as intravitreal substitute in retinal detachment surgery in 40 patients. *Documenta Ophthalmologica* 1986;64:13-7.
8. Gerke E, Meyer-Schwickerath G, Wessing A. Healon in retinal detachment with proliferative vitreoretinopathy. *Graefe's Arch Clin Exp Ophthalmol* 1984;22:241-3.
9. Swindle-Reilly KE, Shah M, Hamilton P, Eskin T, Kaushal S, Ravi N. Rabbit study of an in situ forming hydrogel vitreous substitute. *Invest Ophthalmol Vis Sci* 2009;50(10):4840-6.
10. Maruoka S, Matsuura T, Kawasaki K, et al. Biocompatibility of polyvinylalcohol gel as a vitreous substitute. *Curr Eye Res* 2006;31:599–606.
11. Soman N, Banerjee R. Artificial vitreous replacements. *Biomed Mater Eng* 2003;13:59–74.
12. Hong Y, Chirila TV, Vijayasekaran S, Shen W, Lou X. Dalton PD. Biodegradation in vitro and retention in the rabbit eye of crosslinked poly(1-vinyl-3-pyrrolidinone) hydrogel as a vitreous substitute. *J Biomed Mater Res* 1998;39(4):650-9.
13. Yang H, Wang R, Qisheng G, Zhang X. Feasibility study of chitosan as intravitreous tamponade material. *Graefes Arch.Clin.Exp Opthalmol* 2008;246:1097-1105.
14. Katagiri Y, Iwasaki T, Ishikawa T, Yamakawa N, Suzuki H, and Usui M. Application of Thermo-setting Gel as Artificial Vitreous. *Jpn J Ophthalmol* 2005;49:491–6.
15. Gao Q, Mou S, Ge J, et al. A new strategy to replace the natural vitreous by a novel capsular artificial vitreous body with pressure control valve. *Eye* 2008;22:461–8.
16. Lahiri A, Waters R. Experience with Bio-Alcamid, a new soft tissue endoprosthesis. *Journal of plastic, reconstructive & aesthetic surgery : JPRAS* 2007;60(6):663-7.
17. Claoue BL, Rabineau P. The polyalkamide gel: Experience with Bio-Alcamid^{TM}. *Semin Cutan Med Surg* 2004;23:236-240.

18. Crafoord S, Andreasson S, Ghosh F. Experimental vitreous tamponade using poly(alkyl-imide) hydrogel. *In preparation* 2010.

19. Sawhney AS, Pathak CP, Hubbell JA. Bioerodible hydrogels based on photopolymerized poly(ethylene glycol)-co-poly(.alpha.-hydroxy acid) diacrylate macromers. *Macromolecules* 1993;26(4):581-7.

20. Duvvuri S, Janoria KG, Pal D, Mitra AK. Controlled Delivery of Ganciclovir to the Retina with Drug-Loaded Poly(D,L-lactide-co-glycolide) (PLGA) Microspheres Dispersed in PLGA-PEG-PLGA Gel: A Novel Intravitreal Delivery System for the Treatment of Cytomegalovirus Retinitis. *Journal of Ocular Pharmacology and Therapeutics* 2007;23(3):264-74.

21. Wathier M, Johnson S, Carnahan MA, Baer C, McCuen BW, Kim T, Grinstaff MW. In Situ Polymerized Hydrogels for Repairing Scleral Incisions Used in Pars Plana Vitrectomy Procedures. *Chem Med Chem* 2006;1(8):821-5.

22. Ufret R, Yu SY, Christoforidis J, D'Amico DJ. Evaluation of a polyethylene glycol (PEG)–derived glue as a potential bioadhesive for vitreoretinal applications. *Invest Ophthalmol Vis Sci* 2004;45:E-Abstract 2054.

23. Gjörloff K, Andreásson S, Ehinger B. Standardized full-filled electroretinography in rabbits. *Documenta Opthalmologica* 2004;109:163-8.

24. Stefansson E. Physiology of vitreous surgery. *Graefe's Arch Clin Exp Ophthalmol* 2009;247:147-63.

25. Holekamp NM, Shui YB, Beebe DC. Vitrectomy surgery increases oxygen exposure to the lens: a possible mechanism for nuclear cataract formation. *Am J Ophthalmol* 2005;139(2):302–10.

26. Johansson K, Malmsjö M, Ghosh F. Tailored vitrectomy and laser photocoagulation without scleral buckling for all primary rhegmatogenous retinal detachments. *Br J Opthalmol* 2006;90:1286-91.

27. Pritchard CD, O'Shea TM, Siegwart DJ, Calo E, Anderson DG, Reynolds FM, et al. A novel injectable thiol-acrylate poly(ethylene glycol) hydrogel for sustained release of methylprednisolone sodium succinate. *Submitted to Biomaterials* 2010.

28. Brandl F, Henke M, Rothschenk S, Gschwind R, Breunig M, Blunk T, et al. Poly(Ethylene Glycol) Based Hydrogels for Intraocular Applications. *Adv Eng Mater* 2007;9(12):1141-9.

Acknowledgments

This study was supported by The Faculty of Medicine, University of Lund, The Swedish Research Council, The Torsten and Ragnar Söderberg Foundation, and research funds of Departments of Ophthalmology Örebro. C.D.P. was supported by the MIT/CIMIT Medical Engineering Fellowship and a gift to MIT by InVivo Therapeutics Corporation.

VII.

Integrative Perspective Paper – A business plan towards clinical trials of biomaterials for the treatment of retinal detachment

Christopher D. Pritchard (1,3), William Herbert (2), Adrian Lu (3)

(1) Department of Chemical Engineering
Massachusetts Institute of Technology, Cambridge, MA 02139, USA

(2) Department of Materials Science and Engineering
Massachusetts Institute of Technology, Cambridge, MA 02139, USA

(3) MIT Sloan School of Management
Massachusetts Institute of Technology, Cambridge, MA 02139, USA

Presented at the MIT Sloan School of Management to students and staff on December 12, 2011.

Executive Summary

Market opportunities

There is a common eye surgery that is called vitrectomy and tamponade (VT). We are proposing to commercialize a new surgical biomaterial to be used in VT surgery. Our initial estimate is there are approximately 150,000 VT surgeries every year in the United States alone. This surgery is also routine in Europe. These numbers are expected to grow with an aging population.

Our new material meets an unmet medical need. For example, detachment of the retina is a medical emergency. If untreated, the torn retina continues to peel off resulting in blindness. This VT surgery is required to reattach the retina.

During surgery the jelly that fills the eye ball has to be removed. This jelly is typically replaced with silicone oil or gas. However, oil and gas only last for short periods of time in the eye and can cause complications such as glaucoma and cataracts. Our material is superior in every way to these options.

Sales and marketing strategy

Initially, our target customer is the expert ophthalmic surgeon. She is the thought leader who will make the decision on whether not the technology is clinically superior to existing materials. Without her buy-in, health insurers and patients are unlikely to support or demand the technology.

Our early stage marketing strategy is to find prominent surgeons to participate in the clinical trial of the technology, who will then promote the use of the technology in their professional circles, based on quality data. After endorsement by the medical community, our sales and marketing strategy will evolve to target the other customers: health insurance companies and patients.

Product description

Our team has worked with surgeons in to develop a special biomaterial that mimics the eye's natural jelly and can be used in the eye long-term. We propose to commercialize the gel as a medical device. The pathway for filing a medical device has simpler regulatory hurdles and testing requirements than drugs or biologics.

Financing needed and planned exit

$4 million for pre-clinical trials (A round: $1m, B round: $3m)

Potential double-down for investors at clinical stage. There will be decision points to exit upon entering both the clinical or market phase, most likely to a strategic acquirer.

Financial projections

3 major phases of development with optionality at each transition for further investment or sale.

In "MARKET" phase, gross margins are > 99%. Total addressable market: $750m (US) > $2bn (US & Europe). This makes us a $32 million company assuming an extremely conservative 5% penetration rate, or a $240 million company assuming a more realistic yet still conservative 50% penetration rate.

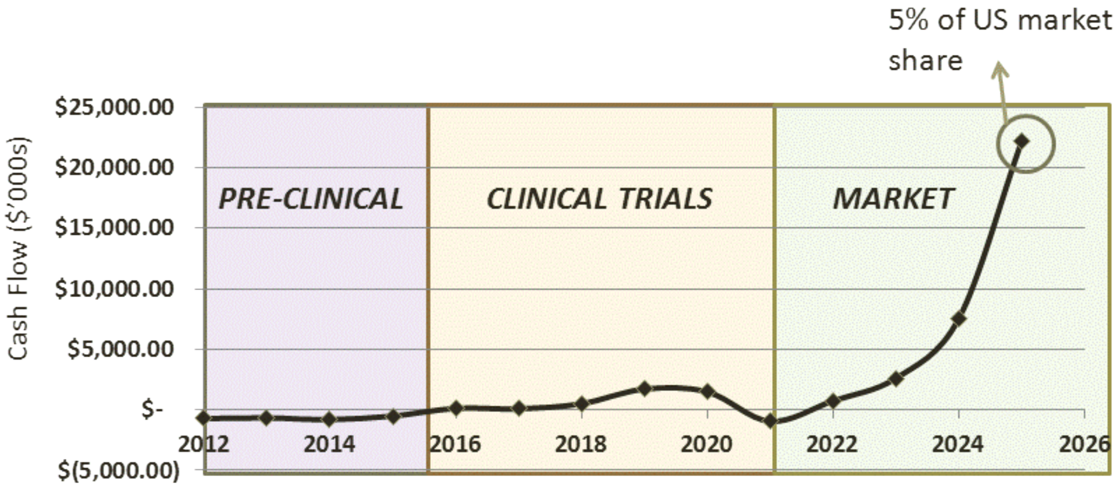

Figure 1. Cash flow projection for Hydrogel through 2025, reflecting three major phases of development with the option for double-down investment or strategic exit/sale at each transition.

Team

Adrian Lu – Chief Executive Officer, technology marketing and sales experience

Christopher Pritchard, PhD – Chief Technology Officer, expertise in hydrogels, former CSO of InVivo Therapeutics

William Herbert – Chief Operating Officer, manufacturing and scale-up expertise

Vision and Values

- Our vision is to improve vision.
- We are committed to improving the lives of patients suffering from long-term vision related disorders.
- We believe in quality engineering.
- We believe in creating superior technologies that can have a significant impact on patients' lives recovering from surgery.
- We believe in providing surgeons with the most innovative and clinically relevant technologies to make their ability to treat their patients easier.
- We believe in reducing the burden of healthcare through technologies that prevent repetitive or chronic medical complications.
- We listen to the challenges faced by surgeons and strive to address their most critical issues
- We create healthcare solutions
- We are a couple of good blokes who want to be superheroes. We can do better than 'do no evil', we will 'do good'.

Market Analysis and Competitive Advantage

Cost of the surgery

The 2010 dollar price of a vitrectomy surgery is listed by several sources below- both for Medicare insurance and for industry averages with two different types of anesthesia. The average is just under $5000, with the cost to the hospital of performing the surgery on the order of $800. Therefore the hospital administration and surgeon charge a premium of roughly 85% over the cost of the surgery.

Table 1. Cost of vitrectomy (retinal re-attachment) surgery from major US Eye hospitals.

Patient Charge	Cost to Hospital	No of Surgeries in 2010	Source
$3467	$925	461	Mass Eye & Ear Medicare Claims * (ahd.com)
$5025	$844	642	Miami Hospital Medicare Claims (ahd.com)
$3508	$554	853	NY Eye & Ear Medicare Claims (ahd.com) [1]
$7177±644	N/A	N/A	[2]
$5469±514			[3]
$4930	$774	N/A	AVERAGE

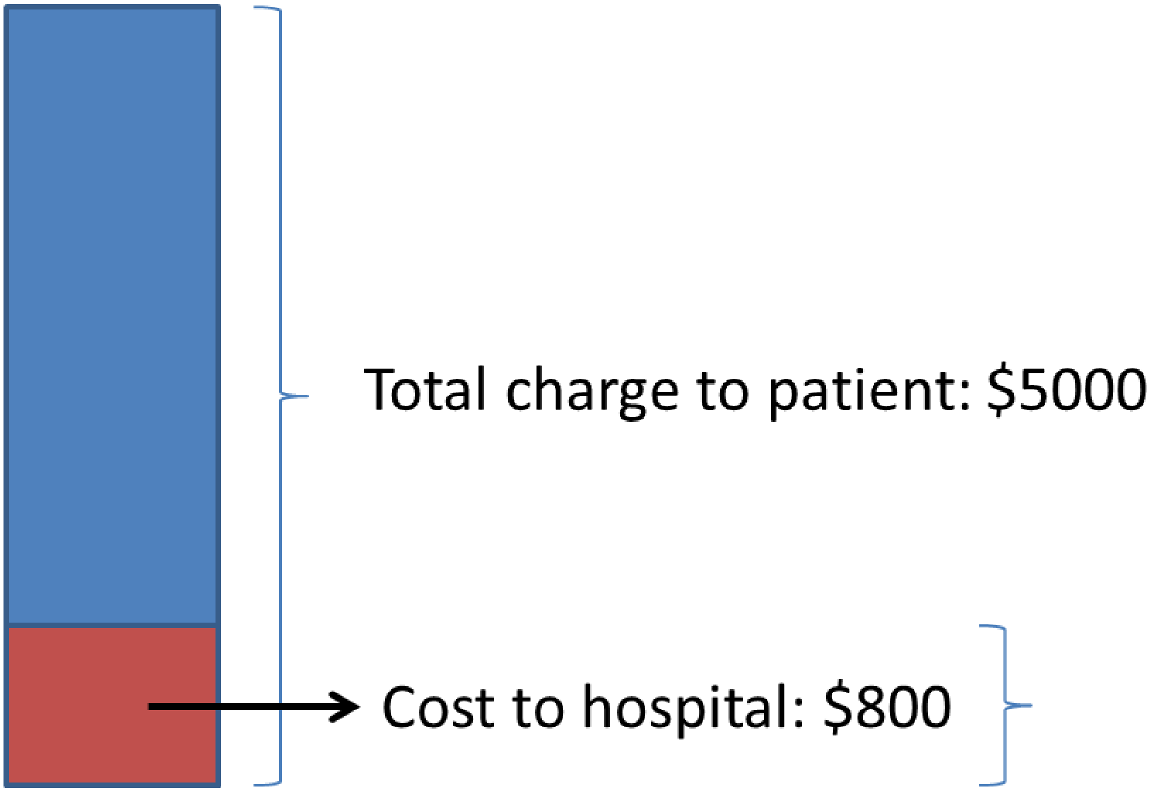

Figure 2. COGS to the hospital of performing a vitrectomy surgery. Hydrogel will be sold at a premium, adding cost per surgery to the end user (the patient and his/her insurance firm), but also allowing the hospital and doctor to increase their revenue per surgery. This is important since the DMU is the ophthalmic surgeon.

Pricing

Competition pricing

Silicone oil: $100 per vial (such as Alcon Laboratories SILIKON 1000)

Gas: Marginal cost of dispensing one extra unit of gas for the eye should be near zero

Hydrogel pricing

Our pricing strategy is to capture the value created by the significant reduction in expected cost of treatment to the patient. To that end, our product will have a $4900 premium over the competition and will cost $5000 for each unit of treatment.

Table 2 below shows our gross margin, where it can be seen that our estimated marginal cost of producing each unit of our device is $5. The low cost of production is due in part to the fact to the simple method of producing the synthetic polymer that forms this medical device. The value is in the intellectual property covering the production method.

Due to this low marginal cost, our gross margin, which is the margin on revenue before cost of sales, general and administrative expenses are taken into account, is a very healthy 99.90%.

Table 2. Gross margin on Hydrogel product

Price per unit	$5,000
COGS per unit	$5
Gross margin	**99.90%**

The price premium for Hydrogel can be easily justified when the total cost of treatment is considered. Fig. 3 shows a simple calculation of the expected cost of treatment of our major competing product, silicone oil, versus the cost of Hydrogel treatment. The expected cost takes into account:

- Odds of initial surgery success
- Likelihood of repeat surgery required
- Cost of follow-up treatment
- Risk of complications causing cataracts

Hydrogel outperforms silicone oil on all counts across these areas, giving an expected treatment cost of $11,300 which is a significant reduction over the expected cost of treatment of $12,500 using silicone oil. Furthermore, there is the intangible value to the patient of less intrusive and debilitating treatment improving quality of life. We also have not taken into account risks of other potential complications with existing surgeries such as glaucoma, which would further increase the expected cost of existing treatments.

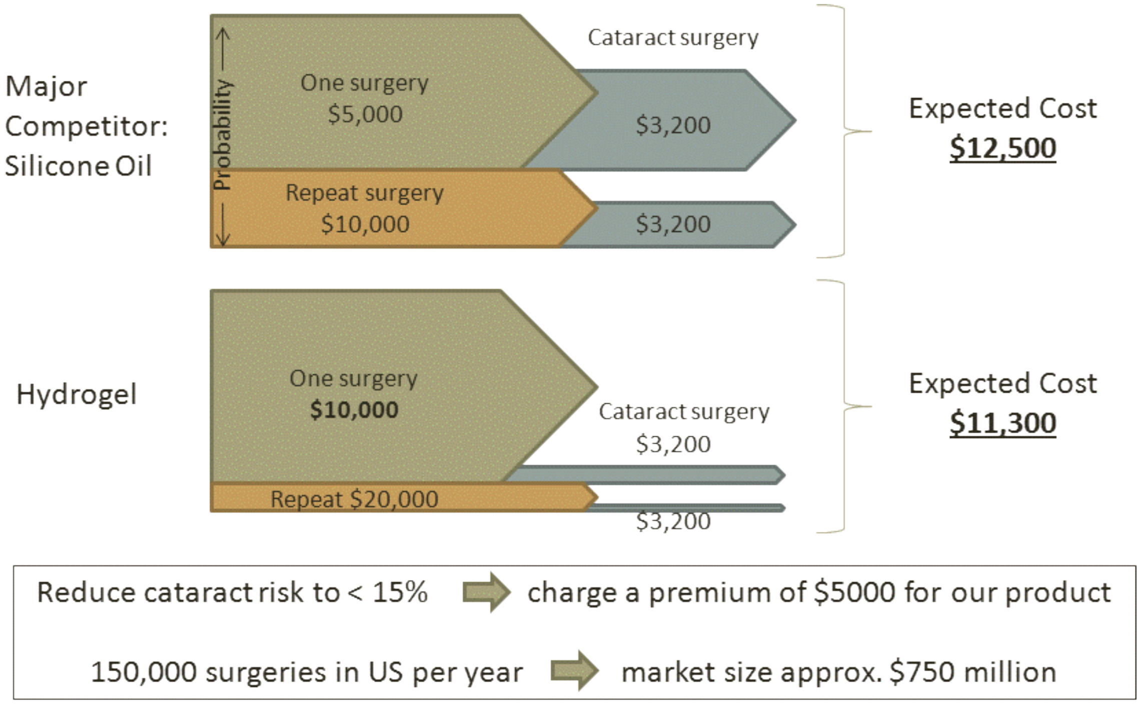

Figure 3. Comparison of expected total cost of treatment, taking into account Hydrogel's improvements in reducing the need for repeat surgery, and also the risk of further cataract surgery. See Table 4 for statistics on Silicone Oil outcomes.

Total addressable market size with current products (US only)

Total spent on surgery = 150,000 cases x $5000 = $750 M

Total spent by hospitals providing this surgery (excluding labor) = $120 M

of which spent on current commoditized “tamponade material” ≈ $100 per surgery

➔ $15 M total market per annum (currently)

This relatively small market size reflects the current low price paid for an eye jelly replacement material. We believe that as a more effective, commoditized product, Hydrogel can be priced at $5000 per surgery. Using this price, our product still reduces the overall surgical cost to the consumer, due to the greatly reduced risk of requiring repeat or further surgeries. This estimate is in line with advice from our expert ophthalmic surgeon, as well as our calculations on lifetime surgical costs outlined in the Pricing section. Given this premium we charge for Hydrogel, the US market is:

➔ $750 M total market per annum in the US (with Hydrogel premium)

➔ > $2 B total market per annum in the US and Europe (with Hydrogel premium)

How the market size will change over time

- Ageing population
- Increase with development of healthcare in emerging countries
- Our opportunity is mainly a function of product switching in addition to market growth

How developments in the field are adopted

Most new therapies are introduced at major ophthalmology meetings such as ARVO, AAO and Club jules Gonin. Surgeons then go home and try the therapies for themselves.

Surgical products work differently compared with medical counterparts. The regulation surrounding surgery is much less strict depending on the material. For instance, heavy silicone oil was introduced in the early 2000´s without any official approval [4]. However, as far as intravitreal drugs are concerned, they need to be approved (FDA or corresponding). Nevertheless, a lot of "off-label use" is carried out and presented at meetings, (e.g. Avastin for ROP [5]).

Adopting new technologies is really up to each surgeon. Of course, this depends on local economic as well as hierarchical factors (a junior surgeon would not be able to use a very expensive new tool).

Pricing varies heavily different depending on the organization of health care. For example, in Sweden, about 95% is government run, but the financial control is not very strict. This means a senior surgeon has a lot of say about what equipment and tools they need.

Portrait of potential customers in the United States

The patient

Robert is a 67 year old retired lawyer from Boston. He is an avid bird watcher and golfer.

Recently, Robert began experiencing flashing lights and was diagnosed with **retinal detachment**.

His ophthalmic surgeon recommends **emergency surgery.**

Robert understands the importance of this surgery, and what matters most is:

- No medical complications
- No repeat surgery
- Convenient recovery

The surgeon

Stephen J. Ryan, MD is President, Doheny Eye Institute (USC), Distinguished Professor in Ophthalmology. He received his MD from Johns Hopkins University 1965 and did internships at Bellevue Hospital and Cornell Medical Division from 1965 – 1966. His residency was completed at Wilmer Eye Institute, Johns Hopkins University in Ophthalmology from 1966 –

1970, and his fellowship at the Armed Forces Institute of Pathology in Ophthalmologic Pathology from 1970 – 1971. His is board certified by the American Board of Ophthalmology and has professional society memberships in the American Academy of Ophthalmology, Institute of Medicine of the National Academy of Sciences, The Alliance for Eye and Vision Research.

Implications for business model

We have narrowed down the typical surgery cost to be about $5000 with an average cost to the hospital of $800. In terms of how we capture that value, our view is that we don't compete on cost terms to give hospitals a larger slice of the pie, but we compete on being the non-commoditized premium product which is worth paying more for than existing procedures, so we're increasing the size of the pie.

We plan to demonstrate to the insurers that the total cost of treatment (to make an analogy to Total Cost of Ownership) works out cheaper over the lifetime over the patient than existing methods. Reasons include eliminating the need for repeat surgery, decreased rate of further complications such as glaucoma and cataracts, which create further costs that the insurer needs to factor into the true cost of treatment. Litigation may be another potential cost saving.

The incumbent technologies are both commoditized. There are many producers of silicone oil and gas is even more commoditized - there's no magic to it at all and any industrial could get in the game for the existing products. The introduction of innovation and new materials to this space would set a precedent for biomaterials development in the eye, as well as drug delivery technologies. It is likely that we would see a competitive response not from incumbents (who make silicone oil or gases), but from companies who make surgical biomaterials for other parts of the body (e.g. Covidien, Boston Scientific).

With low costs of operations post clinical trials, there is a lot of money on the table for a small company or product division. One potential option is to fund all of the development and trials using SBIR grants and well as donations from eye research foundations to get past clinical trials and then either exit or run the company as a cash generator thereafter.

Product and Operations Section

What the product is

The product is an injectable hydrogel. A hydrogel is a polymer gel that contains water. A common example is a contact lens, which is a stiff gel and contains around 60% water. Hydrogels are made from polymers that can absorb water and also form a network of chains. It is analogous to a three-dimensional tennis net, which is made up of strings tied together with knots. Polymers are chains of molecules, so in the tennis net analogy they would be the strings and the chemical bonds that form the polymer gel would be the knots. In a hydrogel, the knots are only nanometers apart.

The hydrogel is 'injectable' because it can be squeezed through a very small diameter surgical needle as a liquid and only forms a gel in situ once injected (which happens when the chemical bonds form). Most gels cannot be formed in this way. One example of a gel that forms in situ is super glue, but super glue cannot absorb water.

Our hydrogel is designed to be injected during surgery into the part of the eye called the vitreous body. The vitreous body is the space between the lens and the retina. The vitreous body is normally filled with a natural hydrogel called the vitreous humor. The vitreous humor is often removed during retinal surgery, in a procedure called a vitrectomy. Currently, there is no adequate replacement for the vitreous humor; retinal surgeons inject gases or silicone oil into the eye after vitrectomy.

What is unique about it

The product is unique in many ways:

- It gels spontaneously in aqueous solution a few minutes after injection through a small diameter surgical needle
    - unlike gases or silicone oil which remain viscous

  - unlike many hydrogels which must be gelled outside the body and therefore not injectable through surgical needle
  - unlike other injectable hydrogels that require UV light, basic conditions or additional chemicals to form gels
  - unlike other hydrogels that have to be formed in absence of water and subsequently hydrated
- It has mechanical properties similar to the natural vitreous
  - unlike gases or silicone oil
- It doesn't need to be removed in a second surgery
  - as silicone oil does
- It doesn't require the patient to lie face down for 2 weeks after surgery
  - as gases do
- It is transparent
  - unlike some hydrogels which are opaque
- It is biocompatible with the retina
  - unlike some other tested vitreous substitutes
  - it is made from a family of polymers that is already FDA approved
- It does not swell

How it works

The product works by preventing excess fluid from seeping behind the retina, which causes the retina to detach from the back of the eye (i.e. from the choroid). The retina relies on the choroid for nutritional support and prolonged detachment will result in death of photoreceptors (responsible for vision). This is why retinal detachment is a medical emergency.

Intellectual property strategy

We plan on generating IP within the company as we iterate on our initial designs for the product. Therefore we expect the company to own much of its IP in the form of trade secrets and key patents. In addition, the company expects to license the technology

Associated technical risks

There are significant technical risks associated with development of a medical device. These can be classed according to safety and efficacy.

Safety risks include problems associated with biocompatibility, toxicity and sterility of the product. Further safety risks include mechanical damage attributed to deployment and placement of the technology in the human body. Other risks include anticipated side effects, such as abnormal intraocular pressure, glaucoma, failure to promote reattachment of the retina, cause of re-detachment of the retina, cataract formation, and ischemia, hypoxia or hemorrhage of the retina resulting from application of the technology. We hope to provide a better safety profile than currently available technologies, particularly with respect to cataract formation, intraocular pressure and glaucoma.

Efficacy risks are associated with how successfully the technology keeps fluid away from a retinal tear. The technology may not perform as desired and may be sensitive to surgical technique. Even if we show much improved efficacy, existing technologies may be more robust/predictable and better understood by clinicians, so that adoption/adjustment to new a risk/benefit profile may be a challenge.

We believe that the preclinical models and outcome measures will enable us to determine safety and efficacy potential to a large degree prior to commencing clinical trials, and will provide a ‘proceed or surrender’ signal. This will have a significant impact on the flexibility of financing the company, and the reduction of costs through the optionality and segregation of funding cycles.

Competitive Advantage

Competing companies

“The Big Guys”

Bausch & Lomb manufacture Oxane HD ™

- Founded 1853, headquartered in Rochester, New York
- 13,000 employees in 36 countries
- 2007 revenue $2.51 Billion USD
- Divisions include contact lenses and medical devices for ophthalmic surgery
- Owned by private equity house Warburg Pincus since 2005
- Last SEC 10K filing when the company was public (FY2005) gives net sales in the different divisions including “cataract & vitreoretinal”:

Table 3. Bausch and Lomb net sales in 2005 in USD millions. Source: SEC Edgar Filings.

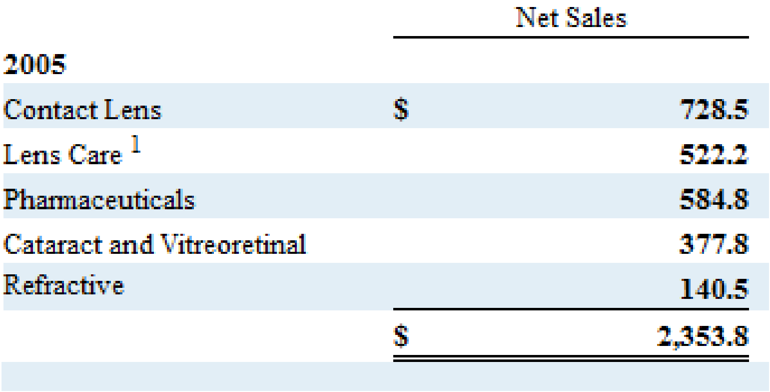

		Net Sales
2005		
Contact Lens	**$**	**728.5**
Lens Care [1]		**522.2**
Pharmaceuticals		**584.8**
Cataract and Vitreoretinal		**377.8**
Refractive		**140.5**
	$	**2,353.8**

“The Small Fish”

Fluoron GmbH manufactures Densiron 68™

- Subsidiary of Geuder AG
- Founded in 1996 by Prof Meinert
- Small, focused biotech company making innovative silicone oil tamponades (to remain in the eye for longer & longer periods) as well as new materials like perfluorocarbohydrates and semifluorinated alkanes for intraoperative use

“The Italian Job”

Alchimia make a range of silicone oils and intraocular gas tamponades

- Based in Padova, Italy
- Founded by a team of research chemists in 1993
- Publish 5-10 papers per year in peer-reviewed journals, mostly presented at conferences
- Active in R&D: focus is on heavier-than-water silicone oils

Competing technologies

Silicone oil

Companies making silicone oil include Alcon Laboratories and Bausch + Lomb Surgical. Following is a brief profile of each of these major competitors.

Alcon Laboratories

Product: SILIKON® 1000 (purified polydimethylsiloxane) Surgical Oil

Product advantages: Reasonably high effectiveness outcomes, 84% effectiveness for preserved vision and 70% for complete after six months (source: Alcon)

Product disadvantages: High incidence of cataracts (63%), hypotony (19%) and corneal opacity/abrasion (26%) measured six months post-surgery (source: Alcon)

Price: $100 per 10mL vial (source: The Aesthetic Guide Primary Care Edition Autumn 2009)

Company: Alcon Retina is a research division of Alcon, founded in 1945, a global medical company specializing in eye care products and now a subsidiary of Novartis. In 2010, Alcon had sales of USD$7.2B and net income of USD$2.2B, offering a range of pharmaceutical, surgical and consumer eye care products.

Bausch + Lomb

Product: ADATO® SIL-OIL 5000 Silicone Oil

Usage: As a prolonged retinal tamponade in selected cases of complicated retinal detachments

Product advantages: Sold as pre-filled silicone oil disposable syringes (rather than vials) for ease-of-use in terms of sterility and administering

Product disadvantages: Use as a long-term tamponade has not been studied. Like other silicone oils, it carries high risk of cataracts, anterior chamber oil migration, keratopathy, and glaucoma.

Pricing: AU$1,140 for a packet of six (source: Bausch Australia)

Company: Bausch + Lomb is a private company founded in 1853 in the U.S. and is one of the world's leading suppliers of eye health products. Its three categories of products are Vision Care, Pharmaceuticals, and Cataract and Vitreoretinal Surgery. The company had USD $2.4B in sales and net income of USD$52M in 2007.

Surgical Gas

Following is an example of a company supplying ophthalmic gases to surgeons.

Air Products

Products: A range of medical device gases for ophthalmic surgery including hexafluorohethane, octafluoropropane, and sulphur hexafluoride

Usage: The gas is injected into the vitreous of the eye and expands over several days, sealing the retinal tear and the area surrounding the tear as the pressure of the gas bubble pushes against it.

Product disadvantages: The treatment is very inconvenient to the patient, who must lie face down for two weeks to maintain the position of the gas bubble against the retinal tear. Deviating from this requirement may re-introduce complications or prevent proper recovery of the treatment.

Company: Air Products is a global supplier of gases, performance materials, equipment and services. It comprises three main divisions: (1) Merchant Gases, (2) Tonnage Gases, Equipment and Energy, (3) Electronics and Performance Materials. Gases for healthcare and medical (including ophthalmic gases) is a part of the Merchant Gases division. This division alone had sales of USD$3.7B in 2010.

Feature comparison matrix

Table 4. Comparison of competitors' effectiveness and features. Source: Alcon Technologies

Feature	**Silicone Oil**	**Gases**	**New Technology**	**Inferior/Superior**
Effectiveness in sealing retinal tear	84% effectiveness for preserved vision and 70% for complete after six months	Effective in sealing a retinal tear as the gas bubble keeps water away from it	We anticipate equal ability to seal retinal tears, but more versatility to seal tears in any part of the eye without special head positions	Equal
Time period in the eye	Must be removed a	Two weeks	Years – the material is biocompatible	Superior
Complications	High incidence of cataracts (63%), hypotony (19%) and corneal opacity/abrasion (26%) measured six months post-surgery (source: Alcon)		We anticipate better oxygen transport and pressure regulation which would reduce cataracts	Superior
Convenience for surgeon	Comes in prefilled syringes		Can be packaged in prefilled syringes but requires more careful handling	Equal/Inferior
Convenience for patient	Requires a second surgery to remove silicone oil	Requires patient to lie face down for two weeks. Deviation may re-introduce complications	No second surgery or special positioning required	Superior

Other Competitors

- For example, Covidien, Boston Scientific
- Other biomaterials companies
- Eye laser companies for retinal surgeries
- Researchers inventing and testing new biomaterials
- Organizations that help to prevent retinal problems e.g. nutritional products, smoking cessation

Marketing Strategy

Our marketing philosophy is that our product offers a better quality of life to patients of vitrectomy surgeries and reduces the risk of complications, which benefits not only the sufferer but also the ophthalmic surgeon, the hospital, and the medical insurance company.

Our approach is a marketing strategy that will facilitate a public awareness of the benefits of our medical device, which is far superior to existing forms of technology for vitrectomy surgeries.

The marketing communication will convey:

- Improved efficacy
- Reduced risk of complications
- Reduced risk of repeat surgeries
- Lower total cost of treatment (analogous to TCO)
- Better quality of life

As this is a medical device currently still subject to clinical trials, we need to take some unique approaches to our marketing strategy. This can be viewed in two sequential stages, each requiring a different approach to marketing and distribution.

Stage 1: Clinical trials

In this stage we will not establish any channels of distribution given the product cannot yet be sold the general market. By far, the key players in the value chain are our chief ophthalmic surgeons participating in the clinical trials. Marketing is achieved in the following manner:

- Establishing credibility for the device as it progresses through clinical trials
- Creating awareness of the new technology through publications and medical conferences, where the chief surgeon will be the advocate for the product. Her reputation in the medical community is therefore essential.

During this stage, our strategy is to target only the professional community of ophthalmic surgeons.

Stage 2: After completion of trials and FDA approval

Once the product is ready for launch, we expect to employ a direct sales team for customer acquisition and distribution. The reasons for this approach are:

- It is a concentrated market in terms of potential sales volume per surgeon
- As a medical device, the product requires highly trained professionals to market
- Establishing relationships with the medical surgeon

The geographic areas we will initially target are the United States and Europe, where we have potentially lower clinical hurdles. In the U.S. we will initially target the Boston area, represented by one of the leading hospitals in the country, Massachusetts Eye and Ear Hospital. Expansion to the rest of the country will take place once the device achieves regulatory approval. Such a rapid expansion target makes sense because our customers are concentrated to a small population around the country, which lends itself to sales by our direct sales force being achieved rapidly. Since retinal detachment is a medical emergency, there is no seasonality to our business and we do not need to consider any off-season sales.

Sales and distribution

As earlier discussed, our method of sales and distribution will initially be through publicizing by word-of-mouth in the medical community, journal publications, and medical conferences. A large part of this will be driven by our chief ophthalmic surgeon who will be a proponent of this technology; simultaneously boosting his own professional reputation is a pioneer in this area of ophthalmic surgery.

The longer range method of sales is to deploy a direct sales force of highly trained professionals. Core to sales professional's responsibilities are:

- Fostering a long-term client relationship with the ophthalmic surgeon
- Maintaining order flow and delivery of Hydrogel to clients
- Provide training on product usage and assistance during vitrectomy surgeries
- Being the first point of call for support or issues raised about the product
- Building new client relationships and seek opportunities to grow orders and revenues

As this is a synthetic pre-sterilized product that will be packaged into very small units, distribution by the direct sales force is achievable considering the concentrated number of potential customers.

Our sales force expansion plan is to extend our sales team into major metropolitan cities in the United States as a follow-the-customer strategy, as this is where the major medical hospitals and ophthalmic surgeons tend to be located. Table 2 shows our expected sales schedule for each sales person.

Table 5. Sales schedule of expected cost per Sales Professional

Retainer	$60,000
Average number of clients	20
Annual surgeries per client	150
Price per unit	$5,000
Revenue per sales person	$15,000,000
Commission rate	2%
Total commission	$300,000
General expenses (travel, etc.)	$50,000
Cost per Sales Professional	**$410,000**

Advertising and Promotion

We expect that once we are able to achieve a minimum penetration rate for our product (say 20%), we can begin directly marketing to potential patients in the general public to raise our brand awareness, similar to the marketing strategy employed by LASIK for laser eye surgery. This will be supplementary to our direct sales force and not a substitute for them.

The objective of direct advertising is to try and create some customer pull, so that patients will ask their doctors and surgeons for Hydrogel treatment. Although the surgeon's own recommendations will still have by far the greatest influence on the patient's decision, creating public brand awareness will be helpful to:

- Persuade ophthalmic surgeons who do not use Hydrogel to consider using it, reducing the acquisition cost for our direct sales team
- Create brand value to raise barriers to entry for potential competing products in future

Operations

The company needs $4 million to complete the preclinical phase, which represents a major milestone and decision point; a potential 'double-down' for investors as well as an opportunity for a strategic acquisition.

Phases of development and resources needed ($1000s)

Table 6. Expected resources needed for pre-clinical and clinical trials.

Phase	Pre-clinical				Clinical					Market
Year	1	2	3	4	5	6	7	8	9	10
SG&A	100	200	200	200	900	1,000	1,100	1,200	1,300	2,600
Pre-clinical studies	60	250	300	300						
R&D	200	500	500	500						
CAPEX	320									50
Clinical trial through FDA approval					1,000	1,000	2,000	2,500	3,000	

Selling, general & administrative (SG&A)

Initially, SG&A will consist mainly of costs associated with running the business, including costs of fundraising, legal costs of incorporation, patent filing and licensing, and hiring employees, advisors and consultants. During the clinical and market phase, there will be selling expenses as the company generates knowledge about its products, mainly through professional organizations and scientific presentations, as well as increased G&A associated with operating a company in sales mode. Upon product launch, there will be also expenses incurred for the manufacturing, packaging and distribution of the hydrogel. These costs will become better defined as we refine our strategies on production (e.g. whether to outsource manufacturing) and distribution (e.g. channel partners and supply chain).

Pre-clinical studies

Pre-clinical studies will be conducted in collaboration with vitreoretinal surgeons who maintain world-class preclinical research facilities. The preclinical studies mirror the eye physiology, surgical procedures and outcome measures performed in the clinic. The hospital already has the staff, equipment and resources to conduct these studies, and is largely supported by grants. We anticipate being able to conduct a significant amount of preclinical research using grants.

Research & Development (R&D)

During the pre-clinical phase, we will iterate on the materials used to make the hydrogel, to improve it and generate new IP in design as well as manufacturing and surgical methods. R&D costs will include the costs of a chemical engineer, a polymer scientist and a lab technicians, as well as chemical supplies.

We will also face costs associated with filing for FDA approval, and will need to hire a Quality and Regulatory Affairs specialist as we move towards clinical studies.

Capital Expenditures (CAPEX)

The company will open a small laboratory for R&D and incur capital expenditures associates with purchase of polymer synthesis equipment and chemical and physical analytical equipment for a wet chemical lab. We anticipate further capital expenditure in setting up corporate infrastructure including office space upon completion of clinical trials and commencement of marketing. Further capital expenditure will be required if we choose to manufacture the product in-house. Given the high fixed costs of running a production facility, we may choose to delay this approach until we have reached sufficient scale in production volume.

Clinical studies

We expect to conduct clinical studies at a major research hospital, such as Massachusetts Eye and Ear Institute, under direction of a Clinical Research Organization.

Finance Section

Financial Summary

Hydrogel's proprietary technology – a gel for the replacement of intraocular jelly following intrusive ophthalmic surgery – is still under development and requires two rigorous testing phases before general release into the surgical devices market: i.e. both pre-clinical and clinical trials. These phases are expected to last approximately 4 and 5 years respectively, at a total cost of around $4-5 million for preclinical and upwards of $10 million for clinical trials.

Therefore we present here an extended, yearly income statement for the period 2012-2025, comprising three different phases corresponding to the preclinical, clinical and mass market stages of the company's growth. We focus primarily on the company's financials through the foreseeable future in a 4-year timeframe, during which the technology will be pushed through the pre-clinical phase. By partnering with a third-party, experienced medical professional with full access to resources and independent funding grants, we expect to generate revenue through the sale of our gel as a high-margin developmental (academic) product. Following this strategy, we expect to reach breakeven in net income sometime in the first quarter of 2015. Similarly, the gel will be sold as a medical research product during the clinical phase, and we expect the company to break even in net income during the first year of clinical trials.

Meanwhile we will pursue a fundraising strategy focused on seed funding through government and other medical grants coupled with a bridge loan from a private investor. Following that, the company will seek to raise $1M in a funding round in year 3 and a further $3M in year 5. This will help build the company's commercial, manufacturing and research capabilities in Cambridge, MA and address costs associated with FDA approved (pre-) clinical trials in the US.

Marketing and sales costs will be low during the first three years, during which there are no projected sales to the general surgical devices market.

Extended Projected Income Statement for Hydrogel

In the preclinical stage, we are looking to partner with a specific research leader to leverage the existing hospital and laboratory resources efficiently. The company will initially generate revenue through the sale of developmental 100 ml sachets of its product, at a price of $500 each. This price is a 90% discounted rate of our $5000 product selling cost based on our previous calculations of expected lifetime surgery cost reductions: using current technologies, the cost to the patient (insurer) is on average > $12,000 for this type of ophthalmic surgery. By using our product we expect this figure to drop below $6,000.

Main Assumptions

- COGS is initially higher during the developmental stages when the product will go through many iterations and modifications based on researcher feedback; it then drops to 0.1% of selling price, reflecting the extremely low manufacturing cost of our product.
- Our hiring strategy is to start with the founders managing the overall project and leading two full-time R&D professionals to build the manufacturing base and supply the pre-clinical medical research requirements. We do not hire management staff until mid-way through the clinical period as we ramp up production and begin a more dedicated sales and marketing strategy. Finally, we hire 2 sales staff in the final stages of clinical trials to build a customer base for product launch in 2020.
- We purchase $300,000 worth of equipment and wet laboratory space for the pre-clinical trial period, which depreciates at a fixed rate of 10% p.a. thereafter. For the clinical period we anticipate capital costs of $0.5M for technical equipment, and subsequently $1M to ramp up production for market launch.
- We assume a tax rate of 35% and tax deferred assets are not used.

Long-term free cash flow projections for Hydrogel (in $ ‘000’s)

Table 7. Projected income statement for Hydrogel 2012-2025 in ‘000s of USD.

Phase	**Pre-clinical Trials**				**Clinical Trials**					**Market**				
Year (End)	**2012**	**2013**	**2014**	**2015**	**2016**	**2017**	**2018**	**2019**	**2020**	**2021**	**2022**	**2023**	**2024**	**2025**
Price / trial product	0.5	0.5	0.5	0.5	1	1	1	1	1	-	-	-	-	-
Trial sales	100	200	400	1000	2000	2000	3000	5000	5000	-	-	-	-	-
Price / surgery	-	-	-	-	-	-	-	-	-	5.0	5.0	5.0	5.0	5.0
Market Share	0.0%	0.0%	0.0%	0.0%	0.0%	0.0%	0.0%	0.0%	0.0%	5.0%	10.0%	20.0%	35.0%	50.0%
Sales Revenue	$ 50	$ 100	$ 200	$ 500	$ 2,000	$ 2,000	$ 3,000	$ 5,000	$ 5,000	$ 37,500	$ 75,000	$ 150,000	$ 262,500	$ 375,000
COGS	0.5	1.0	1.0	2.5	10.0	10.0	10.0	10.0	10.0	0.4	0.8	1.5	2.6	3.8
Gross Profit	$ 50	$ 99	$ 199	$ 498	$ 1,990	$ 1,990	$ 2,990	$ 4,990	$ 4,990	$ 37,500	$ 75,000	$ 150,000	$ 262,500	$ 375,000
Gross Margin %	99.0%	99.0%	99.5%	99.5%	99.5%	99.5%	99.7%	99.8%	99.8%	> 99.9%	> 99.9%	> 99.9%	> 99.9%	> 99.9%
OPEX														
Founder Salaries	$ 20	$ 30	$ 60	$ 75	$ 250	$ 250	$ 250	$ 250	$ 250	$ 400	$ 500	$ 600	$ 750	$ 750
R&D Staff	$ 2	$ 2	$ 4	$ 4	$ 5	$ 6	$ 8	$ 8	$ 8	$ 3	$ 3	$ 3	$ 3	$ 3
R&D Staff Salaries	$ 200	$ 200	$ 400	$ 400	$ 500	$ 600	$ 800	$ 800	$ 800	$ 300	$ 300	$ 300	$ 300	$ 300
Management Staff	$ -	$ -	$ -	$ -	$ -	$ -	$ 1	$ 2	$ 2	$ 4	$ 4	$ 4	$ 4	$ 4
Management Staff Salaries	$ -	$ -	$ -	$ -	$ -	$ -	$ 150	$ 300	$ 300	$ 600	$ 600	$ 600	$ 600	$ 600
Sales Staff	$ -	$ -	$ -	$ -	$ -	$ -	$ -	$ -	$ 1	$ 5	$ 10	$ 20	$ 30	$ 50
Sales Staff Salaries	$ -	$ -	$ -	$ -	$ -	$ -	$ -	$ -	$ 360	$ 1,800	$ 3,600	$ 7,200	$ 10,800	$ 18,000
Marketing and Travel	$ -	$ -	$ -	$ 10	$ 10	$ 20	$ 20	$ 50	$ 50	$ 250	$ 500	$ 1,000	$ 1,500	$ 2,500
G&A (non-salary)	$ 33	$ 35	$ 69	$ 71	$ 113	$ 128	$ 180	$ 203	$ 257	$ 465	$ 750	$ 1,305	$ 1,868	$ 2,948
Preclinical Trial Related Expenses	$ 200	$ 200	$ 200	$ 200										
Clinical Trial (FDA) Related Expenses					$ 100	$ 100	$ 100	$ 100	$ 100					
TOTAL OPEX	$ 455	$ 467	$ 733	$ 760	$ 978	$ 1,104	$ 1,509	$ 1,713	$ 2,128	$ 3,827	$ 6,267	$ 11,032	$ 15,855	$ 25,155
CAPEX														
Technical Equipment	$ 200	$ 180	$ 160	$ 140	$ 620	$ 558	$ 496	$ 434	$ 372	$ 310	$ 248	$ 186	$ 124	$ 62
Laboratory Rent	$ 100	$ 100	$ 100	$ 100	$ 200	$ 200	$ 200	$ 200	$ 200	-	-	-	-	-
Non-technical Equipment	$ 20	$ 18	$ 16	$ 14	$ 10	$ 10	$ 10	$ 10	$ 10	$ 50	$ 50	$ 50	$ 50	$ 50
TOTAL CAPEX	$ 320	$ 298	$ 276	$ 254	$ 830	$ 768	$ 706	$ 644	$ 582	$ 360	$ 298	$ 236	$ 174	$ 112
Earnings before Interest and Taxes (EBIT)	$ (726)	$ (666)	$ (810)	$ (517)	$ 183	$ 119	$ 775	$ 2,634	$ 2,281	$ 33,313	$ 68,435	$ 138,732	$ 246,471	$ 349,733
Pretax Income	$ (726)	$ (666)	$ (810)	$ (517)	$ 183	$ 119	$ 775	$ 2,634	$ 2,281	$ 33,313	$ 68,435	$ 138,732	$ 246,471	$ 349,733
Taxes	-	-	-	-	$ 64	$ 41	$ 271	$ 922	$ 798	$ 11,660	$ 23,952	$ 48,556	$ 86,265	$ 122,407
Free Cash Flow	$ (726)	$ (666)	$ (810)	$ (517)	$ 119	$ 77	$ 504	$ 1,712	$ 1,482	$ 21,653	$ 44,483	$ 90,176	$ 160,206	$ 227,327

Breakeven analysis:

Based on these projections, the company is expected to become cash flow positive around the first quarter of 2016, or 58 months from incorporation at the beginning of 2012. If the company succeeds in clinical trials, it will be able to self-fund the investment required to go to market.

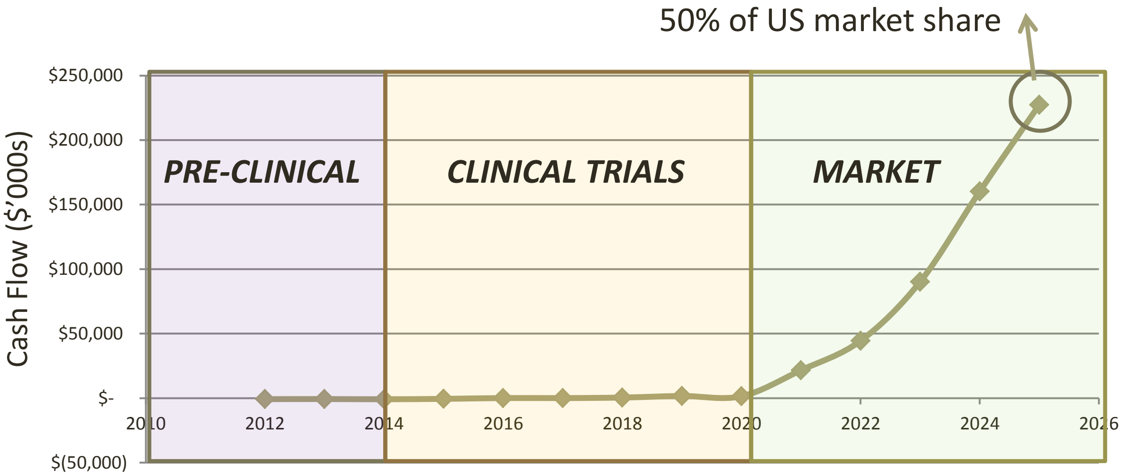

Figure 4. Projected cash flow through 2025 in '000s of USD.

Capitalization and Ownership

To fund the pre-clinical trial period with the anticipated $4-5 million required, we will pursue three complimentary strategies:

I. Application for SBIR (Small Business Innovation Research) grants from the National Institute of Health (NIH). This government-sponsored grant is non-diluting and does not require repayment. A typical application cycle lasts 4-5 weeks and if successful results in two funding phases of $100,000 (6 month period) and $750,000 (over 2 years).

II. Early capital raise from private investors (starting beginning 2012) to make up to $1 million, along with grants, for year 1. This would preferably be a convertible bridge loan with a due date in mid-2013 and an optional discount of 20% on series A funding, but we can also offer preferred stock in the company.

III. Two successive funding rounds of $1 million in 2013 and $3 million in 2015 from institutional investors.

Ownership structure

The three founding members will retain a 5% stake in the company each after the pre-clinical funding rounds. We also retain 10% as stock options for future employees to attract and retain talented management, R&D and sales staff. A breakdown of the equity share at each round of capital raising is below:

Table 8. Equity split for stakeholders following successive funding rounds.

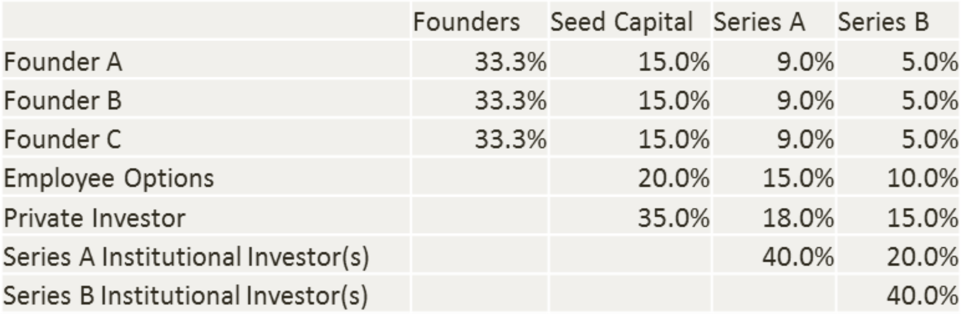

	Founders	Seed Capital	Series A	Series B
Founder A	33.3%	15.0%	9.0%	5.0%
Founder B	33.3%	15.0%	9.0%	5.0%
Founder C	33.3%	15.0%	9.0%	5.0%
Employee Options		20.0%	15.0%	10.0%
Private Investor		35.0%	18.0%	15.0%
Series A Institutional Investor(s)			40.0%	20.0%
Series B Institutional Investor(s)				40.0%

Figure 5: Pie charts of equity split following three major investment rounds.

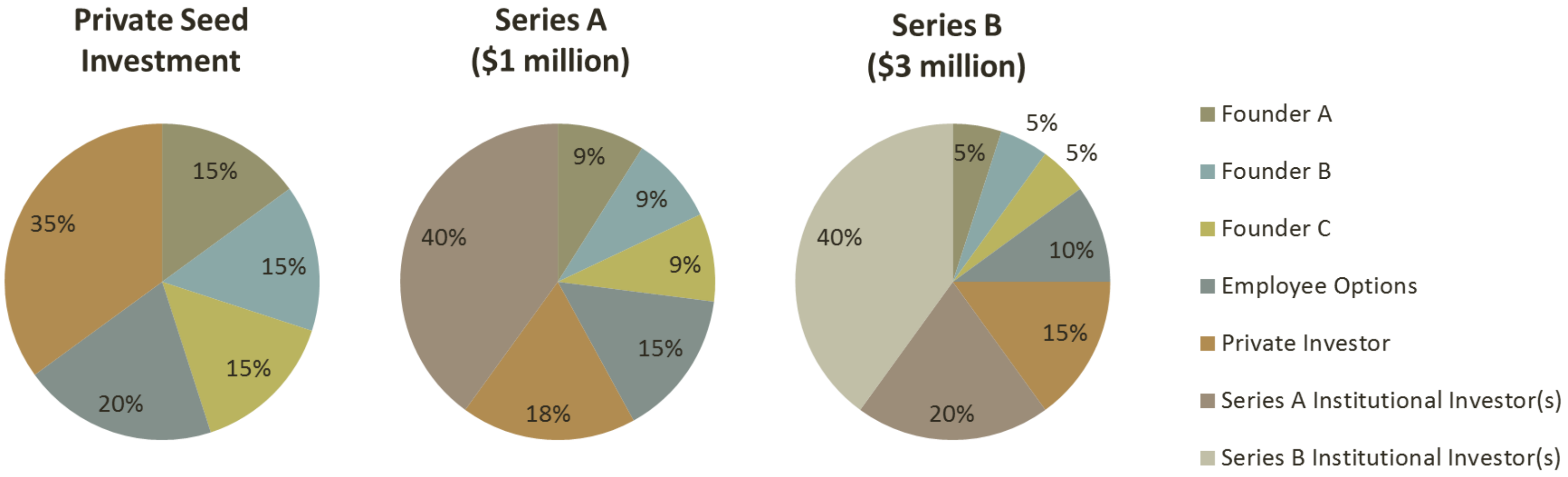

Balance Sheet (in $ '000's)

Hydrogel's projected balance sheet for the pre-clinical period, through the end of 2015, is displayed below, reflecting the three rounds of capital injection.

Table 9. Projected balance sheet for Hydrogel for the pre-clinical trial period in '000 of USD.

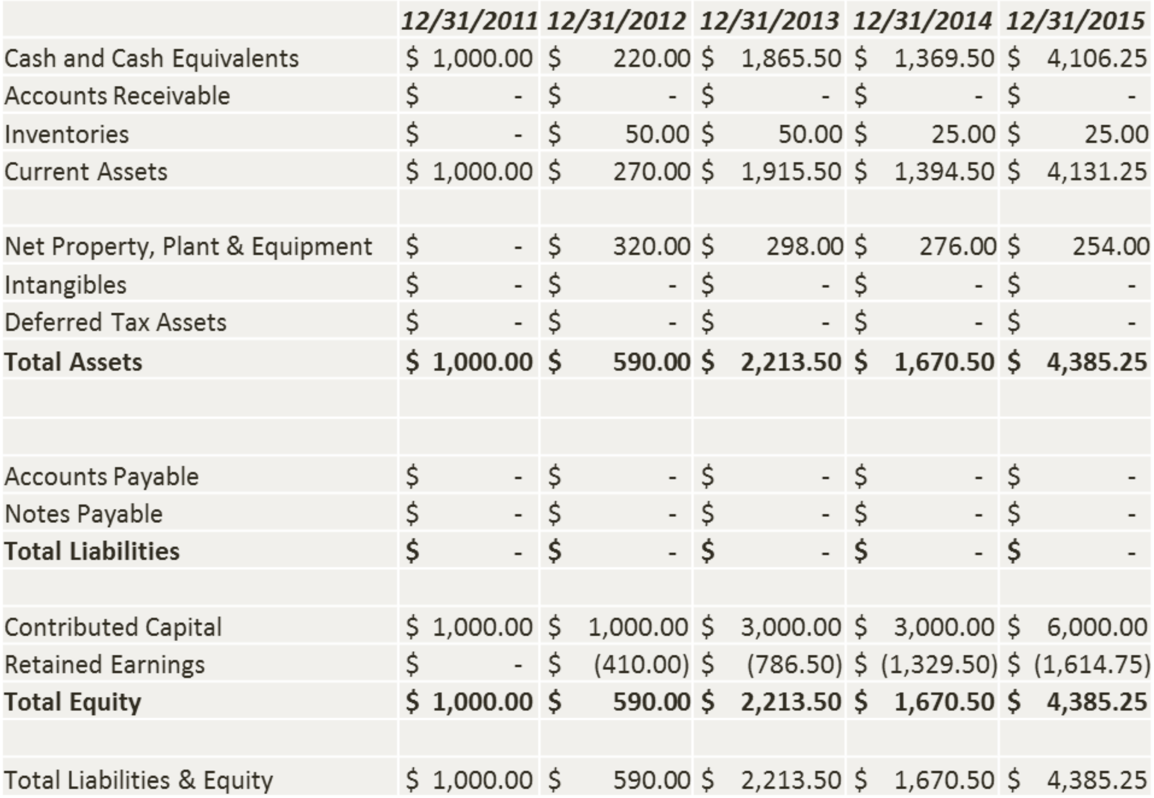

	12/31/2011	***12/31/2012***	***12/31/2013***	***12/31/2014***	***12/31/2015***
Cash and Cash Equivalents	$ 1,000.00	$ 220.00	$ 1,865.50	$ 1,369.50	$ 4,106.25
Accounts Receivable	$ -	$ -	$ -	$ -	$ -
Inventories	$ -	$ 50.00	$ 50.00	$ 25.00	$ 25.00
Current Assets	$ 1,000.00	$ 270.00	$ 1,915.50	$ 1,394.50	$ 4,131.25
Net Property, Plant & Equipment	$ -	$ 320.00	$ 298.00	$ 276.00	$ 254.00
Intangibles	$ -	$ -	$ -	$ -	$ -
Deferred Tax Assets	$ -	$ -	$ -	$ -	$ -
Total Assets	**$ 1,000.00**	**$ 590.00**	**$ 2,213.50**	**$ 1,670.50**	**$ 4,385.25**
Accounts Payable	$ -	$ -	$ -	$ -	$ -
Notes Payable	$ -	$ -	$ -	$ -	$ -
Total Liabilities	**$ -**	**$ -**	**$ -**	**$ -**	**$ -**
Contributed Capital	$ 1,000.00	$ 1,000.00	$ 3,000.00	$ 3,000.00	$ 6,000.00
Retained Earnings	$ -	$ (410.00)	$ (786.50)	$ (1,329.50)	$ (1,614.75)
Total Equity	**$ 1,000.00**	**$ 590.00**	**$ 2,213.50**	**$ 1,670.50**	**$ 4,385.25**
Total Liabilities & Equity	$ 1,000.00	$ 590.00	$ 2,213.50	$ 1,670.50	$ 4,385.25

Discounted Cash Flow Analysis of Hydrogel (in '000's)

Based on these assumptions and projections, we expect Hydrogel to have a net present value of over $806 million. This valuation reflects our estimate that Hydrogel will achieve a 50% market penetration five years after clearing FDA approval and going to the general surgical market. After this initial period, the company can expect to sell the gel at extremely high margin (>99%) in a specialised and market sector with little to no competition, yielding multi-tens of million dollar rapidly after incorporation.

Table 10. DCF analysis of Hydrogel in '000s of USD.

Phase	**Pre-clinical Trials**				**Clinical Trials**					**Market**				
Year (End)	**2012**	**2013**	**2014**	**2015**	**2016**	**2017**	**2018**	**2019**	**2020**	**2021**	**2022**	**2023**	**2024**	**2025**
Free Cash Flow	$ (726)	$ (666)	$ (810)	$ (517)	$ 119	$ 77	$ 504	$ 1,712	$ 1,482	$ 21,653	$ 44,483	$ 90,176	$ 160,206	$ 227,327
Present value of free cash flow	$ 10,787													
Plus: Present value of terminal value	$ 795,644													
Less: Debt	$ -													
Equity Value	**$ 806,431**													
Key Assumptions														
Tax Rate	40%													
Discount Rate	35%													
Long-term growth rate	5%													

Notes and References

1. “Posterior Segment Eye Procedures, Level III”
2. J.J-H. Huang et al., Cost analysis in vitrectomy: monitored anesthesia care and general anesthesia, AAA Journal 69 (2) 2001. (general anesthesia case)
3. J.J-H. Huang et al., AAA Journal 2001. (monitored local anesthesia case)
4. S. Wolf et al., Silicone oil–rmn3 mixture (“heavy silicone oil”) as internal tamponade for complicated retinal detachment, Retina 23 (3) 2003.
5. H. Mintz-Hittner et al., Efficacy of Intravitreal Bevacizumab for Stage 3+ Retinopathy of Prematurity, New Eng. J. Medicine 364 (7) 2011.